

Low Energy Electron Diffraction Studies of Transition Metal Oxide Surfaces and Films

Dissertation

zur Erlangung des akademischen Grades
doktor rerum naturalium (Dr. rer. nat.)

vorgelegt der

Mathematisch-Naturwissenschaftlich-Technischen Fakultät
(mathematisch-naturwissenschaftlicher Bereich)
der Martin-Luther-Universität Halle-Wittenberg

von Jian Wang

Master of Science

geb. am: 09.05.1973 in: Lanxi, P. R. China

Gutachterin bzw. Gutachter:

1. PD. Dr. Karl-Michael Schindler
2. PD. Dr. Angelika Chassé
3. Prof. Dr. Herbert Over

Halle (Saale), 07.02.2005

urn:nbn:de:gbv:3-000007962

[<http://nbn-resolving.de/urn/resolver.pl?urn=nbn%3Ade%3Agbv%3A3-000007962>]

Contents

1. Introduction	1
2. Metal Oxides Surfaces	7
2.1 Cobalt Oxides	7
2.2 Barium Titanate	8
2.3 Properties of Oxide Surfaces	9
2.4 Cobalt Oxide Surfaces	14
2.5 Barium Titanate Surfaces	17
3. Theory of Low Energy Electron Diffraction	23
3.1 Kinematic LEED Theory	23
3.2 Dynamic LEED Theory	28
4. Experimental	37
4.1 Experimental Equipment	37
4.1.1 UHV System A	37
4.1.2 SPA-LEED System	38
4.1.3 UHV System B	40
4.1.4 LEED $I - V$ Measurement System	41
4.2 Sample Preparation	44
4.2.1 Ag(100) Substrate	44
4.2.2 CoO Films	45
4.2.3 BaTiO ₃ (111) Surface	46
5. SPA-LEED Analysis of CoO on Ag(100)	47
5.1 Characterization of the Ag(100) Surface	47
5.1.1 Instrument Response Function	47
5.1.2 Defects on the Ag(100) Surface	49
5.1.3 Ion Sputtered Ag(100) Surface	51
5.2 CoO Films on a Ag(100) Surface	55
5.2.1 Growth at 300K	56
5.2.2 Growth at 390K	63
5.2.3 Growth at 470K	64

6. Tensor-LEED Analysis of Oxide Surfaces	67
6.1 The Ag(100) Surface	67
6.1.1 Introduction	67
6.1.2 TLEED Calculations	68
6.1.3 Results and Discussions	70
6.2 CoO/Ag(100) Surface	72
6.2.1 Introduction	72
6.2.2 TLEED Calculations	74
6.2.3 Results and Discussions	74
6.3 BaTiO ₃ (111) ($\sqrt{3} \times \sqrt{3}$)R30° Surface	78
6.3.1 Introduction	78
6.3.2 Surface Structure of BaTiO ₃ (111)	79
6.3.3 TLEED Calculations	81
6.3.4 Results and Discussions	83
7. Conclusions	89
Bibliography	93
Abbreviation	103
Erklärung	105
Acknowledgements	107
Curriculum Vitae	109

Chapter 1

Introduction

Metal oxides, especially transition metal oxides comprise a very diverse and fascinating class of compounds with properties covering almost all aspects of material science and physics [1]. The bonding characteristics may be classified as covalent for one system and highly ionic for the other. For the electrical conductivity, they cover the entire range from metals to semiconductors and insulators. For example, they can be insulators (CoO, NiO, BaTiO₃), semiconductors (Fe_{0.9}O), metals (CrO₂, ReO₃) and superconductors (YBa₂Cu₃O₇) [2]. They can be ferromagnetic (CrO₂), anti-ferromagnetic (CoO, NiO), ferrimagnetic (Fe₃O₄, Y₃Fe₅O₁₂) and ferroelectric (BaTiO₃). Many oxides have different oxidation states, e.g. vanadium oxide (VO, VO₂, V₂O₃ and V₂O₅). For the crystal structure, they can be simple binary monoxides (NiO, CoO) with NaCl structure or ternary oxides (BaTiO₃, SrTiO₃) with perovskite structure. They also can form complicated structures such as Co₃O₄ or Fe₃O₄ with the normal and/or inverse spinel structure [3].

Due to the diverse physical and chemical properties, transition metal oxides find applications in many fields of technical interest, from nonlinear optics to sensors and catalysis. In some cases the bulk properties are important, as for example very often in nonlinear optics. In other cases the surface properties play a major role, as in catalysis [4]. The bulk properties of simple binary oxides are pretty well understood. In contrast, rather little is known about the surfaces of oxides, even the most simple ones. The present knowledge has been comprehensively reviewed by Henrich and Cox in their book *The Surface Science of Metal Oxides* [1].

Applications of Transition Metal Oxides. One of the most important applications of transition metal oxides is heterogeneous catalysis. They are used for synthesizing many organic compounds via selective oxidation, dehydrogenation, isomerization and other chemical processes. Not much is known about atomic scale mechanisms of catalytic reactions on transition metal oxides, and our understanding of basic transition metal oxide surface chemistry greatly lags behind that of semiconductors and metals. This basic understanding, in particular the relationships between the catalytic function of transition oxide materials and their crystallographic structures and chemical compositions in the surface region, is needed for a targeted catalyst development. On pure metal catalysts the delocalized electrons can easily

be transferred resulting in redox chemistry reaction mechanisms. Transition metal oxides are ionic compounds exposing acidic and basic sites, which may control their surface chemical properties. At the same time, the redox chemistry loses in importance, because the electronic states are separated by the bandgap and become less accessible. Metallic and semiconducting oxides with small bandgaps allow a combination of redox and acid base chemistry, whereas highly ionic oxides with large bandgaps become pure acid base catalysts. In this context, a large amount of work has been performed over polycrystalline oxide catalyst samples, resulting, for example, in the important concept of surface coordinatively unsaturated sites. But since electronic surface structures and acid base properties of oxides may vary greatly with the surface orientation, the conclusions to be drawn from studies on polycrystalline samples are limited. Therefore, a direct elucidation of atomic structural elements involved in chemisorption processes and catalytic conversions requires samples exposing one defined surface orientation. This has led to an increasing number of surface science studies on single crystal metal oxide samples within the last decade, accompanied by theoretical work [1, 5].

While transition metal oxides proved to be important in heterogeneous catalysis for decades, their application in the field of magnetic electronic came to be a subject of research only recently. For example, barium titanate (BaTiO_3) is a typical representative of ferroelectric materials with the useful properties of high spontaneous electric polarization and permittivity. In non-volatile ferroelectric computer memories both of these properties, the high permittivity and the permanent electrical polarization, are utilized [6]. Owing to the permanent polarization the charge of the capacitor of the memory cell circuit is maintained, even if the power is switched off, which makes the memory a nonvolatile one. Furthermore, the high permittivity helps to reduce the size of the capacitor, which is a rather large circuit element on computer chips. Since the material will be deposited as thin films in these applications, there is an increasing interest in the growth of such films. They have been grown on (100) and (111) oriented substrates using a variety of growing techniques, e.g. r.f.-sputtering [7,8], pulsed laser deposition/ablation [9, 10], reactive evaporation [11, 12] and metallo-organic chemical vapor deposition [13, 14]. Most of these investigations concentrate on the 'bulk' properties of such films. To an increasing extent, the films however are characterized using surface sensitive methods, such as Low Energy Electron Diffraction (LEED). The scope of interest has mainly been grain size, faceting and surface roughness on the scale of micrometers and nanometers. Structure on an atomic scale is still lacking, though.

Another application of BaTiO_3 is the use of polycrystalline n-doped material in thermistors of thermal overload protection circuits, where the specific resistivity of BaTiO_3 increases with temperature by several orders of magnitude in the range from 110 to 140 °C. The increase of resistivity with temperature results in a positive temperature coefficient of resistivity (PTCR). The PTCR effect in BaTiO_3 is obviously

related to the phase transition of BaTiO_3 at the Curie point ($T_c \approx 120^\circ\text{C}$), where the ferroelectric tetragonal room temperature phase converts to the paraelectric cubic one [15]. The permittivity undergoes dramatic changes during this phase transition. It has been widely accepted that the PTCR effect can be interpreted by a grain boundary barrier layer model proposed by Heywang [16]. According to his model, the PTCR effect is caused by an increase in the potential height of double Schottky-type barrier layers formed at the grain boundaries associated with the ferroelectric-paraelectric phase transition at T_c . The existence of two dimensional surface acceptor states is indispensable to the formation of the barrier layers. He assumed that a rapid decrease of the dielectric constant of the material above T_c , according to the Curie-Weiss law, causes an increase in the potential barrier height, consequently, a PTCR anomaly results. The Heywang model was improved by Jonker to account for a low resistance below the Curie point by taking account of the compensation effect of surface acceptor states by the spontaneous polarization [17]. However, the origin of acceptor states has not been firmly identified yet. Supposedly, they are due to segregation of impurities or changes in stoichiometry at the grain boundaries. The low resistivity at lower temperatures is more controversial. The barriers at grain boundaries could either be lowered by the large permittivity or by special ferroelectric domain boundaries. A more recent detailed discussion of this topic can be found in Refs. [18, 19].

In spite of these important applications and the progress in structure characterization of the ferroelectric domains by secondary electron microscopy [20], atomic force microscopy [21] and optical microscopy [22], our knowledge on the structure of single crystalline BaTiO_3 surfaces is still rather incomplete. While a number of publications exist for the (100) surface of BaTiO_3 and the related material SrTiO_3 , only a few papers on the (111) surface of a perovskite oxide have come to our attention. Regarding the structure determination by LEED analysis, only one paper on the $\text{SrTiO}_3(100)$ surface has been published [23], no quantitative LEED $I - V$ (Intensity vs Voltage) analysis has been performed on any BaTiO_3 surface. Our work has originally started with the BaTiO_3 system, where we made attempts to image and to characterize grain boundaries of polycrystalline samples as they may be visualized in the surface plane. It soon became clear during the experiments that a characterization of low index single crystalline surfaces of BaTiO_3 was also necessary for our understanding of polycrystalline material.

Preparation of Thin Oxide Films. The question of oxide preparation is central to all surface science investigations, and herein lies, what is possibly the greatest difficulty of all [1]. Compared to elemental solids, the preparation of any stoichiometric compound surface, in particular oxides, is extremely difficult, especially if we consider the preparation of different crystallographic orientations of oxide surfaces [1, 24]. In the cases of binary monoxides with NaCl structure (e.g. CoO and NiO), the polar (111) surfaces are more reactive than the non-polar (100) surface [25, 26]. Non-polar and polar surfaces of ionic binary oxides exhibit fundamentally different behaviors

as far as cleavage, which is one of the desirable preparation methods. The reason for this was pointed out long time ago and is intimately connected with the surface potential [27]. For non-polar surfaces, such as the CoO(100) and NiO(100) surfaces, the surface potential is finite [28]. Therefore, CoO and NiO can easily be cleaved along the (100) direction. However, the surface potential per unit charge diverges for polar surfaces (e.g. the NiO(111) or CoO(111) surfaces) so that cleavage of a rocksalt structure in this direction is not possible. Thus, if we are interested in preparing surfaces of different surface orientation, cleavage is not the most favorable method of preparation for an ionic polar oxide surface.

There are alternative methods of preparation of stable non-polar surfaces. One is to cut a crystallographic plane mechanically or by spark erosion and then polish the surface [1]. This technique is similar to procedures known for the preparation of metal surfaces. Once the sample resides in the vacuum chamber, these surfaces are sputtered and consecutively annealed in oxygen in order to replace oxygen vacancies induced via sputtering. This method has been successfully applied to bulk samples. TiO₂ is an example, where this method has been frequently used with apparently satisfactory results. Again, the preparation of polar surfaces is difficult, because these surfaces have the tendency to facet during the preparation process.

Another, rather different method of preparation is, that oxide films of varying thickness may be grown on metallic substrates [29]. The geometry of the metallic substrate then determines the structure of the oxide film to a large extent. It is this technique that allows preparation of non-polar as well as polar surfaces. Of course, the structural quality of the film depends very strongly on the epitaxial relation between the lattice constants of the metallic substrate and the oxide film. In other words, we can to a certain extent control the defect structure and defect density of the layers grown by controlling the lattice mismatch. Three techniques have been mainly used for this purpose. The most simple one makes use of the fact that a metal single crystal may be oxidized and a more or less well ordered oxide film is formed. In the case of NiO and CoO, ordered thin oxide films can be grown by oxidation of Ni or Co single crystal surfaces. The growth of NiO(100) layers on Ni(100) has been described in ref. [30]. The LEED pattern of oxidized Ni(100) surfaces, however, mostly indicates the presence of a rather imperfect NiO(100) film on top of Ni(100), which might result from the large lattice mismatch of nearly 20% between Ni and NiO. Although the use of highly oriented Ni(100) as substrate leads to considerable improvement of the LEED pattern from the oxidized surface [25], the large lattice mismatch always remains a problem, with the possible consequence of defect structures in the oxide film. An different approach to prepare well ordered NiO(100) films was used by Marre and Neddermeyer, who evaporated Ni onto a Ag(100) surface in an O₂ atmosphere. LEED and UV photoelectron spectroscopy have shown that a well ordered and smooth NiO(100) can indeed be obtained in this way [31]. The reason for this more perfect growth of NiO(100) layers by using a Ag(100) substrate is the smaller lattice mismatch

(only 2%) between NiO and Ag. These results were confirmed by Scanning Tunnelling Microscopy (STM). It has been demonstrated that deposition of Ni onto Ag(100) in an O₂ atmosphere leads to much better NiO(100) films than oxidation of Ni(100), at least regarding surface orientation, which is accessible by standard Laue techniques [32]. The third technique is the oxidation of alloy surfaces. The advantage here is that the physical properties of the alloy may be advantageous for the preparation process. Using this technique, a well ordered Al₂O₃ film on NiAl(110) [33] and Ni₃Al(111) [34, 35] has been prepared. The Al₂O₃ film can be heated to above 1000 °C without melting the substrate. This is of crucial importance to order the layer. On Al metal such a heat treatment would lead to melting of the substrate before the oxide layer could order.

It is the purpose of the present work to provide some details on the growth of CoO(100) films on Ag(100) and to compare the results from NiO(100) films with those from CoO/Ag(100) prepared and measured in the same way. The lattice mismatch between CoO(100) and Ag(100) is slightly larger (4.3%) than that of NiO(100)/Ag(100) and it might be interesting to look for defect structures associated with the differences in lattice mismatch. It should be mentioned that Castell *et al.* have observed, at elevated temperatures (nearly 500 K), atomic defect states on the (100) cleavage planes of bulk NiO [36]. Similar defect states had already been detected in our previous study of NiO(100) film, but had not been described explicitly. We have also concentrated on the presence of such defect states in CoO(100) films.

The present work will demonstrate that the growth phenomena and the structural changes of the CoO film, when changing from a precursor structure to a well ordered (100) oxide layer, are very complicated and are also dependent on the layer thickness. Only for thicker films a rather uniform appearance of the surfaces was detected. In the very thin film limit (1-2 ML) the surprising variety of structures and island shapes indicates an unexpectedly large interaction between the growing film and the substrate. As already shown in the example of the NiO films grown on Ag(100) and Au(111), the substrate temperature during evaporation and the O₂ partial pressure are very important to determine the quality of the NiO films [31, 32, 37]. Heiler *et al.* systematically examined the growth of CoO films on Ag(100) and Au(111) as a function of these two parameters by means of Angle Resolved Ultraviolet Photoelectron Spectroscopy (ARUPS), Auger Electron Spectroscopy (AES), Auger Electron Diffraction (AED), LEED and show similar results [38]. The emphasis of that investigation was to determine the electronic structure of the CoO films. The present investigation is concerted on the geometric structure characterization of thin CoO films, which combines STM and Spot Profile Analysis LEED (SPA-LEED) methods. The emphasis of the investigation is to characterize the surface of the CoO films as a function of the growth parameters on an atomic scale.

The structure of the thesis is organized as follows: Chapter 2 gives an introduction to general properties of transition metal oxides and surfaces. Chapter 3 gives the

theoretical basis of LEED, both kinematic and dynamic theory are described. Chapter 4 deals with the Ultra High Vacuum (UHV) equipment used in this study and the details of sample preparation, with the data acquirement techniques applied to the LEED. In Chapter 5, the CoO film growth on Ag(100) is analyzed by SPA-LEED, and the results are discussed. The tensor LEED analysis is described in Chapter 6, with results of three systems, the clean Ag(100) surface, the 4 ML CoO/Ag(100) film and the BaTiO₃(111)($\sqrt{3} \times \sqrt{3}$)R30° reconstruction are presented and discussed. Finally, the conclusions are given in Chapter 7.

Chapter 2

Metal Oxides Surfaces

2.1 Cobalt Oxides

1. CoO

CoO (cobalt monoxide) with rocksalt structure (NaCl structure) consists of two interpenetrating fcc sublattices of Co^{2+} and O^{2-} . These two sublattices are shifted along the body diagonal by half of its length. Thus each ion has six of the other ions as its nearest neighbors as shown in Fig. 2.1. Each cubic unit cell (not the primitive unit cell) has four Co^{2+} and four O^{2-} ions. The lattice constant of CoO is 4.260 \AA [3].

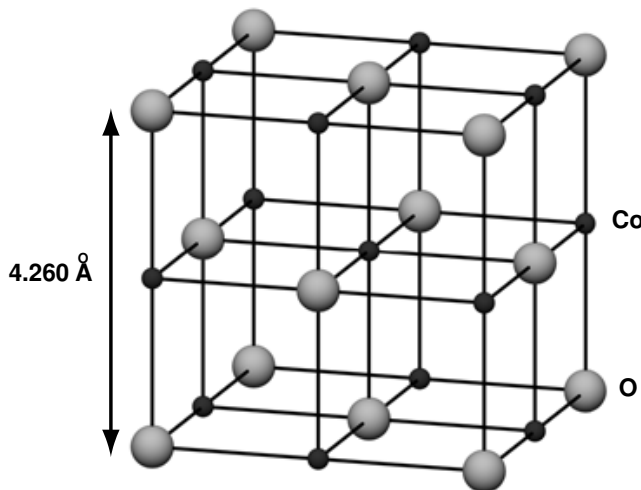


Fig. 2.1: Unit cell of CoO, which consists of two O and Co fcc sublattice lattices. Each ion has 6 of the other kind of ions in a distance of $(1/2)a_0 = 2.130 \text{ \AA}$ as its nearest neighbors, 12 ions of the same kind in a distance $(\sqrt{2}/2)a_0$ as its second nearest neighbors and again 8 ions of the other kind in a distance of $(\sqrt{3}/2)a_0$ as its third nearest neighbors.

2. Co_3O_4

CoO with Co and O atoms in a stoichiometric relationship of Co:O=1:1 is not the only binary oxide phase that forms under readily attainable oxygen partial pressures. Under common ambient conditions, the thermodynamically favored form of the cobalt oxide often is the normal spinel structure Co_3O_4 (Fig. 2.2) with a lattice constant $a_0 = 8.080 \text{ \AA}$ [39].

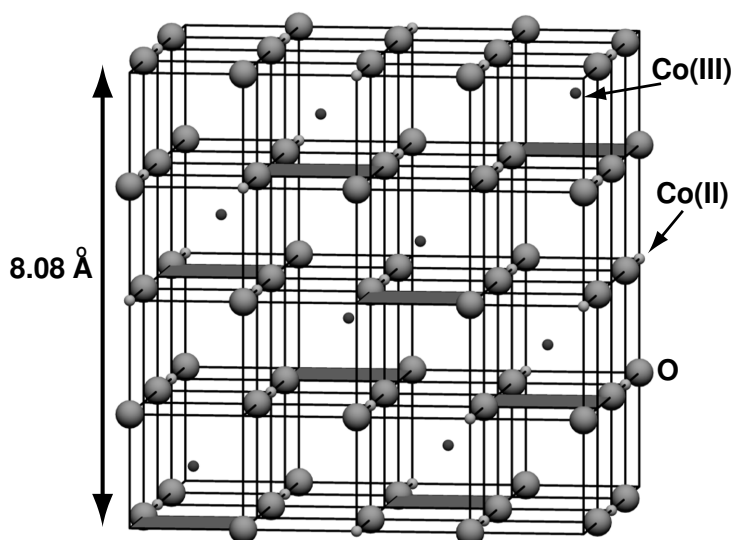


Fig. 2.2: Unit cell of Co_3O_4 with normal spinel structure. The unit cell consists of 32 O^{2-} ions, 8 Co^{2+} ions and 16 Co^{3+} ions.

Despite the simple stoichiometry of $\text{Co}:\text{O}=3:4$, Co_3O_4 with the normal spinel structure is considerably more complicated than CoO with the rocksalt structure. Unlike CoO , there are two kinds of Co ions in Co_3O_4 , tetrahedrally coordinated Co^{2+} (II) and octahedrally coordinated Co^{3+} (III). The number of Co^{2+} and Co^{3+} have a ratio of 1:2 ($\text{Co}^{2+}\text{Co}_2^{3+}\text{O}_4^{2-}$). The distance of Co-O is 1.929 Å and 1.916 Å for the tetrahedral and the octahedral site respectively, compared to 2.130 Å in CoO . The unit cell of Co_3O_4 has 8 Co^{2+} , 16 Co^{3+} and 32 O^{2-} ions, which gives a very large unit cell with a total of 56 atoms [40, 41].

3. Co_2O_3

Besides the two cobalt oxide forms mentioned above, the metastable form Co_2O_3 has been reported in the literature. However, whether the binary oxide Co_2O_3 really exists as stable solid crystal is still uncertain. In the literature [39, 42], Co_2O_3 is given as hexagonal hcp structure with lattice parameters $a = 4.640$ Å, and $c = 5.750$ Å. Similar result were obtained by Aggarwal *et al.* in 1961 for Ni_2O_3 ($a = 4.610$ Å, $c = 5.610$ Å) [43]. In contrast, Brundle *et al.* [44] have studied the interaction of oxygen and air with clean cobalt surfaces, through X-ray Photoelectron Spectroscopy (XPS) experiment and they couldn't prove the existence of Co_2O_3 .

2.2 Barium Titanate

BaTiO_3 with perovskite structure is cubic for $1460^\circ \text{C} > T > 130^\circ \text{C}$. The crystal has an O_h symmetry with a lattice constant $a_0 = 3.996$ Å and is nonpiezoelectric. Fig. 2.3 shows the cubic bulk unit cell of BaTiO_3 . The Ti^{4+} ion sits at the center of a cube with Ba^{2+} ions at the corners and O^{2-} ions at the centers of the faces. An equivalent description places Ba^{2+} at the center, Ti^{4+} at the corners, and O^{2-} at the

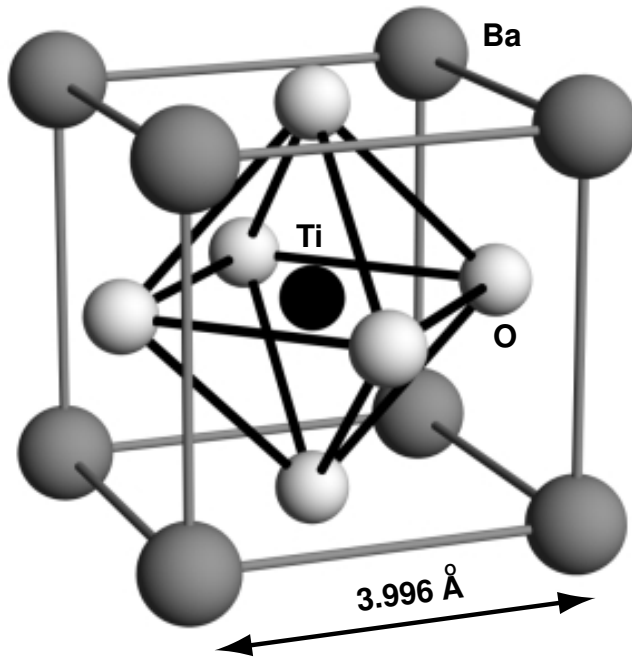


Fig. 2.3: Unit cell of cubic BaTiO_3 with Ti^{4+} sitting at the body center, Ba^{2+} at the corners, and O^{2-} at the centers of the faces. The lattice parameter of BaTiO_3 is 3.996 \AA . In the tetragonal room temperature phase the Ti and O ions are shifted in the c direction by small amounts.

centers of the edges. The ionic radii are 1.35 \AA , 0.68 \AA , 1.40 \AA for Ba^{2+} , Ti^{4+} , O^{2-} respectively. In the tetragonal room temperature phase the Ti and O ions are shifted in the c direction by small amounts.

2.3 Properties of Oxide Surfaces

Compared to metal or semiconductor surfaces, the field of oxide surfaces has only developed within the last fifteen years, due to the difficulties in preparing well controlled single crystal surfaces and implementing spectroscopic experiments to access the local atomic and electronic structures. This is the well known charging problem met in Ultra High Vacuum (UHV) based spectroscopies, which involve the emission or scattering of charged particles, such as electrons. Most of these difficulties are nowadays overcome.

Currently, the controlled fabrication of ultrathin oxide layers is opening additional new perspectives. First, it gives a solution to the charging problem, since it allows tunnelling of neutralizing electrons or holes from the substrate. More fundamentally, in growing thin films through the deposition of metal atoms and subsequent oxidation, it becomes possible to produce more open or unstable surface orientations and polar orientations than by cutting a single crystal. One can also synthesize metastable phases, or substrate stabilized phases, in regions of the bulk phase diagram, where they would be thermodynamically unstable.

Diverging Electrostatic Surface Energy. According to classical electrostatic criteria, the stability of a compound surface depends on the characteristics of the

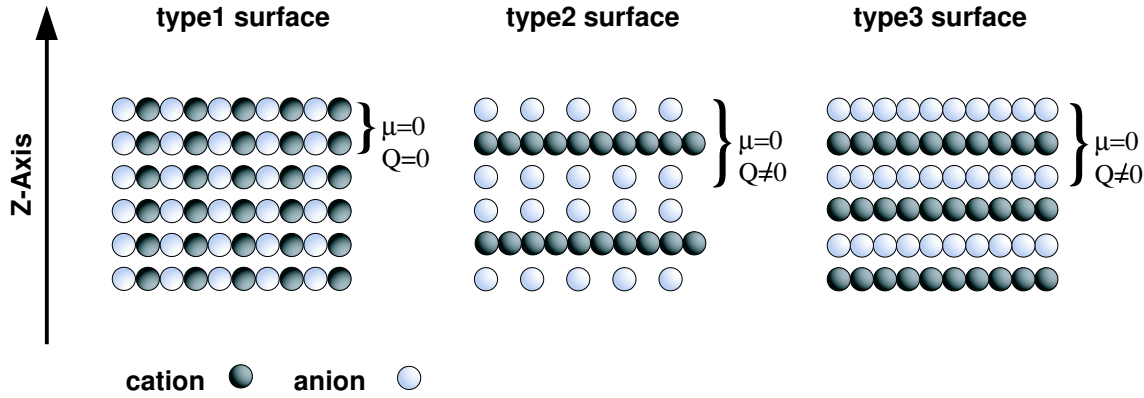


Fig. 2.4: Classification of insulating surface according Tasker [45], Q and $\vec{\mu}$ are the layer charge density and the dipole moment in the repeat unit perpendicular to the surface, respectively.

charge distribution in the structural unit, which repeats itself in the direction perpendicular to the surface as schematized in Fig. 2.4. Type 1 or 2 surfaces, which differ in the charge Q born by their layers, have a zero dipole moment $\vec{\mu}$ in their repeat unit and are thus potentially stable. In contrast, type 3 surfaces are polar and have a diverging electrostatic surface energy. This is due to the presence of a non-zero dipole moment not only on the outer layers but also on all the repeat units throughout the material [46].

The simplest representation of a crystalline compound cut along a polar direction is given in Fig. 2.5a. Two inequivalent layers of opposite charge densities equal to $\pm\sigma$ alternate along the normal to the surface, with interlayer spacings R_1 and R_2 . Each repeat unit bears a dipole moment density equal to $\mu = \sigma R_1$, and, as a result, the electrostatic potential increases monotonically across the system by an amount $\delta V = 4\pi\sigma R_1$ per double layer. δV is large, typically of the order of several tens of an eV in an ionic material. The total dipole moment $M = N\sigma R_1$ of N bilayers is proportional to the slab thickness, and the electrostatic energy amounts to $E = 2\pi N R_1 \sigma^2$. It is very large, even for thin films. In the limit $N \rightarrow \infty$, the electrostatic contribution to the surface energy per unit area diverges. This is the origin of the instability of such surfaces.

Classification of Surfaces. The classification of surfaces relies on the characteristics of the polarization in the bulk unit cell, on the surface orientation, and on the nature of the crystal termination.

In most cases, simple models for the electronic structure may easily indicate, whether a surface is polar or not. In binary compounds, for example, the difference in electronegativity of the constituents readily points to the sign of the charge transfer between the ions. The presence of a dipole moment in the repeat unit is unquestionable, whatever the charge values provided, they are non-zero. These surfaces are

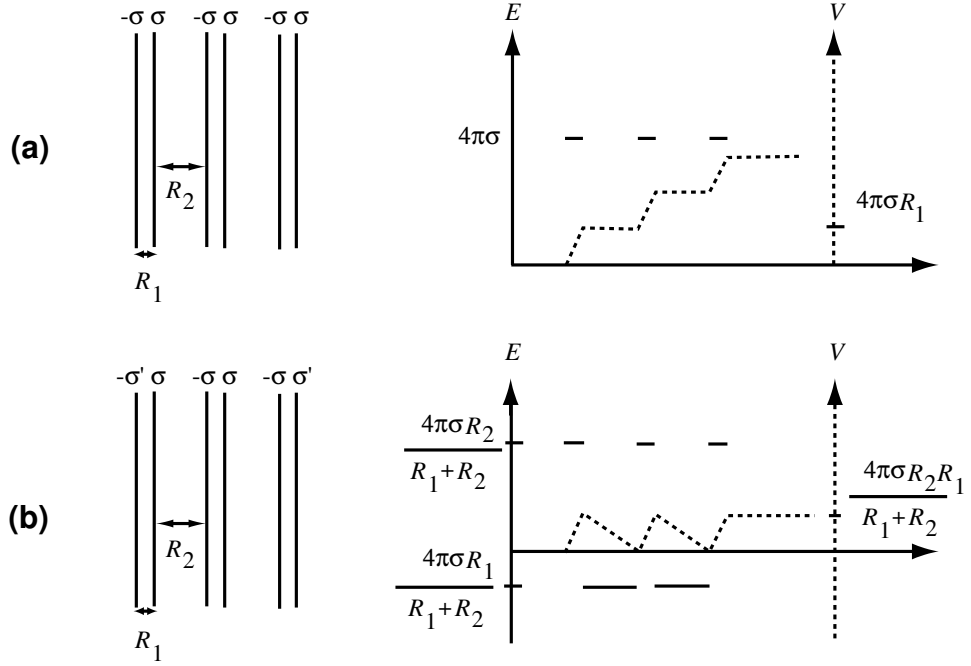


Fig. 2.5: Spatial variations of the electrostatic field E and potential V in a slab cut along a polar direction [47].

undoubtedly polar surfaces. The same is also true for some surfaces of ternary compounds, such as the (111) faces of ABO_3 perovskites. In BaTiO_3 , for example, the (111) repeat units contain alternating BaO_3 and Ti layers, which are undoubtedly charged, because, in each case, one of the layers in the repeat unit contains a single ionic constituent.

There are less obvious cases, among which is the (100) perovskite surface. In BaTiO_3 , it presents alternating layers of BaO and TiO_2 composition. If formal charges are assigned to the ions (Ba^{2+} , Ti^{4+} , and O^{2-}), then each layer is charge neutral, the repeat unit bears no dipole moment, and the orientation is considered as non-polar. This is the assertion most often encountered in the literature. However, BaTiO_3 is not fully ionic. It is on the borderline between semiconductors and insulators, and the Ti-O bond presents a non-negligible part of covalent character. The actual charges are thus probably not equal to the formal ones and there is little chance, that $Q_{\text{Ba}} + Q_{\text{O}}$ and $Q_{\text{Ti}} + 2Q_{\text{O}}$ vanish. $\text{BaTiO}_3(100)$ should thus be considered a polar surface.

Electrostatic Conditions for Cancelling the Polarity. According to classical electrostatics, ideal polar surfaces are unstable. However, specific modifications of the charge density in the outer layers may cancel out the macroscopic component of the dipole moment and cancel the polarity. Within the geometry displayed in Fig. 2.5b, this can be achieved, for example, by assigning a value $\sigma' = \sigma R_2 / (R_1 + R_2)$ to the charge density on the outer layers of the slab, and this results in a total dipole moment $M = \sigma R_1 R_2 / (R_1 + R_2)$, which is no longer proportional to the slab thickness. The

monotonic increase of the electrostatic potential is also suppressed. More generally, when m outer layers are modified ($|\sigma_j| \neq \sigma$ for $1 \leq j \leq m$ and $|\sigma_{m+1}| = \sigma$), the condition for the cancellation of the macroscopic dipole moment reads [47]

$$\sum_{j=1}^m \sigma_j = -\frac{\sigma_{m+1}}{2} \left[(-1)^m - \frac{R_2 - R_1}{R_2 + R_1} \right] \quad (2.1)$$

A polar surface can thus be stabilized provided that the charge compensation dictated by equation (2.1) is fulfilled. This implies, that either the charges or the stoichiometry in the surface layers are modified with respect to the bulk, and thus, several scenarios are conceivable that would cancel the polarity:

- One or several surface layers have compositions that differ from the bulk stoichiometry. This may lead to a phenomenon of reconstruction or terracing depending upon how the vacancies or adatoms order. However, if no ordering takes place, surface diffraction patterns exhibit a (1×1) symmetry and, unless quantitative analysis is performed, give no information on the surface stoichiometry.

- On stoichiometric surfaces, charge compensation may result from an electron redistribution in response to the polar electrostatic field. This is well exemplified in self-consistent electronic structure calculations.

- Foreign atoms or ions, coming from the residual atmosphere in the experimental setup, provide the charge compensation.

Which process actually takes place depends firstly upon energetic considerations. If stoichiometric ideal polar surfaces are not observed, this is never because their surface energy diverges. There always exist enough electronic degrees of freedom in a material to reach charge compensation through the third mechanism. However, in most cases, the resulting surface energy is high and other processes may be more efficient. If experiments are performed in thermodynamic equilibrium conditions, the observed surface configuration is that with the lowest relevant thermodynamical potential. If thermodynamic equilibrium is not reached, the observed surface configuration is that of lowest kinetically accessible energy [48].

Surface Termination and Structural Distortion. In complex oxide structures, it is generally not sufficient to know the surface orientation, because there exist several inequivalent bulk terminations. The actual termination of a surface is generally fixed by stability criteria and by the conditions of preparation, when experimental conditions are varied. For example, in the process of fabrication of ultrathin films, or under bombardment, or reducing or oxidizing conditions, some variations of stoichiometry in the surface layers may take place and polarity arguments have to be reexamined.

Among all possible terminations, some are associated with a high surface energy. This is the case for polar terminations, such as the (111) faces of rocksalt and perovskite crystals etc. Surface energies of type 1 or type 2 terminations are generally lower. Aside from this electrostatic consideration, an additional criterion of stability is

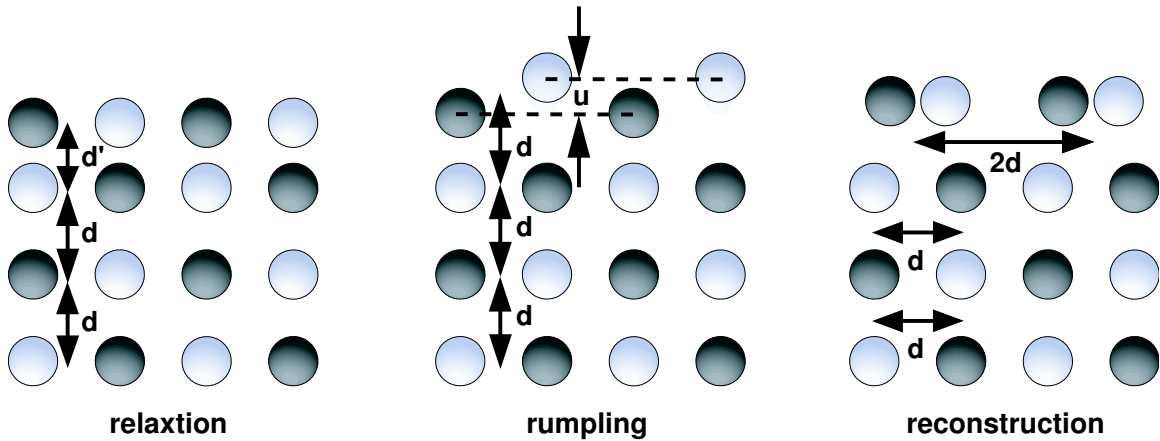


Fig. 2.6: Relaxation, rumpling and reconstruction effects. In the first two cases, the surface cell is identical to the projection of the bulk three dimensional cell but the inter-atomic distances between the surface and the underlying planes are modified. When a reconstruction takes place, the size of the surface cell changes.

provided by the number of oxygen-cation bonds that have been broken during surface formation. Since energy is required to break these bonds, the most stable surfaces are those with the smallest number of broken bonds. They are also the most compact surfaces, on which the coordination number of the atoms is not greatly reduced. For the rocksalt structure, the (100) surface, with one broken bond per surface atom, is the most stable, while the (111) orientation, with three broken bonds, has a higher surface energy and is difficult to obtain defect free.

The bond breaking process in the surface formation induces forces that push the atoms out of their bulk positions. When a two dimensional periodicity is kept in the surface layers, structural distortions will happen, which are called: relaxation, rumpling or reconstruction as shown in Fig. 2.6.

Relaxation - A relaxation is associated with a change in the spacing between the surface top layer and the underlying plane. An inward relaxation corresponds to a spacing contraction. In the opposite case, an outward relaxation takes place. Relaxation effects may, and generally do affect several layers.

Rumpling - Layers, which contain at least two types of atoms, may also rumple. For example, when the oxygen anions and the cations move in opposite vertical directions. The oxygens are often displaced outwards and the cations inwards. This effect is not induced by specific properties of the oxygen atom.

Reconstruction - A reconstruction is characterized by a change in the periodicity of the outer layer.

A lowering of the surface energy is induced by all the structural distortions, which have just been described. It must be taken into account when comparing the relative stability of different faces of a given material.

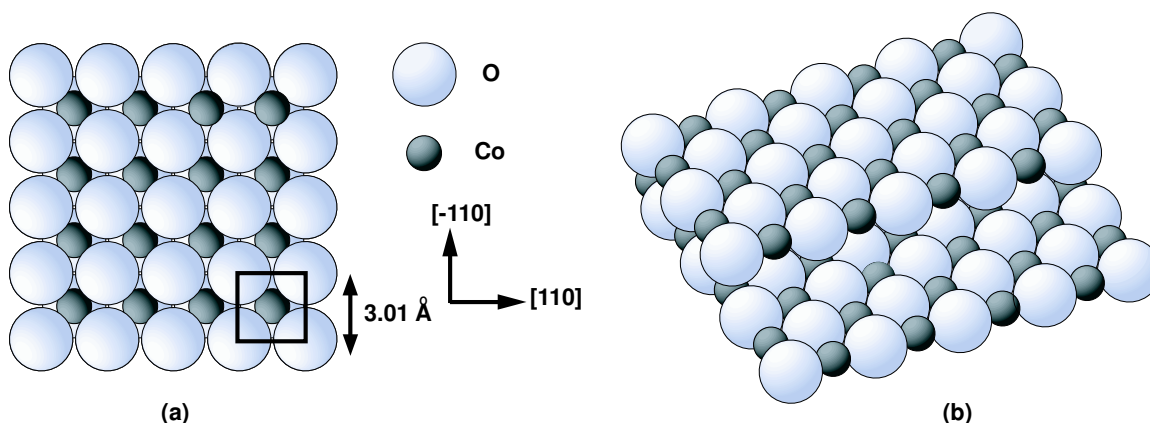


Fig. 2.7: (a) Model of the CoO(100) surface. (b) Side view of a $\langle 100 \rangle$ step on this surface, both ions are six-fold coordinated in the bulk of the crystal while the coordination number on (100) terraces is five and only four at step edges.

2.4 Cobalt Oxide Surfaces

CoO(100) surface. The CoO(100) surface structure model is represented in Fig. 2.7a, the primitive surface unit cell contains a Co^{2+} and an O^{2-} ion. Each surface atom is five-fold coordinated, while they occupy octahedral sites in the bulk. The alternating layers are equidistant ($R_1 = R_2$) containing an equal number of Co^{2+} and O^{2-} ions. Thus, they are neutral and belong to type 1 surfaces.

The CoO(100) surface can be easily prepared by cleavage. STM investigations of the (100) cleavage surfaces of CoO single crystals reveal atomically flat terraces separated by monatomic steps that run in $\langle 001 \rangle$ directions. A model of the steps in $\langle 001 \rangle$ directions show in Fig. 2.7b. The terraces generally have a low defect density and are arranged in a bulk terminated (1×1) structure as determined by STM. The terrace widths generally are between 50 \AA and 300 \AA [49].

A LEED $I - V$ analysis was performed on a UHV cleaved CoO(100) surface and the surface looked like a termination of the bulk [50]. Sample charging limited the incident electron energy that could be used to above 170 eV, thereby restricting the data base and hence the accuracy of the determination. The surface atomic plane was found to be at the ideal bulk location to within $\pm 3\%$ of the interlayer spacing [50]. The bulk termination result was also confirmed by Helium Atom Scattering (HAS). A step height h of $2.15(\pm 0.05) \text{ \AA}$ was evaluated, in good agreement with the ideal bulk layer spacing of 2.13 \AA [51].

The same type of experimental and LEED $I - V$ analysis was performed on UHV cleaved NiO(100), MgO(100) and CaO(100) surfaces, which all have rocksalt structure (100) surfaces. The conclusions are similar to those for CoO(100). Within $\pm 5\%$ rumpling of the surface plane occurs on a scale detectable by LEED analysis, and the outermost plane of ions is relaxed inward within 3% of the interlayer spacing.

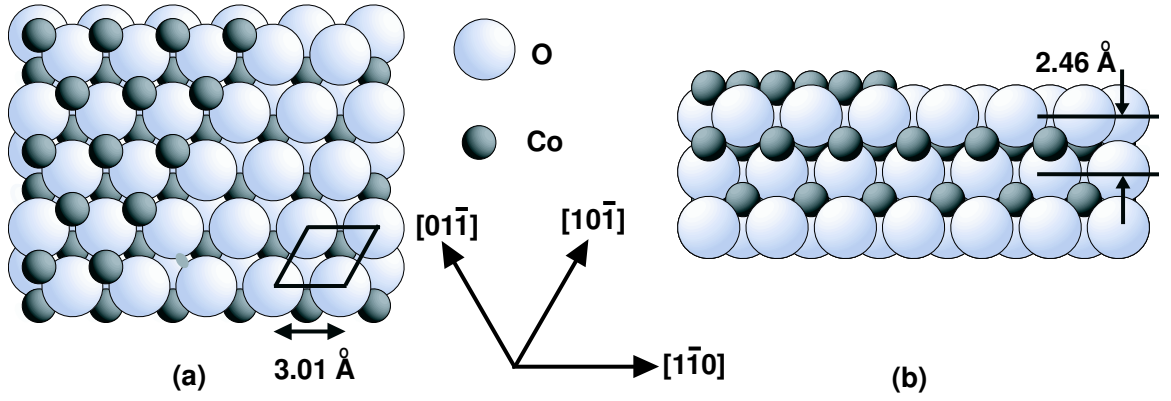


Fig. 2.8: (a) Schematic representation of unreconstructed CoO(111) surface. (b) Side view.

These conclusions are supported by shell model calculations of the surface structure. The atomically flat character of CoO(100), CaO(100), MgO(100) and NiO(100) is somewhat surprising in view of the variations in ionicity and cation polarisability between these materials. It is conceivable, that they may have in common an enhanced covalency of the surface O ions, which leads to a very similar ionic arrangement for these surfaces as discussed by Prutton *et al.* [52].

Concerning the electronic structure of the CoO surface, the theoretical description is still a matter of discussion mainly due to the importance of the correlation of the cobalt 3d electrons. Another difficulty is the mixing of cobalt and oxygen states in the valence band region. In both of the theoretical approaches (local density approximation band structure calculations and *ab initio* cluster calculations) it is difficult to take all of these aspects into account appropriately. Previous experimental investigations of the electronic structure of CoO were mainly performed on single crystal CoO surfaces by means of photoemission [53, 54]. Recently, we have prepared ordered thin films of CoO by evaporating cobalt in an O₂ atmosphere on to a heated (500 K) Ag(100) substrate. The geometric and electronic structures of the films were characterized by means of AED and ARUPS, respectively. The experimental AED results were compared with simulated data, which showed that the film grows in (100) orientation on the Ag(100) substrate. ARUPS investigations confirmed the chemical identity of CoO and the bulk like electronic structure of the film [55].

CoO(111) surface. Fig. 2.8 schematically shows the (111) surface of CoO. This surface is not a natural cleavage plane of CoO with rocksalt structure. It is shown idealistically, as no reconstruction or surface charge reduction to stabilize the surface has been taken into account here. The surface atoms are threefold coordinated. A crystal cut along (111) presents alternating layers of Co²⁺ and O²⁻ composition, which are equidistant ($R_2 = R_1$). In an ionic picture, the two-dimensional unit cell bears a charge of ± 2 , so a reduction of charge by a factor of 2 is required in the outer layers, according to equation (2.1). When charge compensation is provided by

changes in stoichiometry, simple electrostatic arguments suggest two stable surface configurations. One is obtained by removing every other atom in the outermost layer, which yields a missing-row surface structure with a $p(2 \times 1)$ reconstructed unit cell. This configuration may be thought of as a stacking of non-dipolar Co/2O/Co repeat units, with zero inter-unit distance. The second stable surface configuration, called the octopolar $p(2 \times 2)$ reconstruction, is obtained by removing 75% of the atoms in the outermost layer and 25% in the layer beneath, in a way which produces (100) nano-facets [28].

The NiO(111) surface, which is chemically quite similar to CoO(111) surface, is relative intensively studied in literature. Single crystal NiO(111) surfaces [56, 57] as well as thin NiO(111) films grown on various substrates such as Ni(100) [58], Ni(111) [25, 26], and Au(111) [59, 60] have been studied. No reconstruction was found for NiO(111)/Ni(100). LEED $I - V$ analysis has suggested that the terminal layer is made of oxygen atoms and is strongly relaxed inwards (14.8%) [58]. All other NiO(111) surfaces considered present $p(2 \times 2)$ LEED patterns, usually attributed to the octopolar reconstruction. This finding was independent of whether the films were grown by oxidation of a Ni(111) surface or on Au(111). The lattice mismatch between NiO(111) and Au(111) is smaller than with Ni(111), and the films are of better quality. STM experiments furthermore suggested that the surface is terminated by a single type of atoms, due to the presence of steps of a single unit cell height [59, 60].

Grazing Incidence X-ray Diffraction (GIXD) experiments have been performed on single crystal NiO(111) samples [57]. For air annealed samples, the structural refinement indicates that the $p(2 \times 2)$ surface is terminated by Ni atoms, as predicted by molecular dynamics simulations of the surface [61]. In contrast, as shown recently, both metastable O and thermodynamically stable Ni terminations may co-exist, separated by single steps, on NiO(111)/Au(111) films 5 ML thick [62]. After in situ annealing and oxidation, however, the $p(2 \times 2)$ single crystal surface is better described as a Ni₃O₄ inverse spinel structure.

The $p(2 \times 2)$ surface reconstruction of NiO(111)/Ni(111) disappears in the presence of water [26]. This effect was attributed to the stabilizing presence of hydroxyl groups adsorbed on the outer layers, which provides exact charge compensation. A reversible transition between the reconstructed and the non-reconstructed surfaces was evidenced [25]. These results support the idea that the polar orientation of NiO is more reactive than the (001) cleavage face. However, on NiO(111)/Au(111) surfaces, no reconstruction takes place when the film is exposed to a water atmosphere. Recent attempts to decompose water on a single crystal NiO(111) surface also failed and suggest that water decomposition only takes place on defective surfaces [62].

Several studies on CoO(111) surfaces have been published. An early dynamical LEED analysis of a single crystal CoO(111) surface interprets the experiment in terms of the bulk structure with a terminating O plane [63]. While the reasons for the existence of the (111) films have been discussed controversially, this surface must

be stabilized by a more complex defect structure or by the thinness of the oxide layer. This interpretation has been criticized by Prutton and Welton-Cook. Their explanation lies in the reduction of the dipolar electric field due to the image charge induced in the metal substrate [52, 63]. Thin cobalt oxide films have been obtained through oxygen chemisorption on Co(0001) and heating. Epitaxial CoO(111) layers have been produced. However, beyond some critical temperature and at high oxygen exposures, Co₃O₄(111) layers are formed [64]. The same sequence occurs when a Pt alloy containing about 20% of cobalt is oxidized [65].

Recently, ultrathin CoO(111) films have been synthesized either by oxidation of Co(0001) [66, 67] or by deposition and oxidation of metallic atoms on Au(111) substrates [68, 69]. The CoO surface displays a (1 × 1) LEED diagram, probably due to the presence of hydroxyl groups. Attempts to remove them without damaging the film were not successful. The combined use of High Resolution Electron Energy Loss Spectroscopy (HREELS) and Near Edge X-ray Absorption Fine Structure (NEXAFS) to probe NO adsorption on CoO(111) has suggested that the surface is metal terminated, in contrast to NiO(111), which can have O-terminated terraces, a difference tentatively attributed to the more covalent character of the metal-oxygen bond in CoO [67].

Co₃O₄ Surface. As revealed by GIXD experiments, the (111) surface of a CoO single crystal is covered with an epitaxial Co₃O₄(111) layer of spinel structure, with the epitaxial relationships Co₃O₄(111)||CoO(111) and Co₃O₄(100)||CoO(100). Air annealing of the surface, as well as UHV annealing and Ar⁺ bombardment, lead to the creation of metallic Co islands but cannot restore the CoO stoichiometry [70].

Valence-band photoemission studies have been performed on a CoO(100) single crystal as it is slowly oxidized under 1×10^{-4} Torr O₂ at 623 K, eventually forming a Co₃O₄ epitaxial film. The most significant changes occur in 3*d* related features, with the peak located at the top of the valence band sharpening and shifting to lower binding energies as the spinel oxide forms. Constant initial-state measurements indicate that Co₃O₄ contains an admixture from neighboring O 2*p* to its 3*d* band, as observed for CoO and other monoxide charge-transfer insulators. The peak at the top of the Co₃O₄ valence band results from the 3*d*⁶L final state of the octahedral Co³⁺ 3*d* band. The Co³⁺ 3*d*^{*n*-1} satellite is much less intense in Co₃O₄ than in CoO, as is observed for the analogous structure in the cobalt 2*p* core spectra [71].

2.5 Barium Titanate Surfaces

BaTiO₃(100) surface. Fig. 2.9 presents an ideal model of the BaTiO₃(100) surface. The surface can exhibit either a BaO or a TiO₂ termination, the alternating layers are equidistant ($R1 = R2$), and as already mentioned they are not neutral. This surface is the prototype of what is called 'weakly polar surfaces' [72]. The electrostatic condition

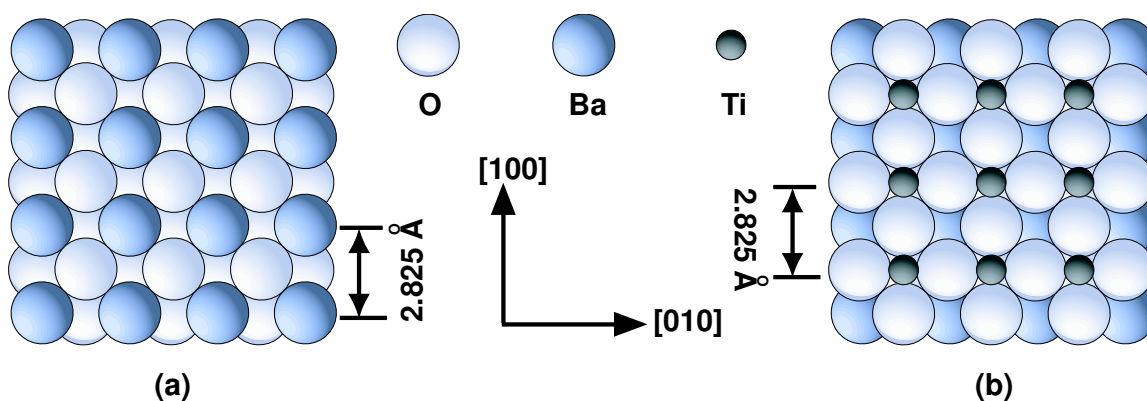


Fig. 2.9: Model of perovskite $\text{BaTiO}_3(100)$ surface. (a) BaO termination. (b) TiO_2 termination. On the BaO surface, the large Ba cations have eight O ligands, compared with twelve in the bulk. On the TiO_2 surface, the smaller Ti cations are five-fold coordinated with O ions.

for surface stability is $\sigma' = \sigma/2$. In practice, any real cleaved surface would consist of equal areas of terraces having each of the two compositions, separated by steps. The BaO and TiO_2 surfaces may, however, have different surface energies, so surfaces prepared by ion bombardment cleaning and annealing might have different ratios of the two types of surfaces. On the BaO surface, the large Ba cations have eight O ligands, compared to twelve in the bulk. On the TiO_2 surface, the smaller Ti cations are five-fold coordinated with O ions.

Investigations of the $\text{BaTiO}_3(100)$ surface using STM and LEED revealed (2×1) and $(\sqrt{5} \times \sqrt{5})R26.6^\circ$ superstructures [73–75]. Measurements on annealed natural growth faces showed complex, streaked patterns for annealing temperatures below 1100 K. Annealing at 1123 K produced (1×1) patterns characteristic of the bulk, but when the annealing temperature was increased to 1273 K, a $(\sqrt{5} \times \sqrt{5})R26.6^\circ$ structure appeared. Some samples that were treated to give the (1×1) pattern exhibited hysteresis of some of the beam intensities as a function of temperature between 300 and 923 K, and it was suggested that this might be explained by the existence of two surface layer geometries, one cubic and one tetragonal, as a function of temperature [76].

LEED observations have also been made on $\text{BaTiO}_3(100)$ samples that were bombarded with O^+ ions and subsequently annealed at 1273 K. Such surfaces showed good quality (1×1) patterns. Samples that were bombarded with Ar^+ ions and then annealed at 1273 K exhibited fractional order spots indicating two mutually perpendicular (2×1) LEED patterns [73]. It was found that the BaTiO_3 surface was readily reduced by ion bombardment and that subsequent annealing did not necessarily result in the restoration of a stoichiometric surface [77].

Based on an investigation of the $\text{SrTiO}_3(100)$ surface using Reflection High Energy Electron Diffraction (RHEED) and STM, the superstructures observed were assigned

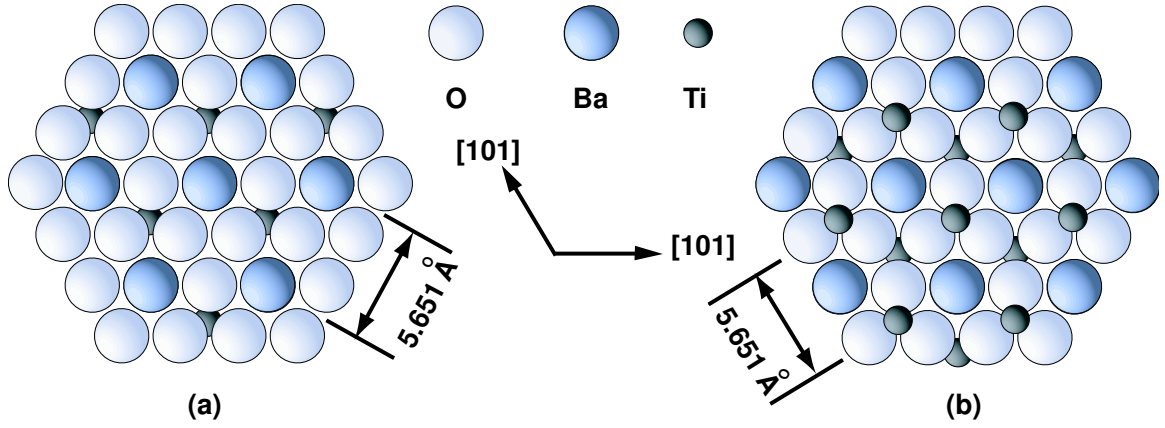


Fig. 2.10: The $\text{BaTiO}_3(111)$ surface consists of alternating BaO_3 and Ti layers. The surface unit cell is 5.65 \AA long, which is the distance between neighboring Ba and Ti atoms on the BaO_3 and Ti terminated surfaces. The left (a) exhibits the BaO_3 termination, where each Ba atom is coordinated by six O atoms in the top layer. The right (b) shows the Ti termination with Ti atoms only. Each Ti atom is coordinated by three O atoms of the underlying BaO_3 layer. Note the close packed structure of the BaO_3 terminated surface and the rather open structure of the Ti terminated one.

to a TiO_2 terminated surface [78]. With UPS and STS investigations these superstructures and corresponding midgap states on both the $\text{BaTiO}_3(100)$ and the related $\text{SrTiO}_3(100)$ surface were attributed to an ordering of Ti^{3+} ions and O vacancies complexes [73, 75]. These complexes are produced by annealing samples at high temperatures under UHV conditions, which is the usual procedure to obtain conducting samples, suitable for investigations with charged particles or STM. However, the geometrical arrangement of atoms in these complexes of Ti^{3+} atoms and O vacancies has not been determined, yet.

Several ab initio theoretical calculations were performed to study the relaxation of $\text{BaTiO}_3(100)$ surfaces [79–81]. In all these works, the TiO_2 top layer is slightly more stable than the BaO one, and a large polarization of ions in the first two layers of the surface was found. Even if the TiO_2 terminated surface is more stable than the BaO terminated surface, the two types of surfaces could still coexist. This is confirmed experimentally on $\text{SrTiO}_3(100)$ surfaces by means of a LEED $I - V$ analysis [23].

$\text{BaTiO}_3(111)$ Surface. Fig. 2.10 shows a $\text{BaTiO}_3(111)$ surface with its two bulk-like terminations. The left (a) is Ba-O terminated, with Ba ions in a surface unit cell mesh. In the top layer each Ba ion is coordinated by six O ions, which in turn form bridges between neighboring Ba ions. This structure leads to an O-rich BaO_3 composition in the top surface layer and a negatively charged surface. The right (b) is Ti terminated and consists of Ti ions only, again in a unit cell mesh. This termination is O-deficient and positively charged. The Ti ions do not bond to other ions of the top layer, because the distance (5.651 \AA) to the next ion (a Ti ion) is too large. Therefore,

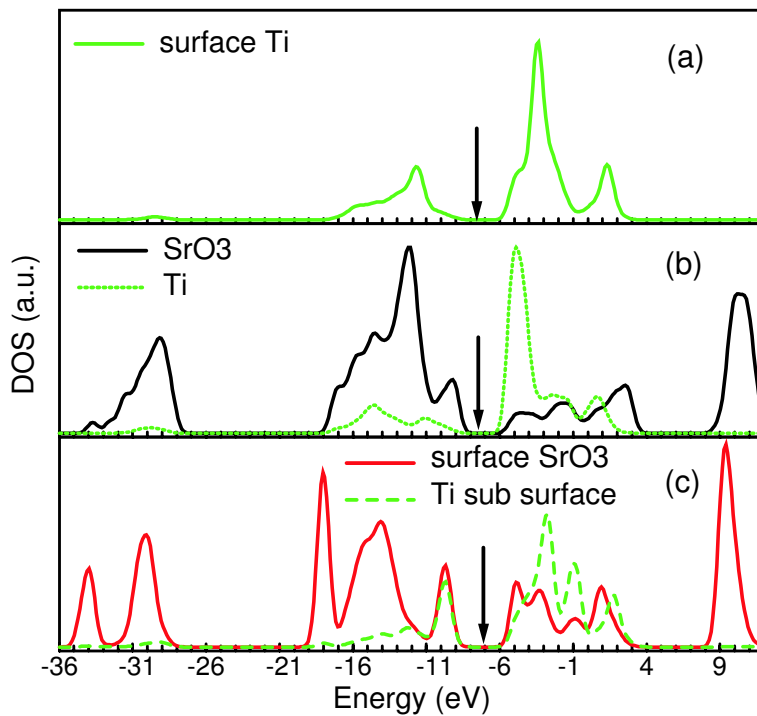


Fig. 2.11: The local density of states of a SrTiO_3 slab containing stoichiometric SrO_3 and Ti layers: (a) the Ti-termination projected DOS; (b) the bulk DOS; (c) the SrO_3 -termination projected DOS; all DOS have been convoluted with a 0.5 eV wide Gaussian function. Note the enhanced contribution of the valence DOS on the outer Ti on the Ti termination and on the sub-surface Ti on the SrO_3 termination, and the overall insulating character of the surface layers (the Fermi level is indicated by an arrow) [82].

they are coordinated only by three O ions of the Ba-O layer below. Both terminations are polar with equidistant layers ($R_1 = R_2$) in their repeat unit, of the Ti- BaO_3 type. The layers formally bear charge densities equal to ± 4 per surface unit cell and require compensating charges equal to ± 2 . It is to be expected that the excess charge on either bulk-like terminated surface and the mismatch in stoichiometry of oxygen and the respective metal lead to high surface energies for both such surface terminations which makes surface reconstructions very likely. Another striking difference between the two terminations is that the Ti terminated surface with only one ion per surface unit cell is more open than the Ba-O terminated one with four ions per unit cell.

$\text{BaTiO}_3(111)$ and $\text{SrTiO}_3(111)$ surfaces have been produced and studied. A well ordered (1×1) $\text{SrTiO}_3(111)$ surface was prepared by Ar^+ bombardment and subsequent annealing below 1100 °C [83,84], with the top layer being of either SrO_{3-x} or Ti composition. There is no evidence of surface states in the bulk projected band gap. In references [83,85], surface atoms with anomalous charge states were detected by core level spectroscopy. It is a remarkable finding that the $\text{SrTiO}_3(111)$ surface does not reconstruct, although one might expect a large enough 'driving force' for

reconstructions, since both of the two bulk-like terminated (111) surfaces are polar and not charge compensated.

The atomic and electronic structures of $\text{SrTiO}_3(111)$ (1×1) surfaces have been investigated using a total-energy, semi-empirical Hartree-Fock method [82, 86]. Terminations of various stoichiometries, whether compensated or not, exhibit strong electron redistributions, which suppress the macroscopic component of the dipole moment (see Fig. 2.11). For stoichiometric non-compensated surfaces (e.g. SrO_3 or $\text{Ti}(111)$ layers), this is an expected result, but redistributions are also present on stoichiometry-compensated surfaces (e.g. SrO_2 or $\text{TiO}(111)$ layers), leading to an anomalous filling of surface states and anomalous charge states for some surface atoms. All terminations were found to be insulating, a result attributed to the specific value ± 2 of the compensating charges, which allows the complete filling of one surface state per unit cell. The average surface energies were found to be rather low, consistent with the possibility of the fabrication of planar (1×1) $\text{SrTiO}_3(111)$ surfaces. The relative stabilities of terminations of different stoichiometries were calculated as a function of oxygen chemical potential and it was anticipated that non-stoichiometric reconstructions are not necessarily efficient mechanisms for stabilizing the surface.

On $\text{BaTiO}_3(111)$ surfaces, we found various superstructures depending on the preparation procedure. In detail, vacuum annealing resulted in a $(\sqrt{3} \times \sqrt{3})R30^\circ$ superstructure and annealing in oxygen lead to a mixture of (1×1) and (2×2) [87]. Subsequent vacuum annealing produced a mixture of $(\sqrt{3} \times \sqrt{3})R30^\circ$ and (2×2) structures. This indicates that conclusions about the $\text{SrTiO}_3(111)$ surface are not necessarily valid for the $\text{BaTiO}_3(111)$ surface: the surface stoichiometry, and hence the geometrical structure, depends more critically on preparation parameters, like annealing temperature and oxygen partial pressure, than that of the $\text{SrTiO}_3(111)$ surface.

Chapter 3

Theory of Low Energy Electron Diffraction

Low Energy Electron Diffraction (LEED) is one of the first and one of the most successful surface science techniques for structure determination ever invented. For more than 50 years it has been the dominant method to study the structure and morphology of two dimensional plane surfaces. From its invention in 1927 by Davison and Germer [88] until today a vast variety of very different techniques and extremely sophisticated applications have been developed.

For the structure analysis of atomic positions in the surface unit cell, LEED $I - V$ analysis has been developed with an accuracy of less than a few hundreds Å. Furthermore, the determination of complex surface structures has been automated [89]. Besides the intensities of the diffraction spots also the profile and position contain important information about the surface morphology, which can be analyzed by Spot Profile Analysis LEED (SPA-LEED) [90]. In the following, both the kinematic and dynamic theory of LEED will briefly be described since the SPA-LEED analysis is based on the kinematic theory whereas the tensor LEED analysis based on the dynamic theory and both will be used in this thesis.

3.1 Kinematic LEED Theory

The diffraction from surfaces may be described as a sum of electron wave functions scattered from the initial wave vector \vec{k}_i of the incoming electron to the final wave vector \vec{k}_f by all surface atoms at positions $\vec{r}(\vec{n})$

$$\Psi(\vec{K}, \vec{k}_i) = \sum_n f(\vec{n}, \vec{K}, \vec{k}_i) e^{i\vec{K}\vec{r}(\vec{n})} \quad (3.1)$$

where $\vec{K} = \vec{k}_i - \vec{k}_f$ is the scattering vector and $f(\vec{n}, \vec{K}, \vec{k}_i)$ the structure factor, which depends both on the initial \vec{k}_i and final electron wave vector \vec{k}_f . The structure factor combines the electron waves coming from the surface atom at $\vec{r}(\vec{n})$ and all underlying atoms in the column perpendicular to the surface.

The diffraction phenomena with the diffraction spot intensity

$$I(\vec{K}, \vec{k}_i) = |\Psi(\vec{K}, \vec{k}_i)|^2 = \sum_{n,m} f(\vec{n}, \vec{K}, \vec{k}_i) f^*(\vec{m}, \vec{K}, \vec{k}_i) e^{i\vec{K}(\vec{r}(\vec{n}) - \vec{r}(\vec{m}))} \quad (3.2)$$

are mainly determined by the scattering cross section, i.e. the values of the structure factor $f(\vec{n}, \vec{K}, \vec{k}_i)$.

The infinite periodicity parallel to the surface results in extremely well defined reciprocal lattice vectors \vec{K}_{\parallel} . On the contrary, in the direction perpendicular to the surface, electrons in a LEED experiment are elastically scattered within a depth of only a few atomic layers due to strong electron-electron interactions. The lack of a well defined periodicity perpendicular to the surface relaxes the selection rule for \vec{K}_{\perp} , almost any value of \vec{K}_{\perp} is possible. Therefore the reciprocal lattice in a LEED experiment is well described by a periodic arrangement of lattice rods.

The finite penetration depth of the electrons together with the dominating multiple scattering effects influences the intensity via the structure factor $f(\vec{n}, \vec{K}, \vec{k}_i)$ as a function of the initial \vec{k}_i and the final scattering vector \vec{k}_f .

Dynamic LEED theory is necessary to describe the dependence between the geometric atomic structure in the unit cell and the intensities $I(\vec{K}, \vec{k}_i)$ of the diffraction spots as a function of electron energy and incidence angle. This whole field of atomic structure determination by LEED $I-V$ analysis for smooth and homogeneous surface will be described in section 3.2.

For simplicity reasons the kinematic approximation is used for the spot profile analysis of rough or stepped surfaces. Pendry *et al.* [91] have discussed multiple scattering effects of disordered surfaces. However, up to now, it is still too complicated to consider different structure factors $f(\vec{n}, \vec{K}, \vec{k}_i)$ for the diffraction from disordered step edges of rough surfaces.

All structure factors are replaced by their spatial average (3.3)

$$f = f(\vec{K}, \vec{k}_i) = \langle f(\vec{n}, \vec{K}, \vec{k}_i) \rangle_n \quad (3.3)$$

independent on the site of a particular unit cell and the arrangement of the neighboring unit cells. This approximation is strictly valid for a smooth and flat surface. However, small deviations may be expected at crystal positions without translational symmetry, i.e. at step edges. Considering the unit cell columns just at the step edge, it becomes clear that the surrounding atomic configurations are different as shown in Fig. 3.1. Electrons scattered directly from below and above the step edge undergo different structure factors. Due to the very limited electron penetration depth of less than 5 Å only such a small band around a step edge may show up a different structure factor. Electrons scattered from unit cells further away than 5 Å from the step edge are simply insensitive to it and exhibit all the same structure factor f . Therefore, this approximation is the better, the larger the separation between steps. With decreasing

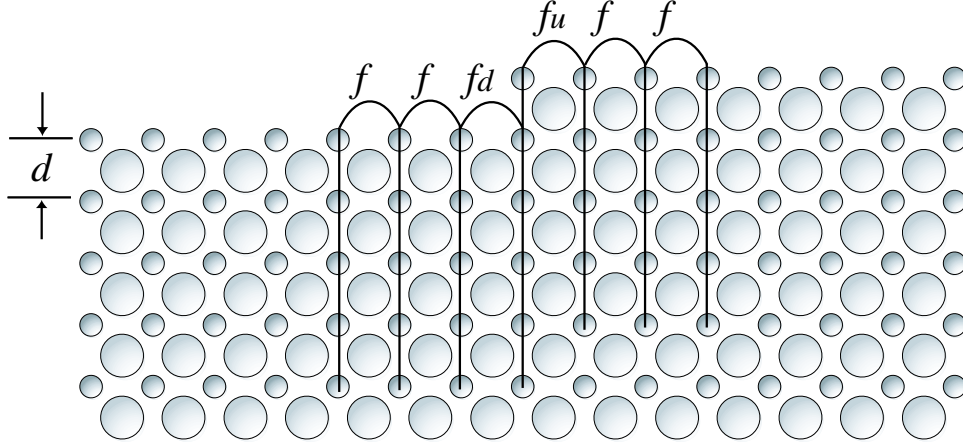


Fig. 3.1: At a step edge the structure factor f deviates from its average value. f_u and f_d may show different scattering amplitudes and scattering phases.

step density also the areas with a different structure factor decrease and consequently their influence on the spot profile.

The intensity splits up

$$I(\vec{K}, \vec{k}_i) = F(\vec{K}, \vec{k}_i)G(\vec{K}) \quad (3.4)$$

into the dynamical form factor, which depends on the initial and final wave vector

$$F(\vec{K}, \vec{k}_i) = |f(\vec{K}, \vec{k}_i)|^2 \quad (3.5)$$

and the well known lattice factor, which is only determined by the surface morphology and the scattering vector \vec{K}

$$G(\vec{K}) = \left| \sum_n e^{i\vec{K}\vec{r}(\vec{n})} \right|^2 \quad (3.6)$$

The lattice factor $G(\vec{K})$ does not modify the integral intensity of the spots, it influences the intensity distribution in reciprocal space. A perfectly smooth, flat surface shows up with perfectly sharp diffraction spots, which are only instrumentally broadened. However, any deviation from a perfect translational symmetry such as a step edge or an island results in a redistribution of intensity from the sharp fundamental diffraction spots into diffuse intensity between the LEED spots [92, 93]. For a rough surface spot broadening is observed, for a regular step train spot splitting, and for facets new fundamental spots [94].

The total intensity of the diffuse and peaked part of a particular spot i, j is conserved and normalized to 1 by the number N of surface unit cells and is independent on the surface morphology and independent on K_\perp :

$$\int_{Bz} d\vec{K}_\parallel G_{ij}(\vec{K}) = 1 \quad (3.7)$$

This is of very special importance for the spot profile analysis and is essential for the practical data evaluation. The lattice factor $G_{ij}(\vec{K})$ is obtained from the intensity $I_{ij}(\vec{K})$ of LEED spot i, j . The absolute value of the spot intensity is not evaluated, only the variation of the spot profile with \vec{K} . The lattice factor $G_{ij}(\vec{K})$ is obtained by normalization of the experimentally measured intensity profile $I_{ij}(\vec{K})$ with the total integral intensity of the spot i, j

$$\frac{I_{i,j}(\vec{K})}{\int d\vec{K}_{\parallel} I_{i,j}(K_{\parallel})} = \frac{F(\vec{K}, \vec{k}_i)G(\vec{K})}{\int_{Bz} d\vec{K}_{\parallel} F(\vec{K}, \vec{k}_i)G(\vec{K})} \cong \frac{F(\vec{K}, \vec{k}_i)G(\vec{K})}{\bar{F}_{i,j}(\vec{k}_i) \int_{Bz} d\vec{K}_{\parallel} G(\vec{K})} \quad (3.8)$$

$$= \frac{F(\vec{K}, \vec{k}_i)G(\vec{K})}{\bar{F}_{i,j}(\vec{k}_i)} \cong G(\vec{K}) \quad (3.9)$$

This intensity profile is also modulated by the dependence of the dynamic form factor $F(\vec{K}, \vec{k}_i)$ on the electron energy E , the angle of incidence φ of the electron beam and the scattering vector \vec{K} . Recording a spot profile usually only the scattering vector \vec{K} is varied. For the analysis it is usually assumed that the variation of $F(\vec{K}, \vec{k}_i)$ with \vec{K} is much smoother than that of the lattice factor $G_{i,j}(\vec{K})$, i.e. that $F(\vec{K}, \vec{k}_i) = \bar{F}_{i,j}(\vec{k}_i)$ is constant with respect to \vec{K} around the spot i, j in reciprocal space, where diffuse intensity is observed.

This approximation is the better, the larger the observed morphological features are, because the diffuse intensity will be confined to a smaller region around the spot i, j . The kinematic approximation works best for large morphological structures. However, the observation of such large structures requires a high resolution instrument.

Of special importance are conditions, when the structure factor equals zero: the different scattering amplitudes from atoms of the unit cell annihilate each other (complete destructive interference). Small changes of the initial or final wave vector will immediately disturb the cancellation: intensity is observed and may strongly vary by orders of magnitude for small variations of the scattering vector \vec{K} . This effect does not happen for strong intensity conditions, when the scattering amplitudes of most atoms of the unit cell interfere constructively. Changes of the energy and scattering vector will also affect this situation and may also modify the intensity. However, the relative changes of the structure factor with \vec{K} or \vec{k}_i will be small, and will only become large, if the structure factor varies strongly or is close to zero.

The lattice factor could also be expressed by the absolute square of the two dimensional Fourier transform

$$G(\vec{K}) = \frac{1}{2\pi} \left| \sum_n e^{iaK_{\parallel}\vec{n}} \varphi(K_{\perp}, \vec{n}) \right|^2 \quad (3.10)$$

of the surface phase function

$$\varphi(K_{\perp}, \vec{n}) = e^{idK_{\perp}h(\vec{n})} \quad (3.11)$$

This equation highlights the maximum obtainable morphological information: The surface height function $h(\vec{n})$ is in principal not accessible, only its projection on the unit circle of complex numbers could be determined. Due to the modulo properties of the complex exponential with 2π this causes some ambiguous results, if the spot profile is determined only for a single value of K_{\perp} . For an unambiguous determination of the surface morphology $h(\vec{n})$ the lattice factor $G(\vec{K})$ must be known for different values of K_{\perp} .

The scattering phase S replaces the vertical scattering vector as dimensionless value (independent on the particular material)

$$S = K_{\perp}/2\pi \quad (3.12)$$

$$\varphi(S, \vec{n}) = e^{i2\pi S h(\vec{n})} \quad (3.13)$$

The scattering phase S describes the phase difference in numbers of the electron wavelength λ , when electrons are scattered from adjacent terraces with a height difference of one atomic step d .

$$\lambda = (h^2/2m_e e E)^{-1/2} \quad (3.14)$$

Electrons interfere constructively for integer S , i.e. the Bragg or "in-phase" condition of scattering. For this conditions they are not sensitive to any surface roughness. Therefore, a sharp LEED spot is expected for electrons with an energy corresponding to a Bragg condition.

For the "out-of-phase" or anti-Bragg condition the electrons interfere destructively and are most sensitive to surface roughness. The electrons are not annihilated from the sharp LEED spot, but redistributed into a diffuse part surrounding the sharp spot. The shape or profile of such a broadened spot is determined by the lattice factor $G(\vec{K})$.

For the (00) spot, i.e. $\vec{K}_{\parallel} = 0$, and an arbitrary incidence angle the scattering phase S depends as follows on the electron wavelength

$$S = 2d \cos(\vartheta)/\lambda \quad (3.15)$$

or electron energy

$$S = 2d \cos(\vartheta) \sqrt{E(eV)/150.4} \quad (3.16)$$

Though the electrons gain energy during the scattering process due to the inner potential V_0 . of the crystal, the interference conditions described by the scattering phase S are not affected. Each electron undergoes the same constant phase shift due to the inner potential.

Therefore, the accurate and absolute determination of vertical layer distances is possible for a rough surface via the position of the "in-phase" conditions, i.e. the three dimensional Bragg conditions [94].

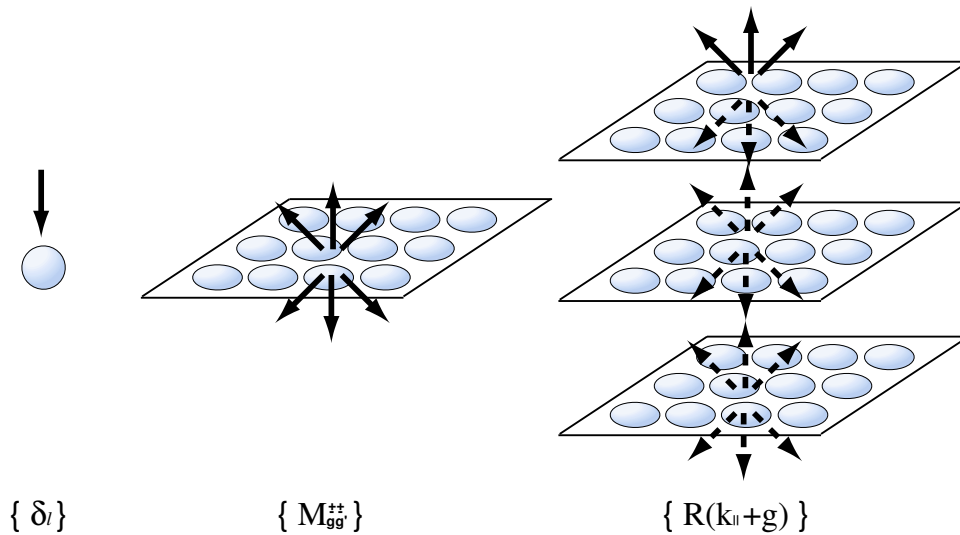


Fig. 3.2: Hierarchy of dynamical LEED intensity evaluation. [95].

3.2 Dynamic LEED Theory

Standard Dynamic Intensity Calculation. As mentioned above, dynamic LEED theory is necessary for the determination of atomic structures. The computation of diffraction intensities must consider multiple scattering due to the large cross section for electron-atom scattering. Though the total of scattering events is complex the calculations can be organized in a clear way by following the hierarchical scheme as displayed in Fig. 3.2: First, the scattering of the electrons by a single atom is calculated. Then the atoms are arranged to form an atomic layer for which layer diffraction matrices are computed. Finally, the layers are stacked to a crystal to yield the total reflection matrix of the surface.

The single atom scattering results from solving the Schrödinger equation assuming an atomic potential of spherical symmetry and finite spatial extension. The radius of the sphere is usually defined so that neighboring spheres touch each other. Electron orbitals extending over the sphere are redistributed inside the sphere. In the area between atomic spheres the potential is kept constant described by the real part of the inner potential V_{0r} . It adds to the electron energy when the electron enters the solid, so its total kinetic energy within the surface is $E_i = E + V_{0r}$. For an atomic layer the potential looks like an arrangement of a muffin tin, from which the expression muffin-tin potential arises. Of course, the spherical symmetry of the atomic scattering potential is an approximation only, as the atom is embedded in an arrangement of non-spherical symmetry. However, this approximation works well for LEED energies, because they are so much above the Fermi energy that scattering is dominated by the spherically symmetric inner electron shells and the nucleus of the atom. Due to the spherical symmetry the scattering is best described in the angular momentum

presentation resulting in a set of phaseshifts δ_l with l cut off at a certain maximum value l_{max} . For higher values of l the phaseshifts are assumed to be negligible, thus

$$l_{max} \approx kR \quad (3.17)$$

with R the radius of the atomic sphere is usually a good approximation. By solving the Schrödinger equation, the phaseshifts fully describe the multiple scattering within the atom.

The scattering within an atomic layer is also described in the angular momentum presentation. Scattered spherical waves outgoing from a certain atom are expanded to spherical waves with respect to the atomic position of a neighboring atom in order to account for multiple scattering. As this neighbor may scatter back to the original atom a self-consistent solution of the total sum of the scattering processes is required. This is equivalent to the inversion of a matrix whose dimension scales with l_{max}^2 . Calculation and inversion of this matrix usually requires the major part of the computing time. For the total diffraction from a layer of atoms a representation in momentum space is appropriate because of translational symmetry. Therefore, the sum over all dynamical atomic scattering amplitudes is developed in a set of plane waves with surface parallel momenta $(k_{i\parallel} + \vec{g})$ producing layer diffraction amplitudes $M_{gg'}^{\pm\pm}$ where the \pm signs indicate the direction of incoming and outgoing plane waves. Eventually, the matrices $M_{gg'}^{\pm\pm}$ are used to stack the layers in order to produce the full surface diffraction. Multiple diffraction between layers has to be accounted for, which again leads to the inversion of a matrix. It is sufficient, to couple neighboring layers step by step so that by each matrix inversion the number of layers can be doubled (layer doubling scheme). The dimension of the matrix is determined by the number of propagating plane waves, for which a natural cut-off is the Ewald sphere, so that $|\vec{g}| < k$ results. However, as attenuated waves also couple between neighboring layers, more beams have to be considered. When the layer spacings are well above about 1 Å one can avoid the matrix inversion and profit from the fact that forward diffraction of a layer (described by $M_{gg'}^{++}$ or $M_{gg'}^{--}$) normally dominates over back diffraction (described by $M_{gg'}^{+-}$ or $M_{gg'}^{-+}$). The corresponding approximative procedure is known as Renormalized Forward Scattering (RFS) [96].

While travelling within a solid an electron undergoes inelastic processes dominated by plasmon excitation by which it disappears from the elastic channel. This can be described by the imaginary part of the inner potential, the so called optical potential V_{0i} , which is of the order of 4-5 eV at 100 eV and is slightly energy dependent ($V_{0i} \propto E^{1/3}$ is usually a good approximation [97]). So, the total inner potential is complex

$$V_0 = V_{0r} + iV_{0i} \quad (3.18)$$

This with

$$\frac{1}{2}k^2 = E + V_0 \quad (3.19)$$

results in an imaginary part of the wavenumber,

$$k_i \approx V_{0i}/k_r \quad (3.20)$$

with

$$k_r \approx (2E + 2V_{0r})^{1/2} \quad (3.21)$$

for $V_{0i} \ll (E + V_{0r})$. Consequently, spherical and plane waves described by $\exp(ikr)$ and $\exp(i\vec{k} \cdot \vec{r})$, respectively, are attenuated whilst travelling. Quasielastic scattering by phonons also removes electrons from the coherent elastic channel. This can be described by a Debye-Waller factor, which reduces the atomic scattering factor for a finite temperature to

$$t(E, T) = t(E, 0) \exp\left(-\frac{1}{2} \Delta k^2 \langle u^2 \rangle\right) \quad (3.22)$$

with Δk the modulus of the electron's momentum transfer and

$$\langle (u(T))^2 \rangle = \langle u^2 \rangle \quad (3.23)$$

the mean square atomic displacement due to atomic vibrations at temperature T . The simple relation between t and δ_l

$$t(E, T) = (k)^{-1} \sum_l (2l + 1) \sin \delta_l \exp(i\delta_l) P_l(\cos \vartheta) \quad (3.24)$$

with ϑ the scattering angle, allows simulation of the Debye-Waller factor by complex phaseshifts $\delta_l(T)$. This is a simple way to consider thermal vibrations also for multiple scattering processes, although this description is not fully exact.

Reliability Factor. In order to measure the agreement between curves quantitatively, so called reliability factors (R -factors) are widely used today. Due to the complex structure of the spectra, different concepts for the construction have been followed in the past leading to a variety of different R -factors [88]. Today, the relative mean square deviations of intensities (R_2) or the Pendry R -factor (R_P) are mostly used. In both cases the summation is over all intensities $I_g(E_i)$ taken for different beams g and at different energies E_i . So R_2 simply results by

$$R_2 = \sum_{i,g} (cI_{cal} - I_{exp})^2 / \sum_{i,g} (I_{exp})^2 \quad (3.25)$$

where c is the average normalization constant between experimental and calculated spectra. The Pendry R -factor [98] is more sophisticated and follows the idea that maxima and minima in the spectra are the important features. Their positions come by constructive or destructive interference, which depends both on the electron wavelength and the pathlength difference between different interfering diffraction processes. Therefore, emphasis is on the positions of maxima and minima rather than on the

absolute height of intensities. So, instead of the intensities their logarithmic derivative with respect to energy is used

$$L = (\partial I / \partial E) / I \quad (3.26)$$

As for small intensities this is very sensitive to experimental errors, the bounded function

$$Y = L / [1 + (LV_{0i})^2] \quad (3.27)$$

is used instead of L . The Pendry R -factor then simply results as the mean square deviations of Y functions rather than of the intensities as in the case of R_2 . i.e.

$$R_P = \sum_{i,g} (Y_{cal} - Y_{exp})^2 / \sum_{i,g} (Y_{cal}^2 + Y_{exp}^2) \quad (3.28)$$

Ideal agreement corresponds to $R_P = 0$, uncorrelated spectra yield $R_P = 1$ and anticorrelated curves produce $R_P = 2$. The variance of the Pendry R -factor

$$var(R_P) = R_{P,min} (8V_{0i} / \Delta E)^{1/2} \quad (3.29)$$

with ΔE the energy width of the total data base, allows estimation of the error limits for the model parameters determined [98].

Tensor LEED Approximation. As described above the theory of dynamical low energy electron diffraction has been well developed since the 1970s. It allows the reliable calculation of intensities for structures in principle of any complexity. However, though for clean and low index surfaces the calculation can even be performed on a minicomputer, the necessary computer efforts grow considerably with increasing complexity. They scale, depending on the approximations used, with $n^2 - n^3$ where n is the number of atoms in the unit cell. Though the calculations could be speeded up by the use of symmetry adapted functions in angular momentum expansion [99, 100] this remained fatal for the retrieval of the correct values of structural parameters when a scan of the parameter space is used to find the best theory-experiment fit in a trial-and-error procedure. This is because the number of trial structures grows exponentially with the dimensionality of the parameter space, i.e. the complexity of the structure.

Therefore, the strategy to solve complex structures by LEED must be twofold. On one hand the computer efforts to calculate the intensities for a certain structure have to be reduced. On the other hand, the scan of the parameter space has to be given up in favor of directed search procedures or direct methods. In fact, both strategies were followed during the last decade. The substantial reduction of computer time for the intensity calculation was made possible by the introduction of the perturbation method tensor LEED.

Of course, any reduction of computer time for the calculation of intensities of a trial structure must use certain approximations instead of applying the full dynamical theory. In the latter approximations are also used, which, however, can be iterated

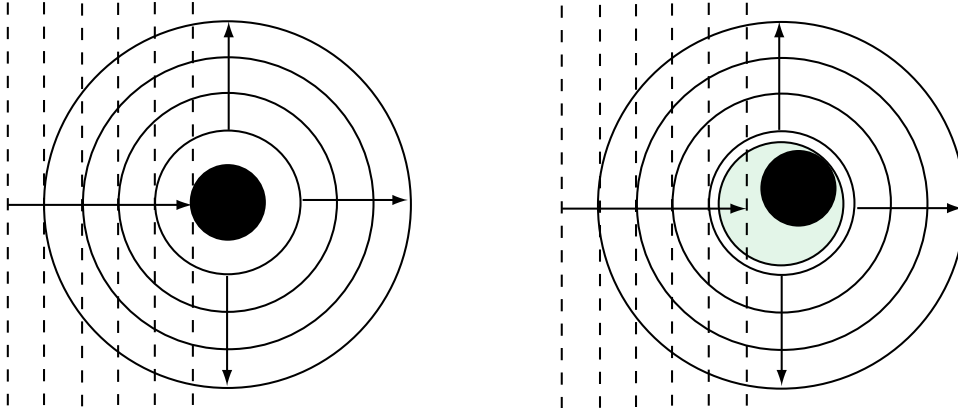


Fig. 3.3: Scattering of a plane wave by an atom into a spherical wave centered at the atom's origin (left) and by a displaced atom (right) with the scattering expressed in terms of spherical waves centered at the original position. [102].

to yield accuracy. Such approximations have been tried since the early days of LEED calculations [88]. All of them consider only a subset of the total of the multiple scattering processes, which is, of course, at the cost of accuracy. Nevertheless, these approximate schemes proved to be useful in a number of cases. However, they were made largely superfluous with the development of the powerful tensor LEED method. The underlying theory was developed by the London Imperial College group. It marks the most important progress in LEED theory made during the 1980s [91,101]. Its essentials are presented below.

Assume that a full dynamical calculation has been carried out for a certain structure, i.e. a reference structure, and that the electron wave field $|\Psi(k_{\parallel})\rangle$ inside the surface has resulted according to an incident electron beam with surface parallel momentum k_{\parallel} . Now some atoms at positions \vec{r}_j with scattering t -matrix t_j are displaced by $\delta\vec{r}_j$ to form a certain trial structure. If the atomic scattering of the displaced atom is still to be described by a t -matrix t'_j located at its former position \vec{r}_j one has to modify the old matrix according to

$$t'_j = t_j + \delta t_j(\delta\vec{r}_j) \quad (3.30)$$

the new matrix t'_j can no longer be diagonal because, as illustrated in Fig. 3.3, the displacement introduces a non-spherical distortion of the scattering potential. In angular momentum basis using the abbreviation $L = (l, m)$ the change of the matrix can be calculated by

$$\delta t_{jLL'} = \sum_{L''} G_{LL''}(\delta\vec{r}_j) t_{L''} G_{L''L'}(-\delta\vec{r}_j) - t_{jl} \delta_{ll'} \quad (3.31)$$

whereby G represents the spherical wave propagator, which converts a spherical wave centered at \vec{r}_j to a set of spherical waves centered at $\vec{r}_j + \delta\vec{r}_j$. The atomic displacements

cause a change of the diffraction amplitude, which for the final direction with parallel momentum $k_{f\parallel}$ can be calculated by first order perturbation

$$\delta A = \sum_j \langle \Psi(k_{f\parallel}) | \delta t_j | \Psi(k_{\parallel}) \rangle \quad (3.32)$$

In angular representation this can be expressed by

$$\delta A = \sum_j \sum_{LL'} T_{jLL'} \delta t_{jLL'} \quad (3.33)$$

which eventually allows the calculation of the intensity of the new trial structure by

$$I = |A_0 + \delta A|^2 \quad (3.34)$$

with $I_0 = |A_0|^2$ the intensity of the reference structure. The quantity T is a tensor in angular momentum representation and this explains the name tensor LEED or, more precisely, as geometrical displacements cause the t -matrix changes, geometrical tensor LEED. The tensor depends only on the reference structure and this mirrors the main advantage of the method: Once the tensor has been computed the intensity of any trial structure results very quickly using equations (3.31)-(3.34). This is similar to a kinematic description of diffraction: in equation (3.33) the tensor represents the form factor and the δt stand for the structure factor. In fact, scattering processes involving more than one δt , i.e. multiple scattering at changes of potentials, are neglected in tensor LEED. In other words, the change of scattering due to the atomic displacements is calculated kinematically.

Limitations of tensor LEED must exist with respect to the amount of $\delta \vec{r}_j$, by which atoms can be displaced. Unfortunately, because of the complexity of multiple scattering, no strict rules can be derived, though tensor LEED is exact in the kinematic limit of diffraction. Experience tells that for displacements up to 0.2-0.5 Å tensor LEED works well. This limit and the accuracy reached depend largely on the extent of multiple scattering correlations of displaced atoms. In turn, this depends on the scattering strengths of the atoms, the number of atoms displaced, the direction of displacement and the electron energy. Consequently, tensor LEED retrieve the correct structural data if the corresponding atomic displacements are not too large.

We have the impression that displacements of up to only a few tenths of an Angstrom are not very helpful to scan a substantial part of the parameter space. In fact it is true, that a good initial guess, i.e. the reference structure chosen being near the true structure, is always of great advantage. If the perturbation of a chosen reference fails to produce a satisfying fit to the experiment, one must try a new model and start a new reference calculation. This procedure is advisable anyway, in order to avoid landing in a local minimum of the R -factor and is applied in demanding structure determinations.

Once the reference structure calculation has been carried out, tensor LEED is extremely fast to compute the intensities for neighboring structures. If there are n atoms per unit cell, the CPU time to calculate any new structure simply scales with n , rather than with $n^2 - n^3$ in the full dynamical procedure. If only a small number of structures has to be calculated the overhead burden to perform the reference calculation might favor the full dynamical calculation. However, as soon as a large number of trial structures has to be checked, as is usually the case, dependent on the complexity of the structure tensor LEED is faster by orders of magnitude [103].

Automatic Structure Search. After the measurement the calculation of intensity spectra for a certain model is only the second step of the structural analysis. A task of substantial difficulty is still left, namely to find the correct model. This always starts with finding a reasonable model on the basis of some pre-knowledge about the surface under consideration. So, one generally knows the crystallographic face and the elemental composition of the substrate. In most cases the latter is also known for the adsorbate or it can be deduced from independent Auger measurements and/or from thermal desorption spectroscopy. Vibrational loss spectroscopy can be used to provide information about the orientation and bonding of molecules, and images obtained by the tunnelling microscope may even suggest a single atomic model or rule out models, which would be possible in principle. Last, but not least, experience from structure determination of related surface systems can be of great help, too.

Once a reasonable and promising model is established, the parameters of this model need to be adjusted. There are several ways for this procedure, which are based on a trial-and-error procedure, whereby scanning the parameter space is the most basic procedure. When a large number of parameters on a dense grid has to be scanned, the necessary computational efforts grow dramatically and an automated search to find the best fit structure is needed, i.e. a numerical procedure, which by built-in criteria finds the minimum of the R -factor automatically by a directed search. A number of such procedures were developed in recent years differing in requirements, strategies and efficiency, where experience from x-ray crystallography was very helpful [89]. Requirements can differ by the need to use derivatives of the R -factor with respect to parameters rather than only the intensities themselves. Derivatives in most cases are calculated numerically and so suffer from experimental noise and approximations used for the calculation of intensities [102]. Strategies differ by the numerical method to find the R -factor minimum and by the type of R -factor used.

The use of automated search procedures was frequently proposed [88] but first realized by the York group applying a form of steepest descent [105]. Starting with a certain reference structure the behavior of the R -factor in the surrounding part of the parameter space is explored to find the direction in which the R -factor decreases most and this procedure is iterated. Soon after, and in parallel, different other groups developed procedures of their own. The Munich and Berlin groups [106] use a non-

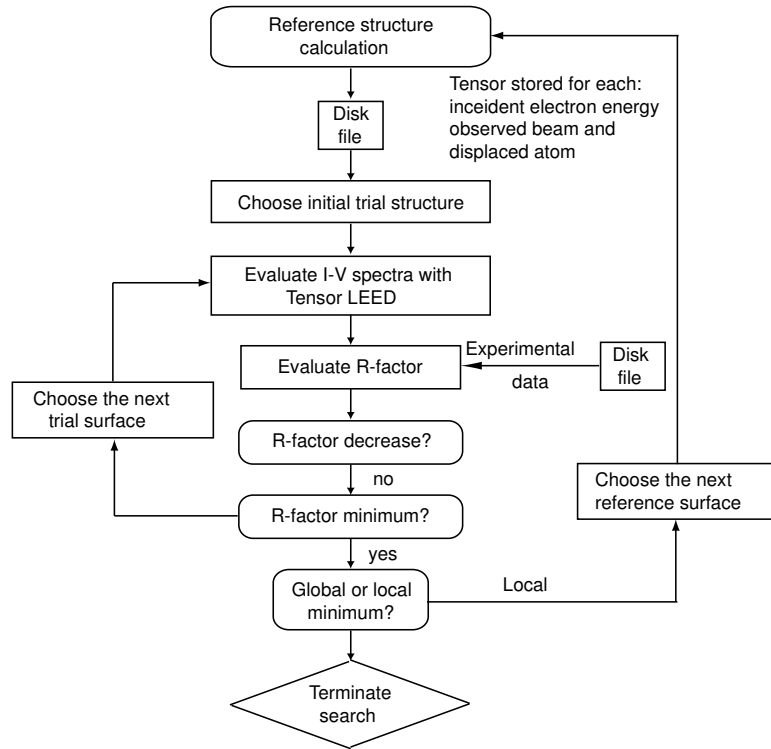


Fig. 3.4: Flowchart for the R -factor optimization using tensor LEED [104].

linear least-squares fit procedure whereby the expansion method is combined with the method of steepest descent [107].

Though the number of trial structures is dramatically reduced with the automated search mentioned above, there is a clear drawback. When the parameters are varied systematically in a grid search, one can make multiple use of costly energy-dependent quantities, such as, e.g., layer diffraction amplitudes, before this quantity is calculated for the next energy. This advantage has to be given up in the automated search because for a new set of parameters the data at all energies are needed for the comparison to experiment and for the decision, where to move next in parameter space. A way out of this situation is the use of tensor LEED together with a directed search as was accomplished by the Berkeley group [89, 104] and is displayed by the flowchart given in Fig. 3.4. For a certain reference structure, which is chosen in a promising area of the parameter space, the tensor is calculated and stored for each energy and beam needed as well as for each atom to be displaced from the reference position. The intensities for a trial structure are calculated and compared to experiment by the Pendry R -factor. A steepest descent method is used to reach the next trial structure point in parameter space. For this the Rosenbrook algorithm is used, which does without derivatives. The procedure described is iterated until an R -factor minimum is reached. If on the way to the minimum the validity range of tensor LEED is left, a new reference calculation becomes necessary. Also, as the minimum eventually found

need not to be the global minimum, it is recommended to repeat the entire search procedure starting with different reference structures well separated in parameter space. The deepest minimum found is believed to correspond to the correct model as long as the R -factor level reached is satisfactory.

One can never be sure, that the best fit model found corresponds to the global best fit. This is an intrinsic feature, because there is no mathematical criterion, whether a minimum is local or global. Even with a grid search one can land in a local minimum, if the span of the parameter space chosen was too small. Efforts to get around this problem, e.g., by application of a simulated annealing procedure [108], which allows large random jumps in parameter space, have only started. It should be emphasized, that none of the automated search procedures described or in sight is push-button safe. In spite of their high degree of automation, they need the investigator's experience with respect to the selection of the parameter space and proper starting points as well as to the critical judgment of intermediate and final results.

Chapter 4

Experimental

4.1 Experimental Equipment

4.1.1 UHV System A

The sample preparation and measurement of LEED spot-profiles were performed in an Ultra High Vacuum (UHV) chamber with a SPA-LEED system, a room temperature STM system and some additional facilities (ion sputtering gun and sample heating) for sample preparation.

The chamber is pumped by a turbo molecular pump TPU 510 (Balzers), which was connected to a rotary pump 10 BHV (Leybold). In addition, a Ti sublimation pump ST 22 (Vacuum Generator) and an ion pump IZ 270 (Leybold) were installed. The base pressure in the chamber was below 1×10^{-10} mbar. A Bayard-Alpert ionization gauge (hot cathode) was used to permanently supervise the pressure of the chamber. The composition of the background gas in the chamber was analyzed using a quadrupole mass spectrometer.

For sample preparation, the following components were used in the UHV chamber.

Sample Cleaning. An Ar^+ ion sputtering gun IQE 11/35 (Specs) was used in the chamber with kinetic energies up to 5 keV and an emission current of approximately 10 mA. Typical emission currents between 3 to 10 μA were chosen in practice with the kinetic energies in the range from 600 eV to 1 keV.

Sample Heating. The sample was heated indirectly by a W-filament, kept in a distance of approximately 2 mm from the backside of the sample. 2.8 A filament current corresponds to a temperature of 320 °C. More than 1000 °C can be achieved, when increasing the filament current.

Co Evaporator. The Co evaporator is a self-made conventional Knudsen cell (K-cell) with an Al_2O_3 crucible used for evaporating the Co [109].

Gas Inlet System. The gas inlet system used for the oxygen, which is needed to prepare oxide films, was evacuated by a separate smaller, air-cooled turbopump TPU 062 (Balzers).

4.1.2 SPA-LEED System

The SPA-LEED system is a commercial Omicron optics, similar to the one Henzler *et al.* developed in 1986 [110].

Principal Elements. Fig. 4.1 shows the principal elements of the SPA-LEED system. The system has a glass phosphor screen, which is observed from the back side. The screen gives a quickly available overview of the reflex pattern. Due to the large distance between the crystal and the screen the spatial resolution is higher than with a normal optics, so that more details can be recognized. On the other hand, the visible area of the reflex pattern is smaller. Behind holes in the screen the electron gun and the channeltron are mounted. In the main mode the intensity at a given position of the pattern is detected by the channeltron. Using two sets of electrostatic deflection plates the whole diffraction pattern is scanned over the channeltron aperture. A crystal lens focuses the electron source with an imaging ratio of 1 : 1 onto the channeltron aperture of 0.1 mm diameter.

Electrostatic Deflection. The main concept of the system is to handle the reflex scanning with electrostatic deflection. No mechanical movement of the sample or of the detector is needed during scanning, which would reduce accuracy and speed considerably. Without voltages applied, the direct beam is reflected into the channeltron aperture for a crystal with its surface inclined by 4° relative to the axis of the system. The mechanical construction determines the angle between the incoming beam \vec{k}_i and the outgoing beam \vec{k}_f . For electrostatic scanning the opposite deflection plates are supplied with equal voltages of contrary polarity. The ratio of voltages between the screen plates and the crystal plates is chosen close to -1 so that the position of the primary beam does not shift on the crystal. The angle between \vec{k}_i and \vec{k}_f remains constant during scanning. Therefore, the absolute value of the scattering vector $\vec{K} = |\vec{k}_i - \vec{k}_f|$ stays constant, only its orientation with respect to the surface varies during scanning. Therefore, a modified Ewald-construction with the center of the sphere at 000 as shown in Fig. 4.2 for the Si(111) surface has to be used. Here, the scattering vector \vec{K} is the radius of the sphere instead of the incidental vector \vec{k}_i , in the usual Ewald-construction. Due to the doubled radius the scanning range in reciprocal space is doubled for a given energy and a given deflection angle of the beam.

Electron Gun. The electron gun supplies an emission current up to 10^{-6} A for the screen display although a fraction of it would be sufficient. If working with the channeltron a current of 10^{-10} to 5×10^{-8} A is needed. For that low current the electron source diameter is less than 0.1 mm down to an electron energy of about 30 eV. The electron gun uses a commercial directly heated tungsten filament with a tip. For that small diameter special efforts are needed with adjustment and design of cathode, Wehnelt cylinder and anode region.

Data Acquisition and Control of the Experiment. Voltages may be applied

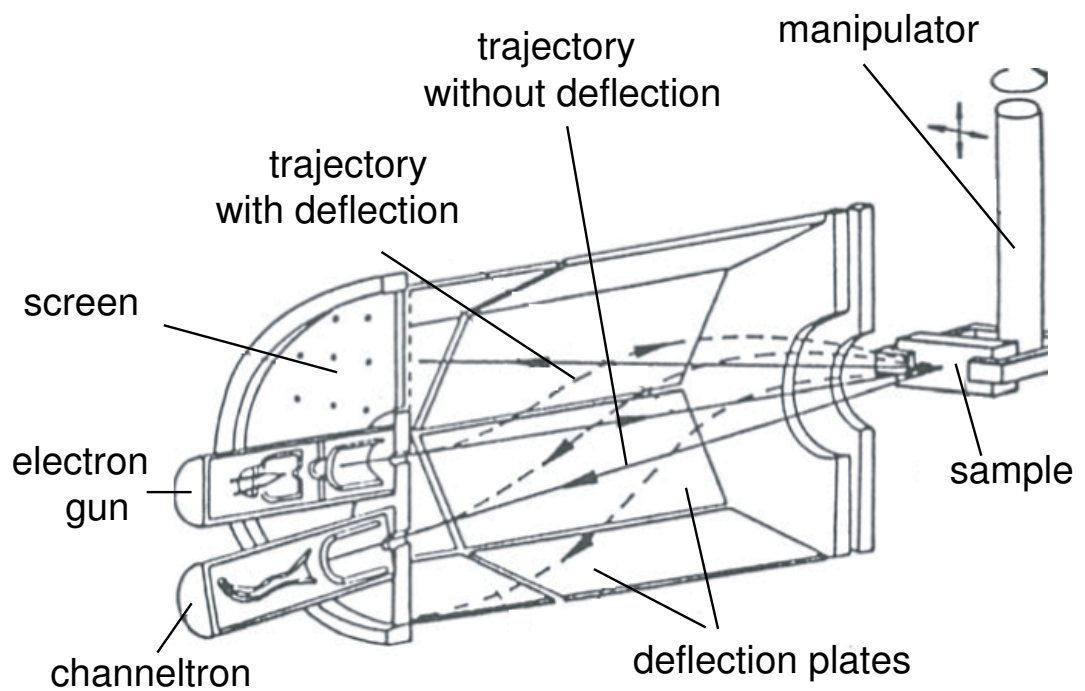


Fig. 4.1: . Schematic set-up of the SPA-LEED system.

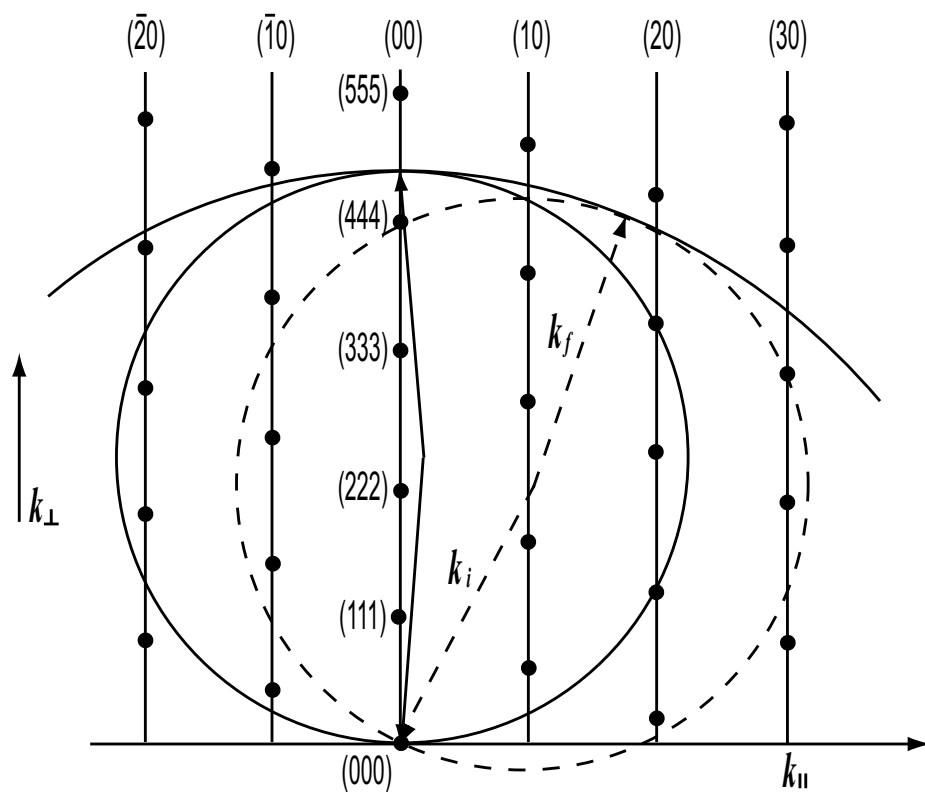


Fig. 4.2: . Scattering geometry for the SPA-LEED instrument, the angle between the wave vectors \vec{k}_i and \vec{k}_f remains constant at 4° ; the situation is equivalent to a sample rotation with fixed positions of the detector and the source. [90]

to the deflection plates under computer control. At a fixed primary electron energy the count rate of every scan position is recorded. The computer generates one dimensional line scans or two dimensional area scans. In the case of area scans the intensity can be presented as contour levels or a surface plot with different magnifications. Dependent on the scale the area scan gives either an overview of the whole Brillouin zone or detailed information of one or a few spots only. Mainly for area scans the aspect of measurement time becomes important. The total measurement time depends on the total number of channels and for each channel on the desired accuracy. With a number of 10^4 channels an area of 100×100 points may be recorded. Linear scans of at least 1000 channels are used for accurate measurements throughout the Brillouin zone to enable reliable quantitative evaluation.

With this instrument the transfer width was increased up to 100 nm, i.e. periodic structures with a separation up to this length can be resolved. Due to channeltron detection, the intensity can be measured over a range of six orders of magnitude. An important information which can be directly extracted from the spot profile is the average terrace length of a atomically rough surface. In this case, the important quantity is the Full Width at Half Maximum (FWHM) measured at an "out-of-phase" scattering condition. Under the assumption that coherent scattering between different terraces is negligible, the half width yields the average terrace width $\Gamma = 2\pi/\Delta k_{\parallel}$.

4.1.3 UHV System B

The LEED $I - V$ measurement for the structure determination part of this work were performed in another commercial multi-functional UHV system (Omicron Full Lab) shown in Fig. 4.3.

The system consists of a preparation chamber, an analysis chamber and a fast entry lock for sample transfer. The analysis chamber is equipped with an electron analyzer, a partial yield electron detector, a Mg/Al dual anode X-ray gun, a rare gas UV lamp, an electron gun, a reverse view LEED system and a combined AFM/STM set-up. This enables investigations with following methods: Photoemission Spectroscopy with UV or X-ray excitation (UPS, XPS), Auger Electron Spectroscopy (AES), Scanning (Auger) Electron Microscopy (SEM, SAM), Low Energy Electron Diffraction (LEED), Atomic Force Microscopy (AFM) and Scanning Tunneling Microscopy (STM). The preparation chamber is equipped with an ion sputtering gun for sample cleaning and a quadrupole mass spectrometer for the analysis of processing gases and the residual gas in the chamber. The sample can be heated by radiative or electron bombardment heating of the sample plate. The temperature of the sample is measured using an optical pyrometer. Base pressures in both chambers are below 5×10^{-11} hPa. XPS investigations were performed using Al $K\alpha$ excitation. The reverse view LEED system can be expanded to a video LEED system, which is essential for the present work and will be described in more detail in the following section.

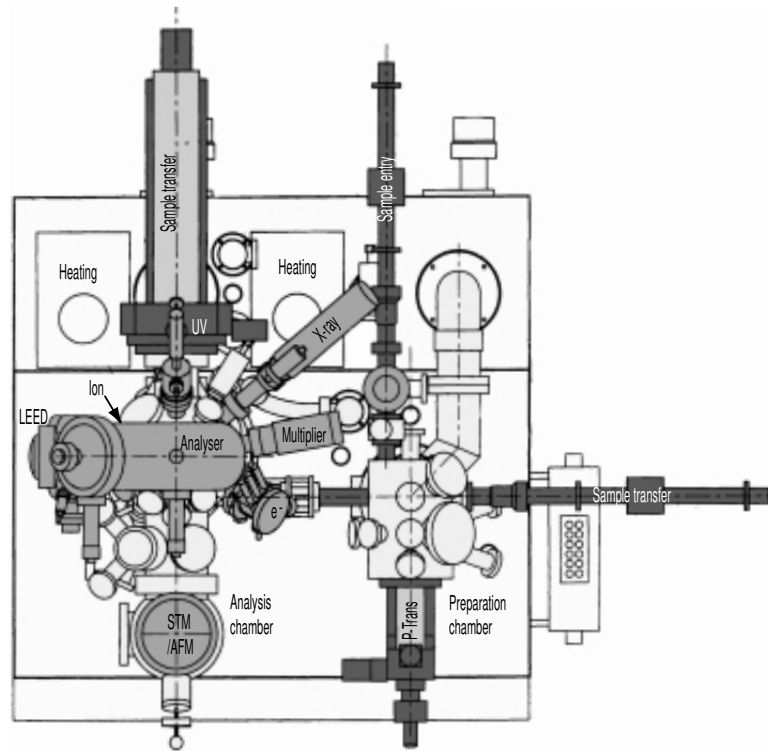


Fig. 4.3: . Multi-functional UHV system (Omicron Full Lab), top view.

4.1.4 LEED $I - V$ Measurement System

The LEED Optics. The setup of the LEED experiment consists of three main components: an electron gun, a sample holder for the single crystal, and a detector. Usually the detector is a luminescent screen, which together with the electron gun forms a commercially available set, called the "LEED optics". This is shown schematically in the right part of Fig. 4.4. The electrons are thermally emitted from a cathode of low work function, e.g. a LaB_6 source, and are accelerated by a variable voltage according to the energy desired. A system of electrostatic lenses within the gun forms an almost parallel beam and directs it onto the sample. Electrons are both elastically and inelastically scattered back from the surface, whereby they are allowed to propagate in a field-free space between the sample and a transparent metallic grid. Before entering a detector the elastically scattered (i.e. diffracted) electrons have to be separated from all others. This "energy analysis" is realized by a retarding field applied by means of additional hemispherical grids. Usually the last grid is followed by a fluorescent screen, on which the diffracted electrons are postaccelerated by a voltage of several kilovolts. According to the direction of the beams a LEED pattern of bright spots appears on the screen. If the luminescent screen is made of glass it can be viewed from behind (reverse view optics).

Video Based Data Acquisition. The direct way for the measurement of in-

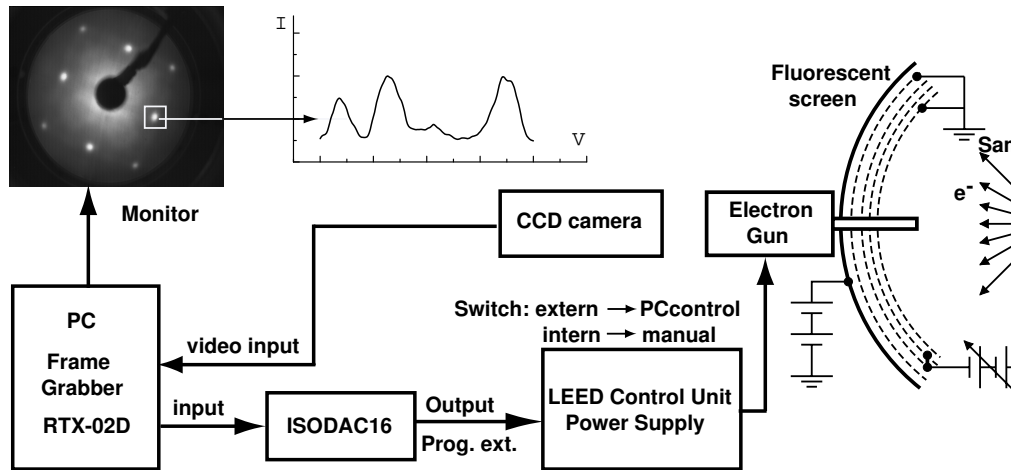


Fig. 4.4: Schematic diagram of video LEED system for LEED $I - V$ spectra measurement.

tensities would be to measure the beam currents by a Faraday cup. However, with varying energy the diffraction angles change enforcing the delicate handling of a cup movable in UHV. For this reason nowadays access to intensities is indirectly and from outside the UHV equipment, namely by the measurement of the light the diffraction beams create on the luminescent screen. Originally, spot photometers were used, but today they are almost exclusively replaced by video cameras as final detectors. Various modifications of this technique have been used to date since the first implementation of the method. They can differ by the speed of the camera, the speed of digitization and/or the evaluation method of the digitized data. Here we concentrate on one of the commercially available version, which was used in the present work in the following.

In Fig. 4.4 the way the system works is shown schematically: The LEED pattern is viewed by a CCD video camera from outside the LEED chamber. By this way the data acquisition system is independent from the restrictions put by the UHV apparatus and, even more, the camera can be moved to any equipment wanted. The video signal is digitized by an 8 bit converter using a frame grabber card (Video 1000 S/W) with a selectable resolution for the full video frame. The digitized intensities are stored in computer memory. If only data within a certain area of the screen are of interest, this area can be preselected by the corresponding setting of an electronic window, which is displayed on the monitor for visual inspection and control. Up to eight such areas can be chosen in parallel under program control using a PC. The areas are of rectangular shape and the digitized intensities inside can be transferred to the PC memory. Further data processing like summing up the intensities to yield the integrated intensity within the window, background correction or averaging over

several windows in order to improve the signal/noise ratio can be carried out under software control. The digitized intensities and the result of data processing are displayed on-line on the PC monitor. In addition, the video signal can be saved in the PC for storage and/or later off-line evaluation. Besides the video signal, a voltage proportional to the primary electron beam current is digitized by an A/D converter and stored separately for later use, in particular for proper normalization of the measured intensities. For the measurement of $I - V$ spectra the control of electron energy is important. This is realized by a computer generated voltage, which drives the power supply of the electron gun via a 16 bit D/A converter (ISODAC16) and a digital I/O interface (RTX-02D). All functions of the video system are controlled by mouse or keyboard driven menus.

$I - V$ Spectra Measurement. In order to determine the position of atoms within the surface unit cell, i.e. the surface structure, the integrated intensities of spots have to be measured and evaluated. The precision of the structure determination depends on the quality and width of the data. The latter increases with the number of beams and the energy range measured. With the sweeping of the energy both the positions and intensities of the spots change. Therefore, any measurement technique has to track the spot moving with energy and simultaneously integrate the intensity over the spot's extension. Additionally, background intensities superimposed on the spot have to be subtracted. The whole procedure should be fast in order to avoid the influence of residual gas adsorption or sample damage by the electron beam.

The video technique perfectly meets all these requirements. Under software control an electronic window is set to frame the spot wanted. The intensity of the pixels digitized within the window are added up under simultaneous determination of the maximum position as well as of the background level at the window's edges. The integrated intensity is corrected for the background level and the result is stored into the PC's memory. Then the energy is stepped forward (typically by 1.0 eV), the window is centrad around the spot maximum and the procedure described is repeated. So the $I - V$ spectra develop step by step until the preselected energy range is covered. If the spot intensity decreases below a certain minimum, so that the intensity maximum cannot be determined, the position of the window is extrapolated from the track recorded so far. The whole procedure proceeds in real-time. In order to improve the signal/noise ratio the intensities can be multiply measured at each energy and subsequently averaged. This increases the total time of measurement correspondingly.

4.2 Sample Preparation

4.2.1 Ag(100) Substrate

Sample Orientation and Polishing. The Ag crystal with a misorientation smaller than 0.5° was checked by the Laue-method. First, the sample was mechanically polished by Al_2O_3 , which reduces the granulation of the sample from $1\ \mu\text{m}$ at the beginning to $0.05\ \mu\text{m}$ finally. Afterwards, the crystal was chemically polished outside the UHV chamber in an Argon-Hydrogen-mixture (95% Ar, 5% H_2) at $700\ \text{^\circ C}$, in order to eliminate the mechanical strains, which have been introduced during the polishing process.

Further Treatment before Transfer into the UHV Chamber. The Ag single crystal is fixed on a tantalum sample holder very carefully in order to avoid mechanical strain. Small tantalum leaf springs press from the top gently on the edge of the sample.

Since Ag reacts very sensitively to the wrong choice or contaminated solvent, the sample and the sample holder were washed with 2-Propanol ($\text{C}_3\text{H}_8\text{O}$) prior to the transfer into the UHV chamber. 2-Propanol (besides ethanol) was also be used for cleaning all other vacuum components in this work. The commonly used acetone (also used for leak detection) must not be used, because the lifetime of the LaB_6 cathode of the SPA-LEED system is drastically reduced by contact with acetone.

Preparation under UHV Conditions. After transfer into the UHV chamber, the sample was sputtered with Ar^+ at first without any annealing, otherwise possibly existing impurities generated during the polishing and assembling process will form dislocations. If heating the sample, the movement of these dislocations will be stimulated. They can spread to the whole crystal and lead to the formation of steps on the surface. Under certain circumstances, the surface becomes too disordered for surface physical measurement and must be polished again.

The preparation of Ag substrates in UHV has been described in Ref. [111,112]. Typical steps of preparation are sputtering by 600 eV Ar^+ with a partial pressure of 1×10^{-6} mbar followed by annealing at temperatures between $300\ \text{^\circ C}$ and $350\ \text{^\circ C}$.

Sputtering and Annealing. About three atoms will be removed by every impinging Ar^+ in the sputtering process ([113], p65). Teichert *et al.* [111] have found that with 600 eV Ar^+ , an Ar partial pressure of about 8×10^{-5} torr and an ion current of $2.4\ \mu\text{A}/\text{cm}^2$ at 300 K, the erosion rate is about 2.2 ML/min. In the present experiment, the erosion rate should not differ significantly from this value, since the selected sputtering parameters were very similar.

Initially, the surface was sputtered with 600 eV Ar^+ (Ar partial pressure: 1×10^{-6} mbar, in the ionization area of the sputtering gun approximately 1×10^{-4} mbar) at 300 K in each preparation cycle. For newly transferred sample, the sputtering time was about 60 min each time. After several preparation cycles the sample surface was clean

and no impurities could be detected by STM measurements. At this stage, a shorter sputtering time (about 15 min each time) is enough, even after vapor deposition experiments.

In further attempts, the sample was successively sputtered at higher temperatures (about 500 K), whereby the yield per impinged ion will increase. By annealing at 600 K, the sample again shows a smooth surface. The optimal sputtering conditions can be found from the recent work by Costantini *et al.* [114]. They showed that the Ag(100) surface will be removed in a layer by layer way during sputtering at a temperature above 440 K. The sample was always sputtered at 300 K followed by annealing within several minutes. Thus, diffusion of the vapor deposited material into the bulk of the Ag single crystal could be avoided.

Other authors chose 550 °C [115] or 480 °C [31] as sputtering temperatures. However, sputtering at high temperatures causes unwanted diffusion of impurities from the bulk to the surface. Furthermore, the heating of the Ta sample holder and the other environment in the UHV chamber was considered as sources of unexpected adsorbates. An additional problem is the different expansion coefficients of Ag and Ta. After high temperature annealing and cooling, the sample is no longer fixed firmly to the mounting plate, which makes the analysis by means of STM and SPA-LEED impossible. Such problems arise frequently (for example) with Si and Ru since the necessary preparation temperatures are 1250 °C [116] and 1330 °C [117], respectively. Therefore, it is advantageous, if short annealing times at low temperatures can be chosen.

4.2.2 CoO Films

For the preparation of CoO films, we used the same approach as Marre and Neddermeyer, who evaporated Ni onto an Ag(100) surface in an O₂ atmosphere [31]. Before deposition, the Ag(100) substrate temperature is either increased to the desired temperature or kept at room temperature (300 K). Simultaneously, the Co evaporator is heated to the necessary evaporation temperature, which was about 1300 °C. If these two temperatures are stable, the desired O₂ partial pressure (purity: 99.998%) in the UHV chamber is adjusted. Then the substrate surface is moved into the Co steam jet and left there. The time of the sample in the beam gives the desired deposition quantity. An experiment is generally terminated by moving away the sample from the Co steam jet, stopping the O₂ supply, switching off the heating, and cooling the sample at 300 K for up to 30 min.

The calibration of the evaporator was performed during the evaporation of Co on Ag(100). The 0.2 ML/min Co deposition rate was determined from the STM image. Repeated calibrations showed good reproducibility of the deposition rate. The temperature of the evaporator is determined by a WRe3-WRe25 thermocouple [109]. The required temperature of 1300 °C for evaporation corresponds to a thermovoltage

of 23.5 mV. It took about 8 min to stabilize the thermovoltage, after which the evaporating experiment can be started.

4.2.3 BaTiO₃(111) Surface

The BaTiO₃ crystal with a (111) surface (Crystec GmbH, Berlin) was clamped onto a tantalum sample plate using tungsten strips. Liang and Bonell [118] have reported on a systematic change of the composition of the surface layer with annealing. It has also been described in the literature that annealing the samples in UHV produces a surface with O deficiency [119]. In the present experiments, we have therefore attempted to follow the influence of various surface treatments in more detail. Different preparation procedures were applied in order to obtain clean and ordered surfaces. The initial procedure consisted of sputtering with Ar⁺ (1 keV, 10 min, 2 μA cm²) and annealing by heating up to 1470 K. It turned out that sputtering of the samples with Ar⁺ produced large height variations on the surfaces. In accordance, the LEED spots became broader. Obviously, annealing was not able to restore surface order after sputtering. Therefore, the surface treatment was restricted to annealing in vacuum or O atmosphere (10⁻⁶ and 10⁻⁴ mbar) without sputtering. This treatment normally leads to clean surfaces, where surface contaminations by C or other impurities (except for Ca, which was sometimes seen as local precipitate) could not be detected by AES and XPS. Taking into account the corresponding cross-sections, the intensity ratios of the emission lines in XPS are in sufficient agreement with a stoichiometry of BaTiO₃. The Ti 2*p* and Ba 3*d* emission lines exhibit shoulders on the lower and higher binding energy side, respectively. Corresponding shoulders on the (100) surface have previously been assigned to Ti³⁺ centers [120] and to a surface core level shift [121].

The sample was vacuum annealed at 1470 K for 20 minutes, then cooled down to room temperature. The temperature of the sample is measured using an optical pyrometer. The BaTiO₃(111) ($\sqrt{3} \times \sqrt{3}$)R30° reconstruction was obtained after several cycles of annealing and cooling. LEED spots indicated the formation of long range order as concluded from their sharpness.

Chapter 5

SPA-LEED Analysis of CoO on Ag(100)

One main interest of surface physics is to analyze structural defects of surfaces and films (atomic steps, inhomogeneities, grain boundaries, anti-phase domains, non-crystalline areas, randomly displaced atoms, etc.), because they may drastically influence physical and chemical processes occurring at surfaces. In the meantime, there are many experimental techniques available to study surface defects on an atomic scale. For this purpose, microscopic (STM, AFM, SEM, TEM) and diffraction techniques (electron, X-ray and atomic beam diffraction) are well established complementary techniques. Microscopy provides a lot of information about details of defects. Diffraction techniques, on the other hand, are better suited if one is more interested in obtaining statistical information about the distribution of defects, because structural defects strongly influence spot profiles (depending on the scattering condition).

Up to now the spot profile analysis is only possible within the kinematic approximation, where the dynamic scattering process is divided into an average form factor describing the multiple scattering of the electrons at several surface atoms and a lattice factor governed by the arrangement of the surface atoms. It has been demonstrated by a huge number of investigations, that this kinematic approximation mostly holds for LEED, if one confines oneself to the spot profile analysis.

5.1 Characterization of the Ag(100) Surface

The exact knowledge of the substrate is an elementary condition for understanding the growth of thin films on the substrate. Therefore, large effort has been given to the characterization of the Ag(100) substrate. Two different Ag single crystals sample have been used in our experiment, one crystal was relatively badly oriented with a misorientation $> 0.5^\circ$, in addition its surface was insufficiently polished. Another crystal shows high quality with a misorientation of less than 0.5° .

5.1.1 Instrument Response Function

At first, LEED patterns and one dimensional spot profiles measured from the high quality sample will be shown, because spot profiles measured from this surface give the

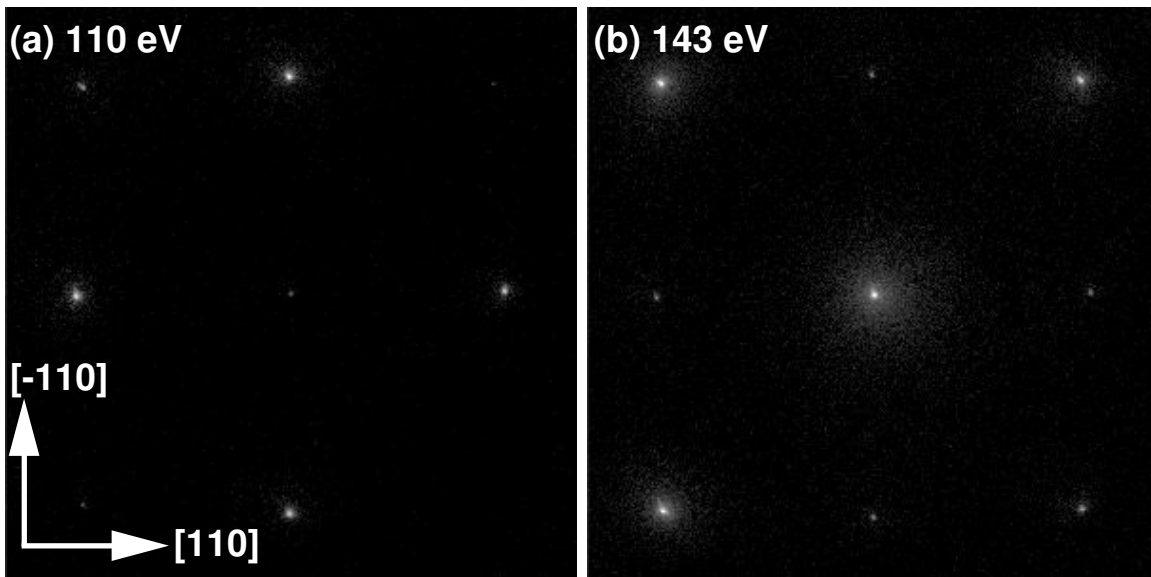


Fig. 5.1: LEED patterns (in a logarithmic intensity scale) of the high quality Ag(100) surface after sputtering at room temperature and annealing at 500 K, Energy: (a) 110 eV. (b) 143 eV.

instrument response function of the SPA-LEED system. The corresponding transfer width, defined as the Full Width at Half Maximum (FWHM) of the Fourier transform of the instrument response function, can be evaluated. In a quantitative spot profile analysis, the instrument response function must be deconvoluted from the measured profile.

Before the measurement, the Ag(100) surface was prepared by several sputtering and annealing cycles. STM measurements show the surface covered by large smooth terraces, with terrace widths between 500 Å and 1500 Å. LEED patterns were recorded for several different energies. Two typical LEED patterns are shown in Fig. 5.1a, b. These patterns are displayed with a logarithmic intensity scale. The LEED spots are very sharp at both energies.

Spot profiles along the $\langle 110 \rangle$ direction through the (00) spot were recorded for different values of the vertical scattering phase $S = K_{\perp} d / 2\pi$, where d is the interlayer spacing. In the case of Ag(100) $d = 2.045$ Å, K_{\perp} is the component of the electron wave vector perpendicular to the surface. Integer values of S correspond to constructive interference of waves diffracted from adjacent terraces ("in-phase" condition), while half-integer values of S correspond to destructive interference ("out-of-phase" condition), so that a maximum sensitivity to surface defects such as the steps is achieved. In the following, the parallel scattering vector K_{\parallel} will be expressed in percent units of the first Brillouin zone (% Bz) along the $\langle 110 \rangle$ direction.

Fig. 5.2 shows two spot profiles of the (00) spot recorded at the "in-phase" ($S = 5.0$) and the "out-of-phase" condition ($S = 4.5$), both profiles are very narrow and

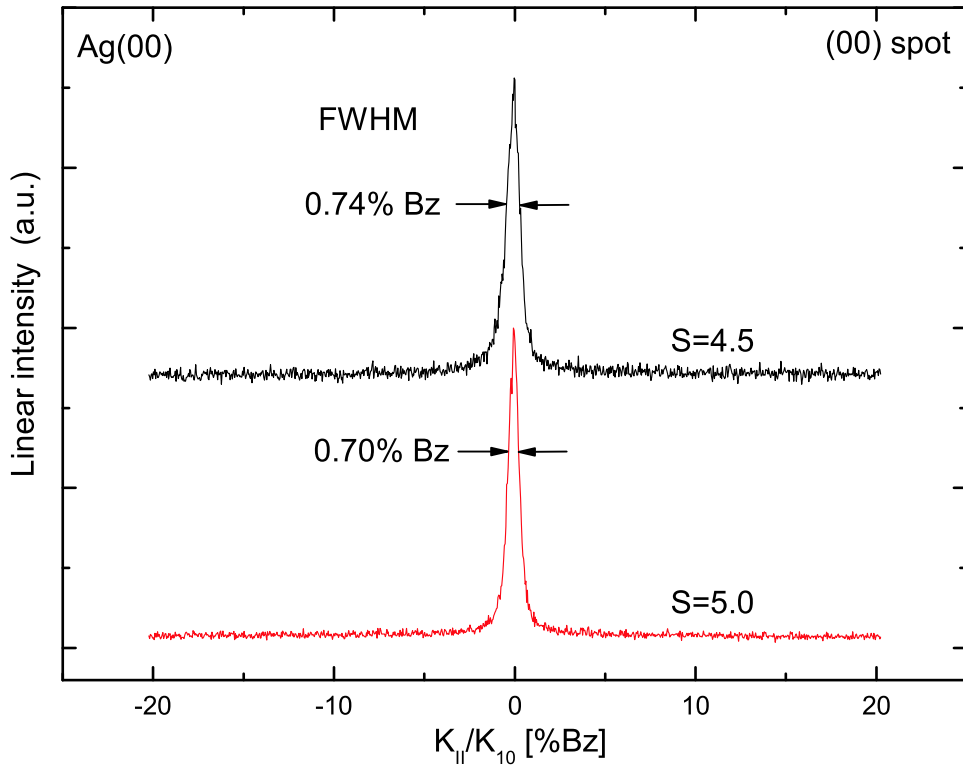


Fig. 5.2: (00) spot profiles (in a linear intensity scale) recorded along $\langle 110 \rangle$ direction, at the "in-phase" condition ($S = 5.0$) and the "out-of-phase" condition ($S = 4.5$)

can be fitted well by Gaussian functions with a FWHM of about 0.70% Bz for the "in-phase" condition and 0.74% Bz for the "out-of-phase" condition. The FWHM of profiles measured at other scattering conditions are nearly the same (See Fig. 5.7) and no broadening induced by steps can be detected. The effective transfer width of the instrument is estimated to be larger than 410 Å.

5.1.2 Defects on the Ag(100) Surface

Surface defects strongly influence LEED. Atomic steps on regularly or randomly stepped surfaces are the most intensively studied surface defects. The influence of regularly arranged steps on the LEED pattern has been discussed since the 70ths by Park and Farnsworth [122]. The first thorough LEED analysis is given by Schwoebel *et al.* [123]. Here, some results obtained for surface steps will be recalled. The LEED pattern observed from a surface covered with steps of a single orientation, regular spacing and height shows some integral order spots split into doublets. With changing voltage all spots appear alternately as doublets and single spots. The characteristic voltages, at which single spots or doublets (at equal brightness) appear, may be calculated from the step height and are independent of both orientation and terrace width. These voltages differ from spot to spot. The spacing of the doublets depends

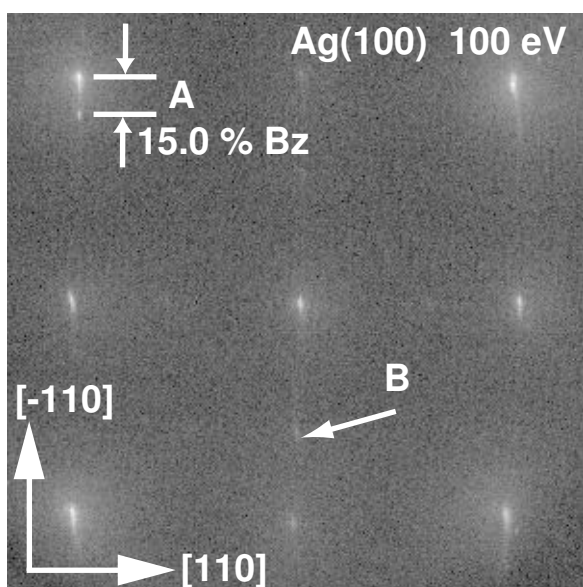


Fig. 5.3: LEED pattern (in a logarithmic intensity scale) recorded from the relatively poor quality Ag(100) surface. It shows different defect features (see text), $E=100$ eV ($S=3.4$).

on the terrace width and the doublets direction is perpendicular to the step direction. The equation for the calculation of the characteristic voltages has been derived. The voltages of the (00) spot are independent of bulk structure and crystallographic face. For random distributed terraces all LEED spots vary their width periodically between a sharp and a diffuse appearance with increasing electron energy. A broadening caused by random distributed steps is easily distinguished from other defects like irregular superstructure domains or lattice distortions due to the characteristic oscillations with energy, which is only possible for step structures.

A typical LEED pattern recorded from the relatively poor quality sample is displayed in Fig. 5.3. It shows very prominent parallel streaks along the [-110] direction, additional spot splitting (A) present near these streaks as well as satellites along the $\langle 110 \rangle$ direction (B). The streaks change their shape with energy and at some energies they become sharp. The satellite spots are very weak. It is difficult to see them in the two dimensional pattern, hence are not detectable with a conventional LEED instrument, but they are clearly resolved in the one dimensional spot profiles, as shown in Fig. 5.4.

As already mentioned, the streaks in Fig. 5.3 are caused by random distributed terraces, while the spot splitting (A) is due to regular arranged step arrays. The observed characteristic spot splitting is about 15.0% Bz, which corresponds to a width of about 18 Å (6-7 atomic distances).

The satellite spot (B) corresponds to a Ag(111) facet on the Ag(100) surface, since its position shifts continuously towards the (00) spot, when the vertical scattering phase is decreased from a noninteger value towards the Bragg condition. This is clearly illustrated in the upper panel of Fig. 5.4, where a set of spot profiles recorded along the $\langle 110 \rangle$ direction through the (00) spot is shown. The lower panel shows the

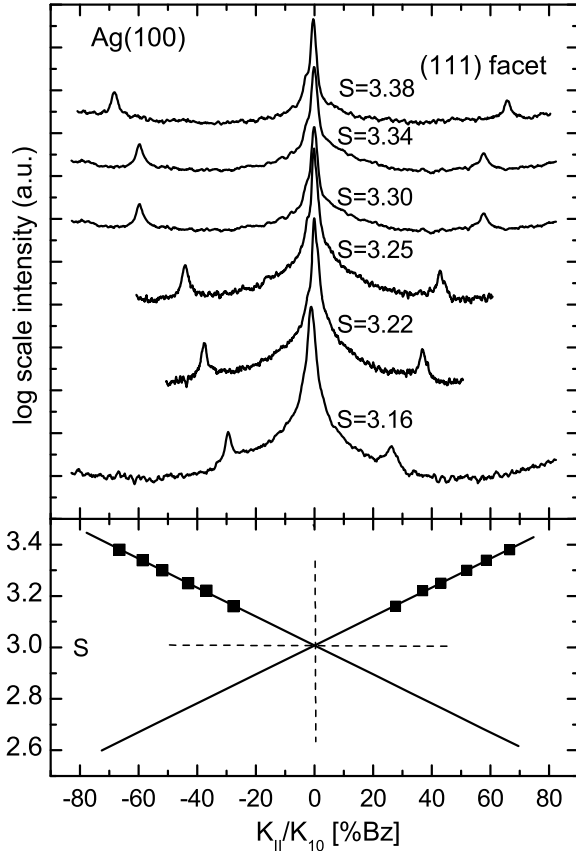


Fig. 5.4: (00) spot profiles obtained for Ag(100) along [110] direction at different vertical phases S (upper panel) and phase-dependent positions of the satellite spots (lower panel).

phase dependent shift of the spot positions in detail. This behavior is characteristic for a periodically faceted surface with a regular up-and-down staircase and has been observed for various systems [90]. The phase dependent spot position shifts that results from such a surface topography are visualized with the help of the Ewald construction: the spot positions are determined by facet rods inclined with respect to the (00) rod.

5.1.3 Ion Sputtered Ag(100) Surface

Spot Shape Analysis. Ion sputtering was used to produce well defined surface step densities. Furthermore, direct imaging methods have revealed that ion sputtering results in the formation of terrace structures with defined step directions, which are essentially determined by the substrate geometry. For example, on noble gas bombarded Au(111) and Pt(111) surfaces triangular and hexagonal vacancy islands were observed by STM, whereas another STM study for 600 eV Ar^+ bombardment of Cu(100) exhibited fourfold terraces mainly bounded by close-packed $\langle 110 \rangle$ step edges.

The LEED spot shape analysis yields information on the lateral extension of coherent scattering regions such as anisotropic periodicity of the unit cell, the shape of

the finite domains or the step arrangement. Fig. 5.5a shows the (00) spot contour recorded at 100 eV (close to the "out-of-phase" condition) from a Ag(100) surface, which has been sputtered with 600 eV Ar⁺ ions at room temperature. Without further annealing, it shows a diamond like shape. Only at the "in-phase" condition, an isotropic spot shape is observed, because the atoms on all terraces separated by surface steps scatter "in-phase", which reflects an apparently "perfect" surface.

As it was already illustrated in the literature, the diamond LEED spot shape on Ag(100) surface is caused by perpendicularly arranged terraces, whose edges are along the $\langle 110 \rangle$ directions. Fig. 5.5b shows a typical STM image measured from the same surface with the pitlike structures. All step edges are forming square pits, all well aligned to the $\langle 110 \rangle$ direction. Monte Carlo (MC) simulations in connection with experimental data revealed the individual atomic processes involved, in analogy to the treatment of epitaxial growth [111].

The step arrangement of an ion sputtered Ag(100) surface is temperature dependent. When Ag(100) surfaces are sputtered by Ar⁺ at low temperature (below about 180 K), the resulting step edges are along the $\langle 100 \rangle$ direction and the corresponding LEED pattern shows a square like shape. The key parameter determining the surface morphology by ion sputtering turns out to be the mobility of adatom clusters and vacancy clusters produced by ion sputtering. Temperature dependent surface morphology models have been proposed for the surface sputtering, in which two reference temperatures are present: an activation temperature for adatom cluster diffusion, $T_{ad} \approx 180$ K, and one for vacancy cluster diffusion, $T_{vac} \approx 250$ K. In particular, for $T_{ad} < T < T_{vac}$ the surface morphology will be dominated by the diffusion and coalescence of adatom clusters (the vacancy ones being practically neglected because of their immobility). For $T > T_{vac}$, the diffusion and coalescence of vacancy clusters will be the dominating process, because the adatom clusters are quickly incorporated at step edges. In this case, pitlike structures like those of Fig. 5.5b ($T = 300$ K) characterize the surface morphology.

Spot Profile Analysis. By analyzing the spot shape we can determine the step orientation on a ion bombarded surface. However, we couldn't get the detailed information about the terrace width distribution, average terrace width, surface lateral and vertical roughness, etc. In SPA-LEED, the spot profile of a crystalline surface contains wealthy information about the size distribution of domains in the surface region, i.e. about the distribution of terrace lengths, step heights, or island sizes. The detailed knowledge of such distribution functions is of great interest for example for the characterization of the surface morphology during epitaxial growth. Parameters as the critical size of a stable nucleus or diffusion constants of the adatoms can be derived from the island size distribution in dependence on the evaporation rate and the substrate temperature. For stepped surfaces step heights and terrace length distributions give information about the interaction between the steps. Systems, for which a detailed knowledge of domain size distributions is particularly useful, are those, which

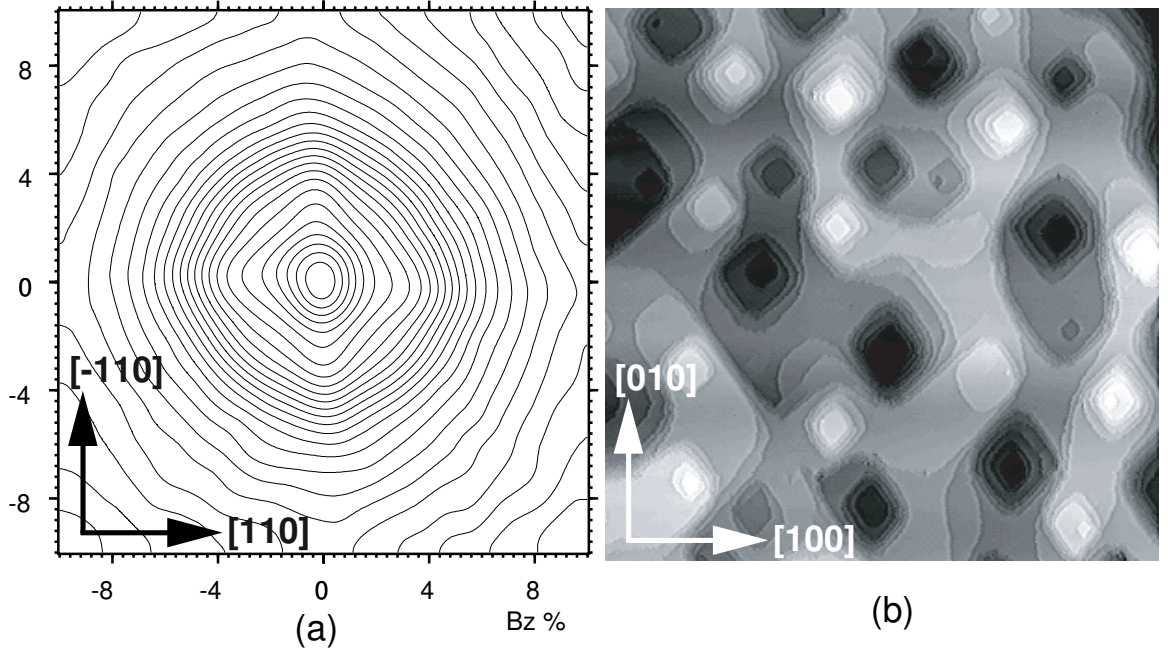


Fig. 5.5: Ag(100) surface sputtering by 600 eV Ar⁺ at 300K. (a): Two dimensional contour plot of the (00) spot close to the "out-of-phase" condition, 100 eV ($S = 3.35$). (b): STM image taken from the same surface shows the pitlike structures ($1500 \times 1500 \text{ \AA}$), The sample bias is -1.0 V and the tunneling current 0.1 nA. note the different sample orientation of two measurements.

form domains in order to reduce surface stress.

Fig. 5.6 shows a spot profile recorded at the "out-of-phase" condition ($S = 5.5$) from the same ion bombarded Ag(100) surface. It has been shown that such a one dimensional spot profile can be described by three contributions. A central spike with only instrumental broadening. An ideally flat surface would produce just that type of spot profile. The second contribution is a shoulder described by a Lorentzian function:

$$1 \propto 1/(1 + a^2 k_{\parallel}^2) \quad (5.1)$$

where k_{\parallel} is the lateral component of the scattering vector and a is determined by the correlation length of the defects. This part of the profile depends on the scattering phase S periodically. Its intensity has always a maximum for half integer values of the scattering phase: $S = 0.5, 1.5, \dots$ ("out-of-phase" condition) and disappears for integer values of S ("in-phase" condition). The third contribution is a constant background caused by point defects and thermal diffuse, inelastic scattering, which is subtracted before further evaluation. The Lorentzian shoulder is explained by a stepped surface, the ratio of the intensity of the central spike and the intensity of this shoulder plus the central spike gives the lattice factor $G(S)$, from which the asperity height and layer distribution are derived. The separation of the three parts of a profile is demonstrated in Fig. 5.6 with the background as dashed line.

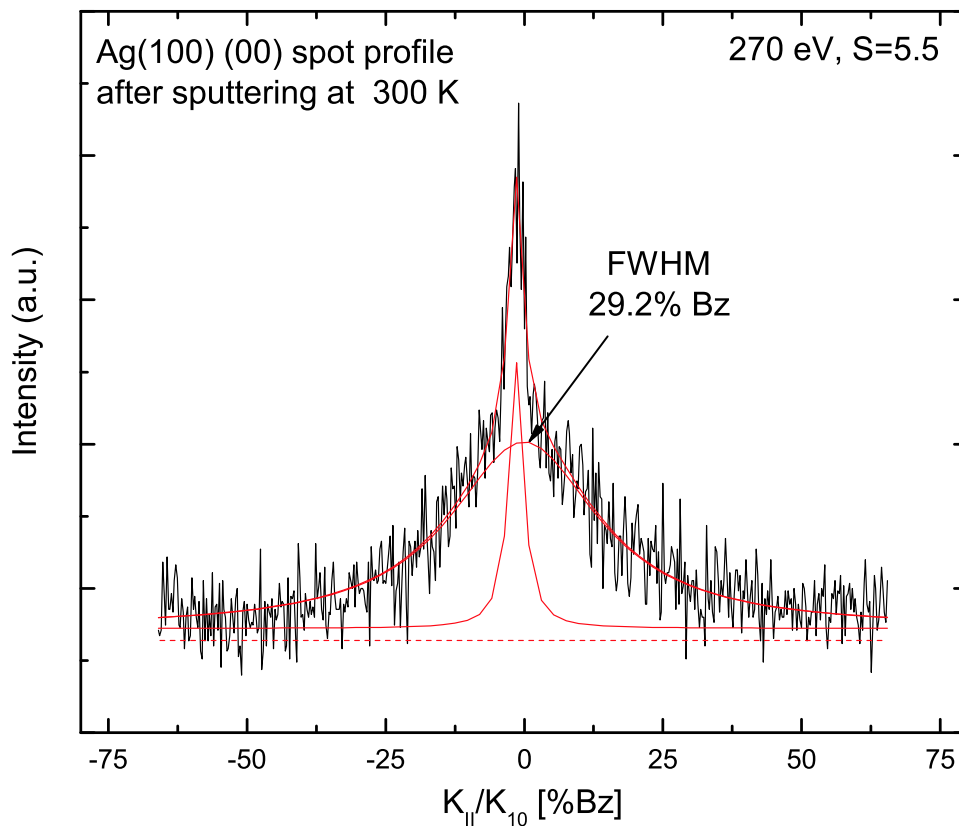


Fig. 5.6: Ag(100) (00) spot profile (in a logarithmic intensity scale) measured at the "out-of-phase" condition, 270 eV $S = 5.0$, the profile can be accounted for by three contribution.

The (00) profile widths are plotted as a function of electron beam energy in Fig. 5.7, along with the corresponding instrument response function for the SPA-LEED system, which represents the width of profiles that would be measured from a perfect surface. As already shown, we have measured the well annealed Ag(100) surface to determine the instrument response function (low curve in Fig. 5.7). Arrows are guides to the eye point and to where the characteristic energies for "in-phase" and "out-of-phase" condition appear. The prominent oscillatory behavior of the dependence of the widths on energy is a clear indication of the presence of atomic steps. Since the form of the oscillations in the fig is roughly sinusoidal, and the FWHM is more or less constant at the "out-of-phase" conditions, we can exclude the presence of a significant amount of multiple steps of height $n \times d$, since these would lead to further minima. The amplitude of modulation of the FWHM with energy is related to the average terrace width, or equivalently, to a step density.

In general, this information is obtained by usual fitting procedures of theoretical spot profiles, calculated for model structures to the experiment data. However, some effort must be made to obtain the terrace width distribution directly from the measured spot profile. In the present situation, a model called geometric distribution has

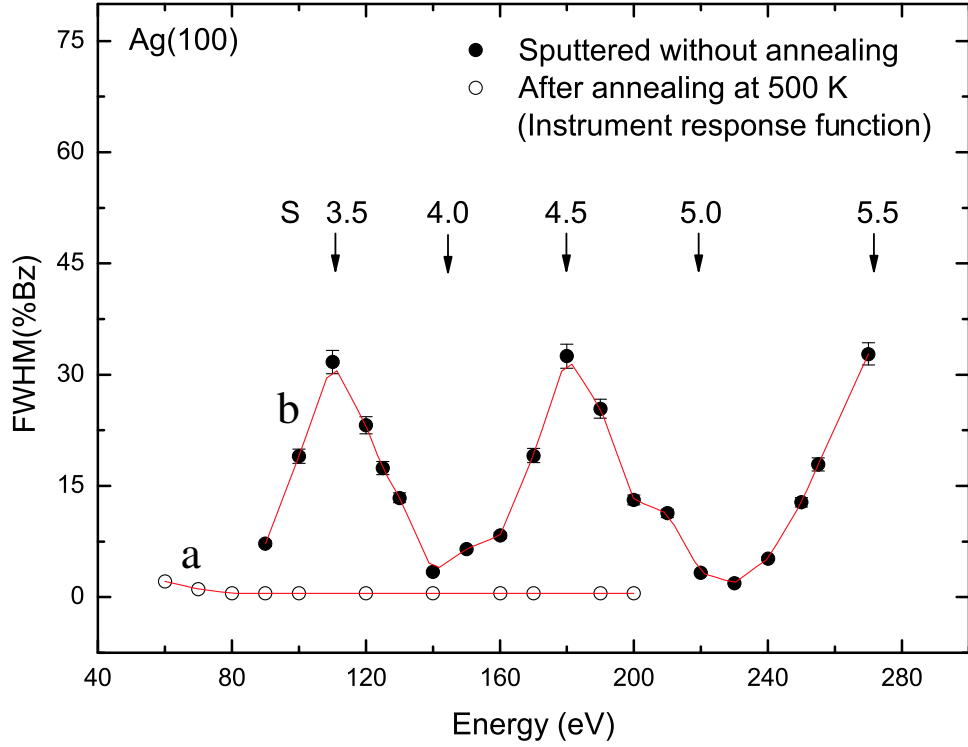


Fig. 5.7: FWHM of (00) spot profiles for Ag(100) surface, the FWHM is plotted versus the beam energy. (a) well annealed after room temperature sputtering (b) after room temperature sputtering without further annealing. The positions of constructive interference ("in-phase") and destructive interference ("out-of-phase") expected for single layer steps are labelled by the index S , the arrows are guide to the eye.

already been developed, which results in a Lorentzian profile. The average terrace width can be calculated from the equation

$$\langle \Gamma \rangle = \frac{2 K_{10}}{\pi K_{1/2}} \quad (5.2)$$

where $K_{1/2}$ is the FWHM of the fitted Lorentzian profile. We obtain an averaged terrace of about 3 ± 1 atoms, which means a very high step density.

5.2 CoO Films on a Ag(100) Surface

In Ref [124], an STM study demonstrated that by reactive deposition Co in an O_2 atmosphere on a hot (450 K-500 K) Ag(100) substrate, CoO films in (100) orientation can be grown. Also it has been mentioned that the overall morphology, the nature of the deposited films and of the substrate drastically depend on the deposition and annealing temperature. For room temperature deposition, an O/metal precursor state is identified, which appears with a height of one atomic layer on top of the substrate as well as within vacancy islands of the substrate, which are generated during the

deposition process. A stoichiometric oxide film can only be obtained at elevated temperatures and grows with a minimum thickness of a double layer. In the initial stage a two dimensional growth of the oxide is found, which changes to a more three dimensional growth mode for thicker films. In the following section we will analyze SPA-LEED experiment data, which have been taken parallel to STM experiments. The result will be discussed and compared with the STM measurements.

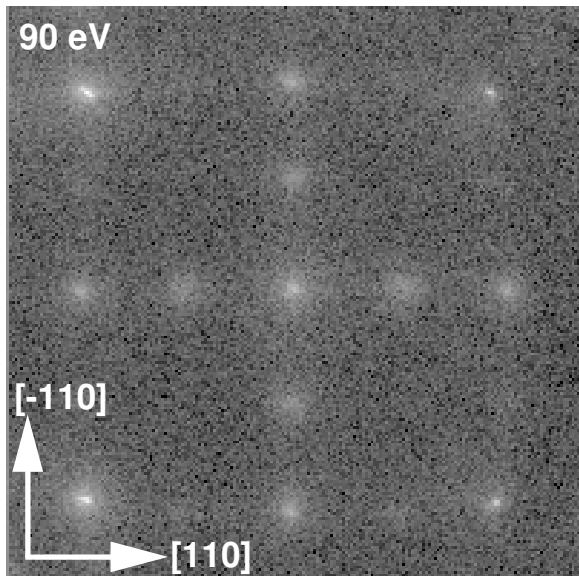


Fig. 5.8: LEED pattern (in a logarithmic intensity scale) of CoO with a (2×1) superstructure after evaporating 2 ML Co on Ag(100) at 300 K and further annealing in an O_2 atmosphere at 470 K.

5.2.1 Growth at 300K

Here, we describe results on oxidic layers deposited at room temperature (RT), which have subsequently been annealed in UHV and in an O_2 atmosphere, respectively. It has already been demonstrated, that only annealing of the films or deposition at elevated temperature gives rise to surface structures, which can be assigned to the formation of the oxide. It has to be mentioned, that RT deposition in the 1 ML range gives rise to large rearrangement effects of the substrate. Four different structures were identified: the Ag substrate, vacancy islands in the substrate surface, Ag islands on the substrate surface and islands of a CoO precursor.

CoO Film of 2ML Thickness. First, we describe results on a 2 ML Co film, which has been deposited on the Ag(100) surface at RT. It has already been shown that without the participation of O_2 , Co forms three-dimensional clusters on the Ag(100) surface. The size of the clusters is between 60 to 70 Å and the height about 15 Å. This result can be explained by the large lattice misfit (13.3%) between Ag and Co (Ag: $a_0=4.085$ Å, Co: $a_0=3.54$ Å).

Annealing the Co film at 470 K in an O_2 atmosphere produces drastic changes of the surface morphology. Square islands are formed with distinct edges along the $\langle 100 \rangle$ direction. Meanwhile, a (2×1) superstructure was found in LEED experiment.

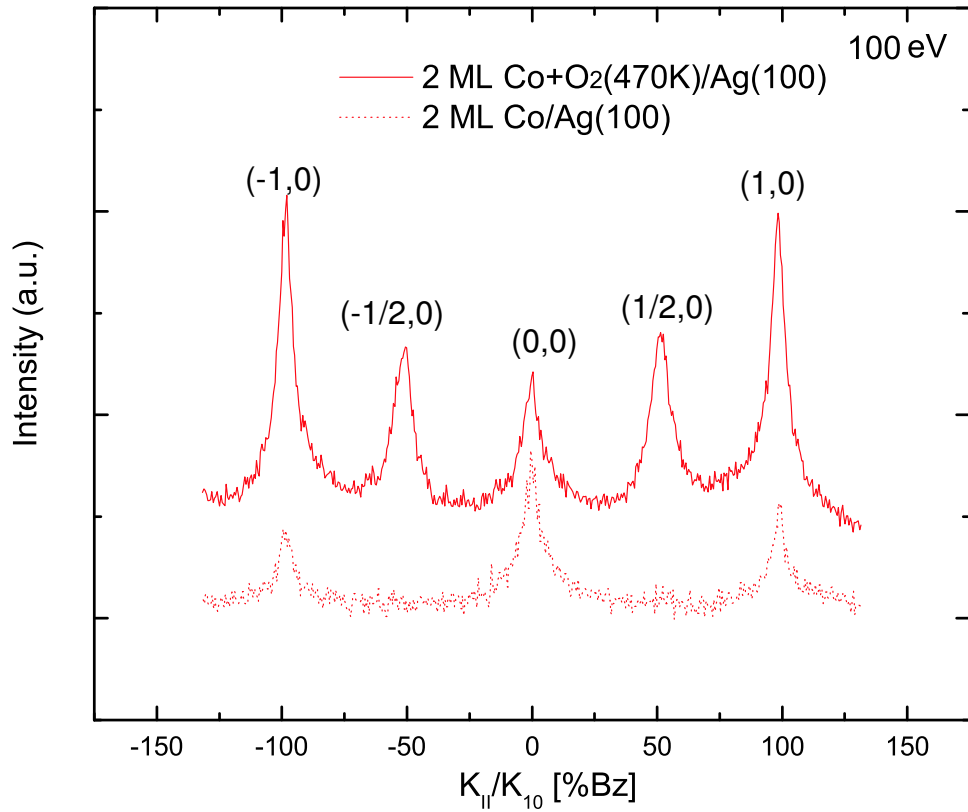


Fig. 5.9: Spot profile (in a logarithmic intensity scale) of 2ML CoO by depositing 2ML Co at 300 K, further annealing in O₂ atmosphere at 470 K. Compare with profiles recorded on bare Ag(100) substrate and pure 2 ML Co on Ag(100).

A typical LEED pattern, which has been taken after annealing, is shown in Fig. 5.8. The appearance of the (2×1) superstructure spots indicate that CoO has already been formed on the Ag substrate. However, the superstructure spots are rather diffuse.

Fig. 5.9 shows the spot profile taken along the $\langle 110 \rangle$ direction at 100 eV, which corresponds to the "out-of-phase" condition for the (00) spot. The (00) peak shows a FWHM of 8.0% Bz, which corresponds to an average island size of 36 Å. The (-10), (10) spots show exactly the same positions as the reference Ag substrate. This means, that the CoO film was pseudomorphic at this stage.

CoO Film of 5ML Thickness. We have already shown that CoO can be formed by annealing the pre-deposited Co film in O₂ atmosphere at high temperature. However, the film is rather rough and no smooth film can be obtained. In the following, CoO films will be prepared by the evaporation Co in an O₂ atmosphere at RT and further annealing in UHV or in an O₂ atmosphere.

At the beginning, 5 ML of Co have been evaporated in an O₂ atmosphere at RT without further annealing. The STM image in Fig. 5.10a shows a rough surface, which is covered by islands with a typical lateral width of 50 Å and a corrugation in the order of 15 Å. The corresponding spot profile is taken at 100 eV and shown in

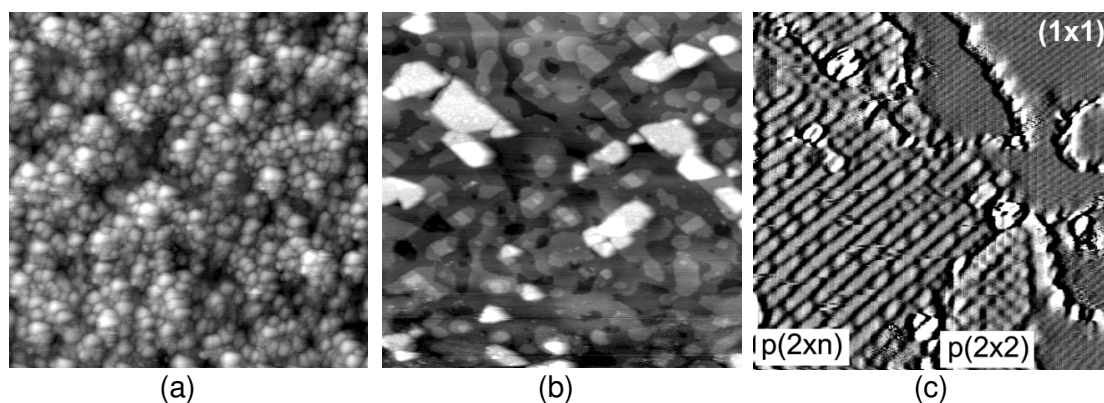


Fig. 5.10: (a) 5 ML Co in an O_2 atmosphere on Ag(100) at RT. $1500 \times 1500 \text{ \AA}^2$. (b) The same sample with additional annealing at 470 K in an O_2 atmosphere for 10 min. $150 \times 150 \text{ \AA}^2$. (c) The same sample after annealing at 470 K for 20 min, the hexagonal CoO islands are identified by the orientation of their edges. $1000 \times 1000 \text{ \AA}^2$.

Fig. 5.11. Again, profiles taken from the Ag(100) substrate and the 5 ML Co film are shown for comparison. The profile shows a (1×1) structure, no superstructure spot are observed. However, the (10) , (-10) peaks are shifted about 2.9% Bz to the center spot compared at the bare Ag substrate. This is a strong indication of a lattice relaxation of the film. The lattice constant of the film calculated to be 4.22 \AA , which is nearly the same value as of bulk CoO.

Annealing the film for 20 min at 470 K produces drastic changes of the morphology, as can be seen in Fig. 5.10b. A considerable smoothing of the film is the main effect. CoO as well as residual metallic Co clusters coexist on the surface. Although the oxide film has been produced under excess of O_2 at room temperature, the Co oxide film grows with a certain O deficiency. This has also been confirmed by Auger electron spectroscopy of similar films. After annealing of such a film, stoichiometric CoO is formed, whereby excess Co condenses and can be observed in form of additional clusters.

We have continued our experiments using the same sample and subsequently anneal it for 10 min at 470 K in an O_2 (10^{-6} mbar) atmosphere. Again, drastic changes of the surface morphology are observed. In Fig. 5.10c an atomically resolved STM image is reproduced. Large parts of the surface show an ordered (1×1) pattern of CoO(100), in other parts, however, $p(2 \times n)$ and $p(2 \times 2)$ superstructures prevail.

It is well known that defects and the stoichiometry of Co oxide surfaces depend strongly on O_2 partial pressure and temperature. The $p(2 \times n)$ superstructures observed after annealing the sample in an O_2 atmosphere at 470 K must be caused by the addition of O_2 during annealing, since they have not been observed after annealing in UHV conditions. By annealing the film in an O_2 atmosphere, the O_2 concentration in the film has certainly increased. Such an increase may give rise to the transformation

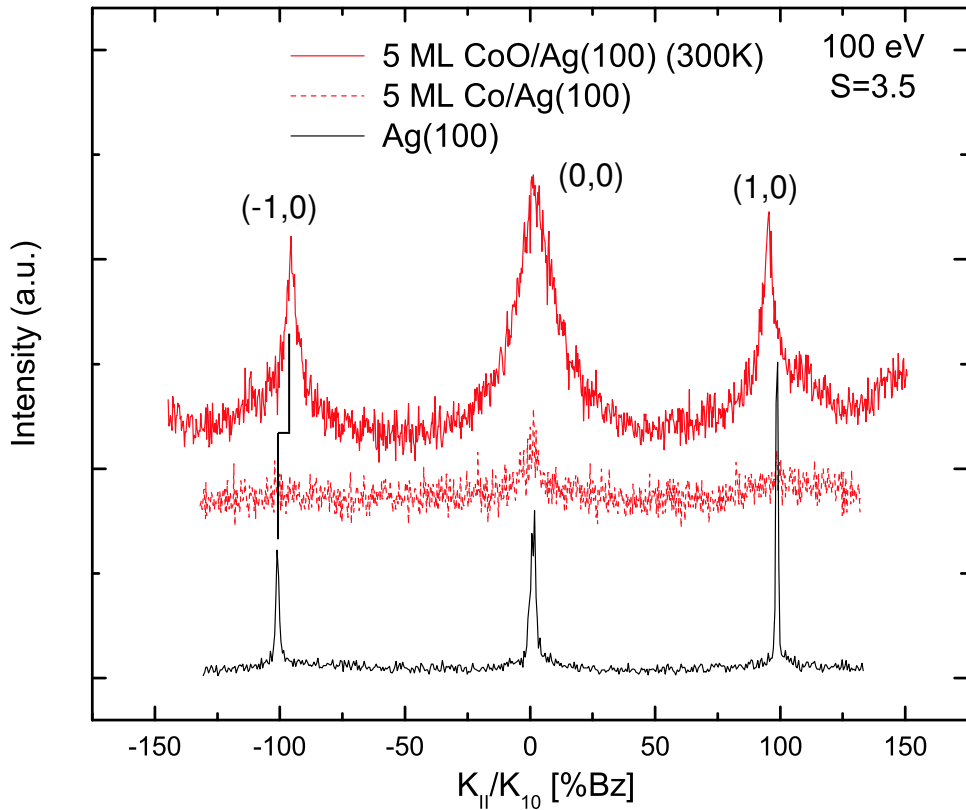


Fig. 5.11: Spot profile (in a logarithmic intensity scale) of 5ML Co deposited in an O_2 atmosphere at 300 K, compared with the bare Ag(100) substrate and a pure 5 Co film on Ag(100). The positions of the (-10), (10) spots of the (1×1) structures still show the same spot positions compared to a Ag surface. $E=100$ eV.

of the CoO(100) to $Co_3O_4(100)$ structure with a correspondingly higher O concentration. The formation of Co_3O_4 layers on CoO(100) at 5×10^{-7} torr O_2 partial pressure and 625 K has been reported [125].

On the same surface, we have recognized islands of hexagonal shape by STM, which might correspond to (111) surface structures of Co_3O_4 or CoO. Whether islands correspond to Co_3O_4 or CoO can't be decided.

CoO Film of 10 ML Thickness. At the beginning, 5 ML of Co have been evaporated in an O_2 atmosphere at RT and spot profiles were taken. The LEED pattern shows that all spots were broadened with weak intensity but without any additional spots. Then, further 5 ML CoO were deposited on the film. The LEED pattern shows even more diffuse spots, but still a four fold (1×1) structure. Finally, the film was annealed for 10 min at 500 K in an O_2 atmosphere ($p(O_2) = 1 \times 10^{-6}$ mbar). Thus, the quality of the CoO film is expected to improve, which was checked by recording the LEED pattern. Surprisingly, the LEED pattern is quite complex as shown in Fig. 5.12a. Besides the expected (1×1) LEED pattern from the CoO(100) structure, ring like spots corresponding to a CoO(111) structure are observed.

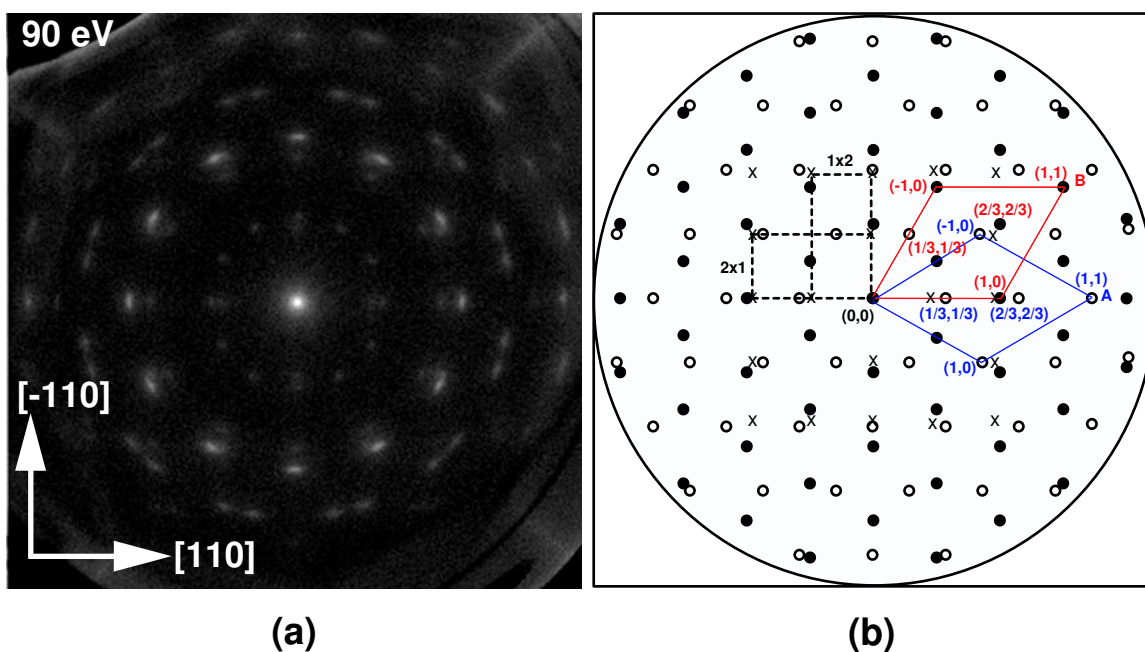


Fig. 5.12: (a) LEED pattern of 10 ML CoO which was deposited in O_2 atmosphere at 300 K with further annealing in O_2 atmosphere at 500 K. Arrows point to the position where the spots come from the (2×1) domains. (b) Model of the LEED pattern on the assumption that two $p(2 \times 1)$ domain rotated each other by 90° and two CoO(111) $(\sqrt{3} \times \sqrt{3})R30^\circ$ domains are present. The filled circles represent the first domain A and open circles the second domain B. The respective unit cell are shown in blue and red color.

The spots corresponding to CoO(111) domains are azimuthally broadened. This broadening corresponds to a rotational misorientation of the CoO(111) domains with respect to the crystallographic orientation of the supporting Ag(100) substrate. This rotational alignment seems to be caused by a better fit of the CoO(111) layer to the underlying Ag(100) substrate. One dimensional azimuthal scans of the first order spots that belong to CoO(111) domains show a FWHM about 10 % Bz. No extra spots or splitting were observed. This indicate that there is no preferential angle, by which the CoO(111) domains are rotated. All rotational angles within a range of 5° are possible, probably due to the different sizes of the CoO(111) domains.

The analysis of the LEED pattern lead to the following structural model: Two CoO(111) domains of a $(\sqrt{3} \times \sqrt{3})R30^\circ$ superstructure, which are rotated to each other by 30° , form the ring like spots. Additional weak spots belong to a (2×1) CoO(100) superstructure. To illustrate this model, a simulated LEED pattern is shown in Fig. 5.12b. It fits quiet well to the experimental LEED pattern. Open circles represent one single CoO(111) domain and closed circles the other. The weak (2×1) superstructure spots are represented by crosses. It is difficult to identify all these simulated spots in the experimental LEED pattern, because some spots are very close to each other. However, through the one dimensional spot profile analysis all weak intensity spots

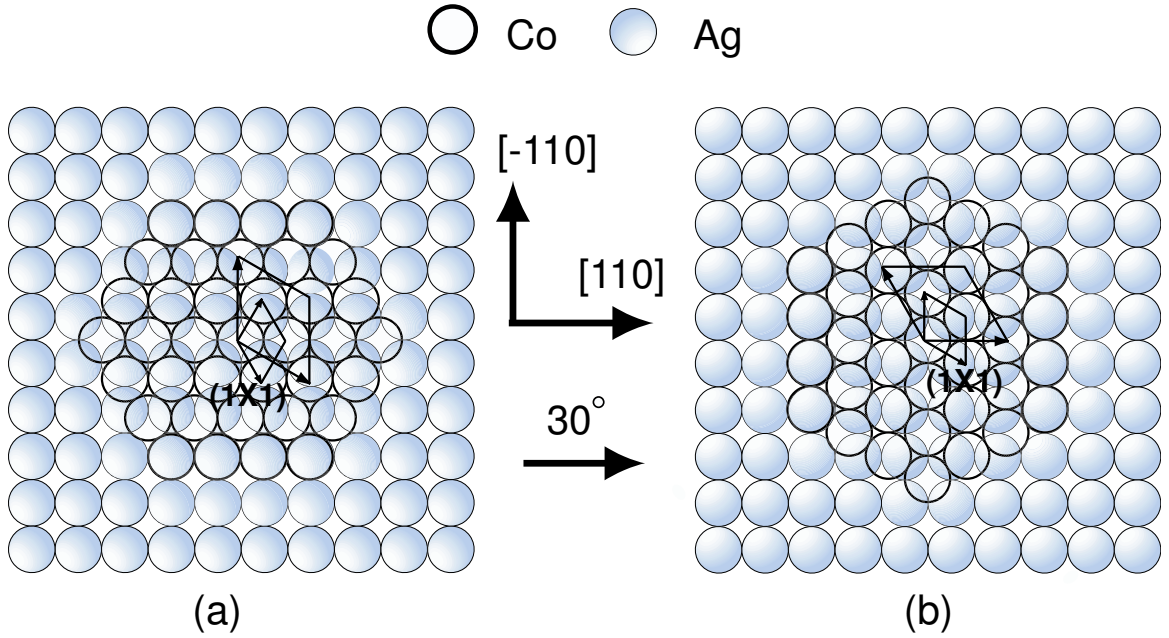


Fig. 5.13: Structure model of 10 ML CoO deposited at RT with further annealing in O_2 atmosphere ($p(O_2) = 1 \times 10^{-6}$ mbar) at 470 K. The $(\sqrt{3} \times \sqrt{3})R30^\circ$ superstructure of CoO(111) on Ag(100). The small unit cell represent the (1×1) structure, the large unit cell represent the $(\sqrt{3} \times \sqrt{3})R30^\circ$ superstructure. (a) Domain A. (b) Domain B rotated by 30° with Domain A.

can be resolved, close spots can be identified and assigned correctly. We will show the one dimensional spot profile later.

Concerning the orientation of the CoO(111) domains in reciprocal space, we found spots coming from the $(\sqrt{3} \times \sqrt{3})R30^\circ$ CoO(111) domains lie along the same direction as the (10), (01) spots of the Ag(100) substrate (see Fig. 5.12a). This relationship indicates that one of the unit vector directions of the $(\sqrt{3} \times \sqrt{3})R30^\circ$ CoO(111) structure must be along the $\langle 110 \rangle$ direction of the underlying Ag substrate. In real space, on the Ag(100) surface the close packed atomic rows with an atomic distance of 2.88 Å lie in the $\langle 110 \rangle$ direction. On the CoO(111) surface rows of closed packed atoms lie in three different directions, the distance of neighboring Co atoms (and/or O atoms) is 3.01 Å. If we put close packed atomic rows of the CoO(111) along a close packed direction of the Ag(100), the misfit is only 4.3% in this direction. Therefore, such an orientation of the domains relating to the Ag substrate is quite possible. The model structure based on this analysis is shown in Fig. 5.13. For simplicity the lattice misfit was not considered in this model.

The structure model and the resulting LEED pattern can be further confirmed by the analysis of one dimensional spot profiles. Fig. 5.14 shows two spot profile taken at 173 eV and 220 eV, respectively. By comparing these two profiles, all spots were identified and assigned in the Fig. The capital letter A and B mean that the CoO(111)

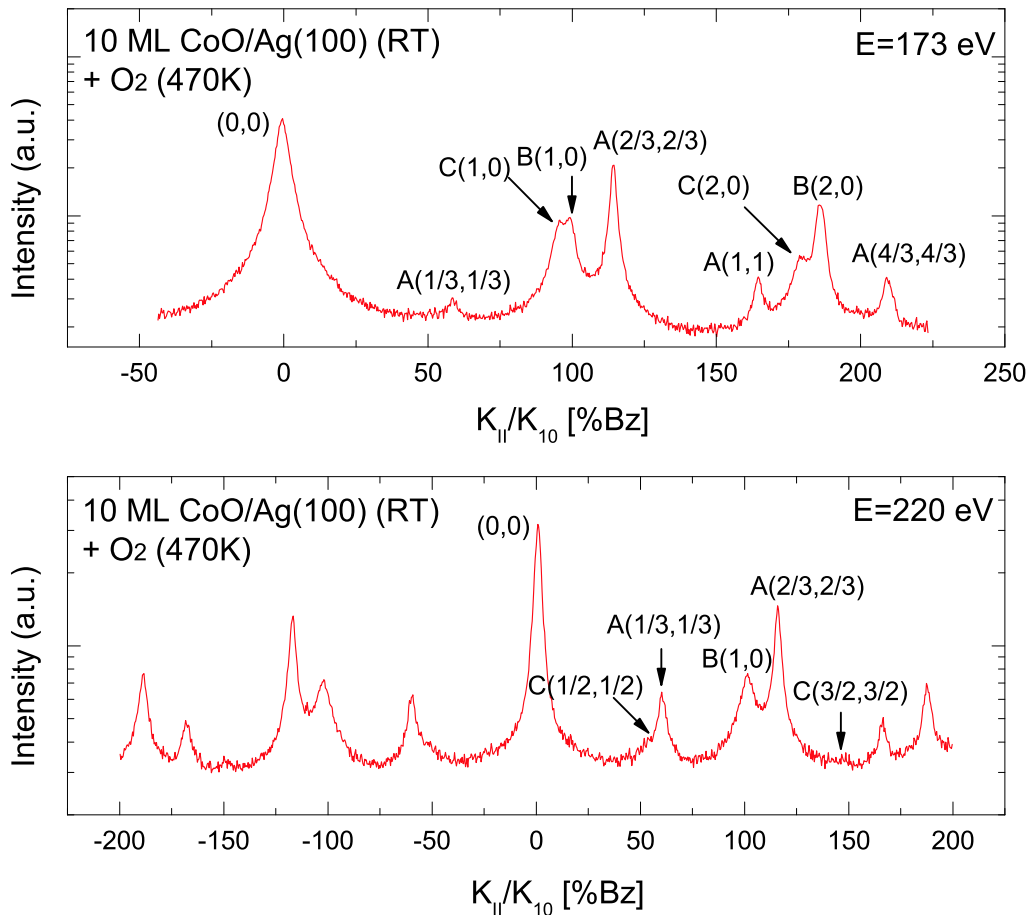


Fig. 5.14: line scan (in a logarithmic intensity scale) along $[110]$ substrate direction of 10 ML CoO disposition at RT with further annealing in an O_2 atmosphere at 470 K.

domains and C belong to (2×1) CoO(100) domain. The spot positions of B(1,0) and C(1,0) in Fig. 5.14 show the lattice mismatch between CoO(100) and CoO(111). The prefixes A, B, and C mean that the spots belong to the two $(\sqrt{3} \times \sqrt{3})R30^\circ$ CoO(111) domains and the (2×1) CoO(100) domains, respectively. Spot C(1,0) at 95.7% Bz Ag(100) corresponds to a lattice constant of 4.26 \AA , which is exactly the bulk value of CoO. However, spot B(1,0) at 99.3% Bz corresponds to a 3.5% compression of the (111) structure compared to the bulk value.

It is not uncommon, that hexagonal oxide structures can be formed on metal surfaces of cubic structure. Wang *et al.* have reported that by oxidation of Ni(100) at different temperature both NiO(111) and NiO(100) can be developed [126]. Hexagonal layer epitaxy of $V_2O_3(0001)$ on the four fold $Cu_3Au(100)$ substrate has also been published [127]. Obviously, the energies of these systems is such that the structure is mainly determined by the bonds within the films and the bonds between the structure and the and the film are of secondary importance.

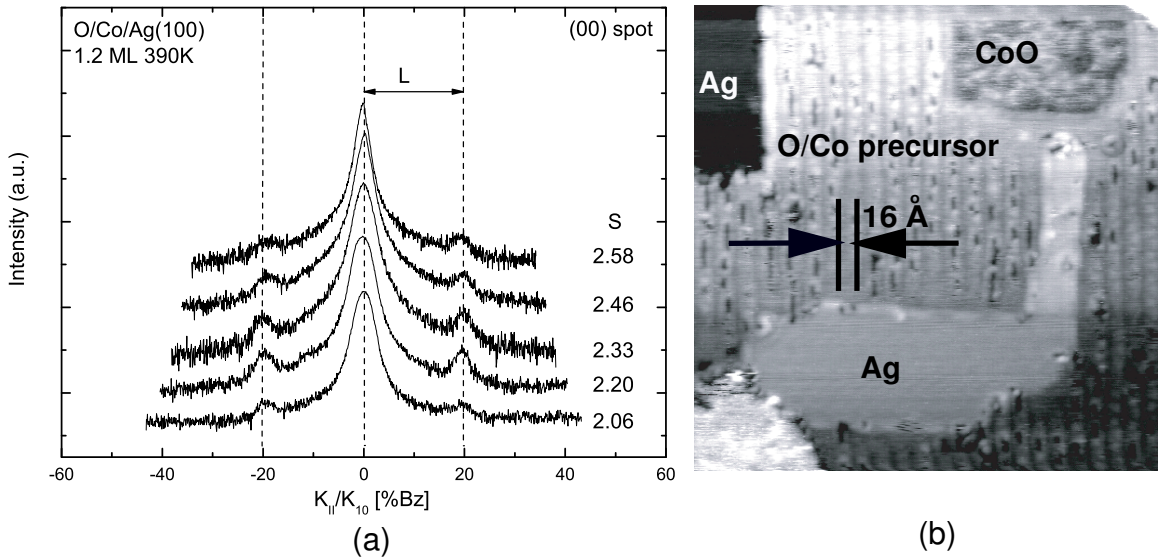


Fig. 5.15: Deposition of 1.2 ML Co in an O_2 atmosphere onto Ag(100) at a substrate temperature of 390 K. (a) (00) spot profile (in a logarithmic intensity scale) measured at different vertical scattering phase. (b) STM image obtained from the same sample. $U=-3$ V, $I=0.1$ nA, $400 \times 400 \text{ \AA}^2$.

5.2.2 Growth at 390K

The preceding part has shown that the way of how the thin film is treated by subsequent annealing in UHV or in an O_2 atmosphere plays a dominant role for the resulting structure. This means that the formation of a uniform Co oxide film is difficult to achieve and that the preparation conditions have to be investigated in great detail. For example, when the deposition was performed at a slightly elevated temperature (390 K), the resulting surface morphology was changed completely.

1.2 ML Co have been evaporated in an O_2 atmosphere ($p(O_2) = 1 \times 10^{-6}$ mbar) at 390 K without further annealing. Fig. 5.15a shows a set of (00) spot profiles taken along the $\langle 110 \rangle$ direction as a function of the vertical scattering phase S . Surprisingly, satellites at a distance $\pm L$ to the center spot were observed. It is well known that such scattering phase independent satellites come from a well defined lateral correlation length. The correlation length $\langle \Gamma \rangle$ can be calculated by the equation $\langle \Gamma \rangle = 2\pi/L$. In the present case, it is easy to get $\langle \Gamma \rangle = 14.4 \text{ \AA}$, ($L=20\%$ Bz). Fig. 5.15b shows a typical STM image measured from the same sample. It clearly shows the row structure that corresponds well to the satellite in the spot profile. The row structure turns out to be some kind of O/Co precursor and not of atomic origin, More likely, it due to a moiré structure of the substrate and the precursor lattices.

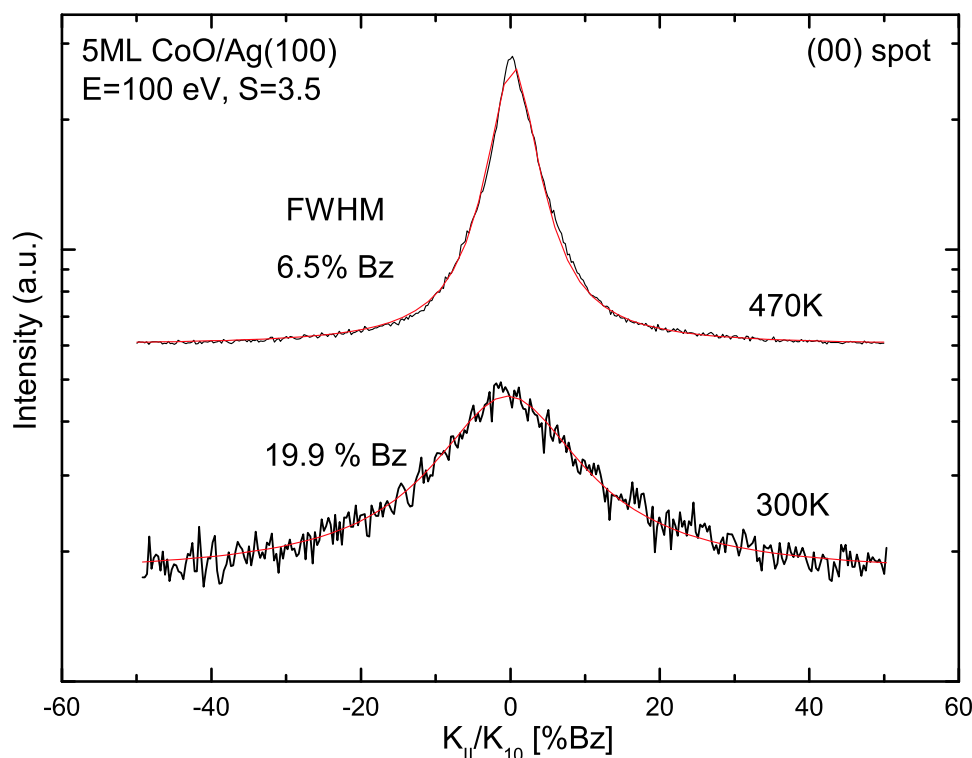


Fig. 5.16: Spot profile (in a logarithmic intensity scale) of the (00) spot at the "out-of-phase" condition at 100 eV for 5 ML CoO films grown at different substrate temperature. The FWHM of the spot profile has reduced significantly at 470 K.

5.2.3 Growth at 470K

The influence of the deposition temperature on the CoO film morphology is of special important to prove the micro roughness as energetically driven strain relief mechanism. The growth temperature has been changed from 300 K up to 570 K.

The spot profiles of the (00) spot are compared in Fig. 5.16 for two different growth temperatures. Both profiles can be described by Lorentzians, which reflect the geometric terrace width distributions. At the higher deposition temperature of 470 K the profile shows a narrow FWHM of about 6.5% Bz, corresponding to an average terrace width of 30 Å. The FWHM of the film deposited at 300 K is much larger (19.9% Bz) and corresponds to an average terrace width of 10 Å. The improved lateral roughness of the film by increasing the disposition temperature is evident. At both temperatures the spot profiles of the (00) spot vary with the vertical scattering phases.

The kinetics of the flattening of macroscopic film structures during thermal annealing has been used extensively to determine atomic diffusion coefficients at surfaces. At temperatures below the surface roughening transition, faceting has been observed as a macroscopic profile is annealed. The influence of the annealing temperature on the CoO film morphology is also important.

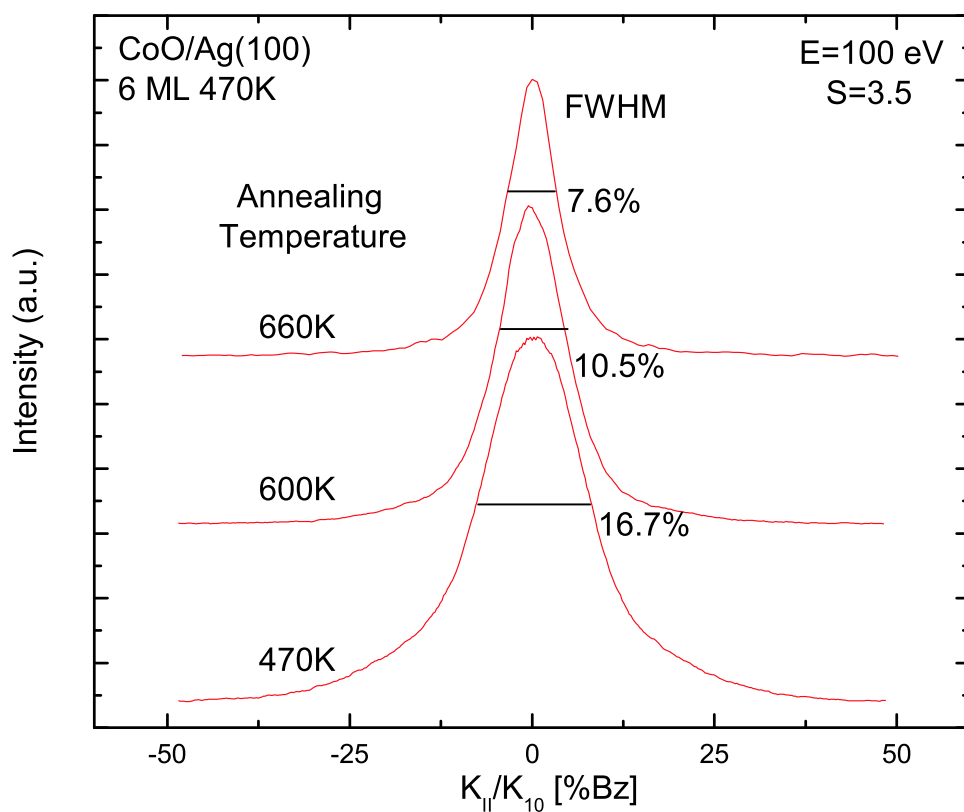


Fig. 5.17: Spot profiles (in a logarithmic intensity scale) of the (00) spot at the "out-of-phase" condition at 100 eV for 6 ML CoO films. The FWHM of the spot profile decrease with annealing temperature, the annealing time is 30 min for each temperature.

Spot profiles of the (00) spot at the "out-of-phase" condition at 100 eV for 6 ML CoO ($p(\text{O}_2) = 1 \times 10^{-6}$ mbar) films grown at 470 K and annealing at different temperature are shown in Fig. 5.17. The annealing temperature has been chosen at 470 K, 600 K, and 660 K and the annealing time is 30 min. The Lorentzians fit the profiles well. The broadening becomes sharper and more intense at higher annealing temperatures, which reflects the increasing size of the terraces or islands. The FWHM of the profiles decrease from 16.7% Bz at 470 K to 7.6% at 660 K. Correspondingly, the average terrace size increased from 17 Å at 470 K to 38 Å at 660 K.

Chapter 6

Tensor-LEED Analysis of Oxide Surfaces

6.1 The Ag(100) Surface

6.1.1 Introduction

The use of LEED as a technique for surface structural determination began with the study of clean surfaces. Low index unreconstructed surfaces of metallic single crystals were commonly chosen, because they have the lowest surface energy, hence, they are the most stable ones. The (100), (110), and (111) surfaces of face-centered cubic (fcc) and body-centered cubic (bcc) crystals as well as the (0001) surface of hexagonal close-packed (hcp) crystals have frequently been the subject of structure determinations. Although the structure of low index faces of metallic single crystals is generally well understood, especially from prior studies using quantitative LEED, studies of their surface crystallography remain of interest. They are, for example, good initial candidates for testing new structural methods, including new computational approaches for simulating LEED $I-V$ curves. A good description of the clean surface is also an important starting point to any LEED study of adsorbate covered surfaces.

Deviations of surface atomic positions from those expected for a simple termination of the bulk structure are due to the reduced coordination of the surface atoms and can involve major reconstructions. Early theoretical work [128] predicted that on most metal surfaces layer distances should increase. However, the current view is that in an ideally bulk-terminated surface, the surface layer of atoms is in a lower average valence charge density than in the bulk, and typically, the outer most layer distance contracts to reduce this effect. Investigations show that there is a correlation between the magnitude of these relaxations and atomic layer density [88], the effect being more pronounced for the more open surfaces. For example, the relatively open fcc(210) and bcc(210) surfaces show a contraction of the top layer distance by approximately 20%, whereas close or nearly close packed surfaces like Ni(111), Ru(0001) or Fe(110) are only slightly contracted or practically bulk terminated [95]. As interlayer distances are parameters normal to the surface, they can be determined with high accuracy using LEED. Error limits given frequently are in the range of $\pm 1\%$ of the top interlayer distance and in favorable cases they are even smaller than $\pm 0.01 \text{ \AA}$ on the absolute

scale. This in turn allows the check of first-principle total-energy calculations, which in most cases are in line with experimental results [129].

Ag(100) surface is one of the typical close packed metal surface with a fcc crystal structure. A small contraction or a bulk terminated surface could be expected accordingly. In fact, one experimental observation by LEED suggested no relaxation of this surface [130]. On the other hand, different theoretical calculation have been performed to study the structure of this surface. All theoretical results show an inward relaxation of the top layer. The disagreement between the theory and the experiment study might come from the experiment result, since the R_P factor of 0.39 obtained in this experimental study was quite high regarding the simple structure of Ag(100) surface and compared to other LEED studies of simple metal surfaces. Therefore, we have reinvestigated this surface by a tensor LEED analysis, which might provide a test of the theoretical prediction.

The LEED experiments in this chapter were performed by means of a four-grid rear view LEED optics installed in the UHV B system. The single crystal Ag(100) surface was cleaned in the usual way. $I - V$ curves of the diffracted beams were collected by the video LEED system. Six non-equivalent beams with beam indices (1, 0), (1, 1), (2, 0), (2, 1), (2, 2), (3, 0) and an energy range from 30-370 eV were measured. The measured LEED $I - V$ curves were normalized to constant incident electron current, smoothed, and corrected for the background. Normal incidence was considered to be achieved when reliability factors R_P (Pendry R -factor) between $I - V$ curves of symmetrically equivalent beams of 0.1 or below were obtained. All LEED $I - V$ curves in this chapter were collected at room temperature. Further details of the UHV chamber, sample preparation and the LEED data acquisition system have been described in Chapter 4.

6.1.2 TLEED Calculations

The theoretical analysis was performed assuming a muffin-tin potential model for the crystal. A muffin-tin radius of 1.446 Å was used for the Ag atoms. Clementi atomic wave functions were used as a starting point for determining the scattering potential, and a Slater exchange parameter of 2/3 was assumed [131]. The scattering phase shifts needed for the LEED calculations were derived from the Barbieri-Van Hove phase shift package [132] which were evaluated by numerical integration of the radial part of the Schrödinger equation in the muffin-tin spheres. A set of 10 ($l_{max} = 9$) phase shifts and a sample temperature of 300 K were assumed. A value of $V_0 = -(10 + 4i)$ eV was assumed for the optical potential. Different values for the imaginary part of the complex inner potential, simulating damping due to inelastic scattering processes, were tried. Thermal effects were represented by augmenting the phase shifts by a Debye-Waller factor. The Debye temperatures of both surface and bulk layers were kept constant and equal to the bulk value ($\Theta_D = 225$ K) [88].

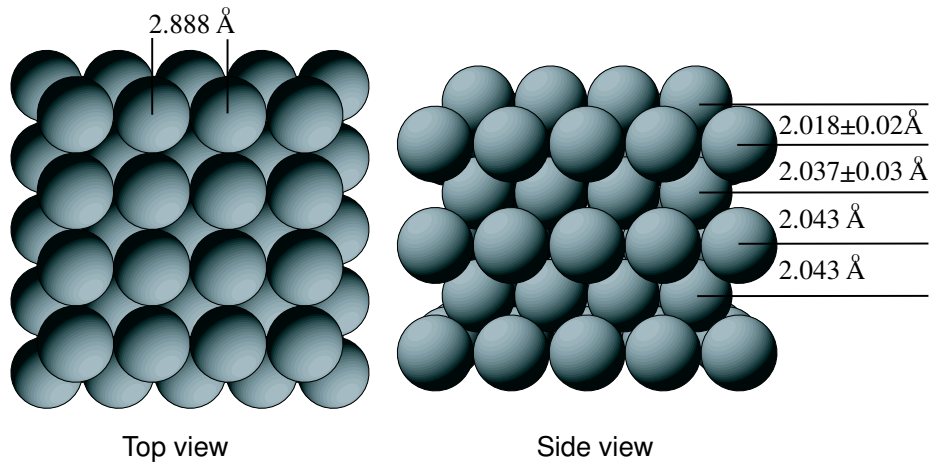


Fig. 6.1: Top view (at left) and side view (at right) of the Ag(100) surface.

For the analysis of the $I-V$ curves, the Barbieri-Van Hove symmetrized automated tensor LEED package (SATLEED) [132] was used in order to fit theoretical $I-V$ curves derived for suitable reference structures in a semiautomatic manner to the experimental data [89]. In the calculations, vertical relaxations of the atoms were allowed for the two upper layers. Lateral displacements could be excluded due to the high symmetry of the fcc(100) surface structure observed in the LEED patterns. Atoms in deeper layers were considered as fixed to the bulk positions. The layers were stacked in an alternating manner until the amplitude of the wave field was low enough to reach convergence in the renormalized forward scattering approximation (RFS scheme).

The analysis of the Ag(100) surface structures was started with the ideally terminated, unrelaxed surface as reference structure, for which in the first step of the automated tensor LEED (ATLEED) procedure the dynamical LEED calculation provides the spherical wave amplitudes, which are necessary for the rapid computation of synthetic $I-V$ curves. In the following steps, these are calculated for surface geometries deviating moderately from the reference structure and fit to the experimental curves. The procedure is based on the minimalization of the Pendry R -factor R_P which compares modified logarithmic derivatives of experimental and theoretical $I-V$ curves [89,98]. The Powell scheme was chosen as optimization algorithm.

In the last stage of the $I-V$ analysis the best-fit structures obtained were taken as new reference structures for further optimizations. These calculations led to only very subtle changes in the atom positions. Finally, the dependency of the R -factor on the structural parameters in the vicinity of the best-fit geometry was analyzed in order to judge the error bars on the obtained surface structures. Following Pendry's approach to measure the reliability of the R -factor, the standard deviation was estimated conservatively from the curvature of the R -factor curves at the optimized geometry, the

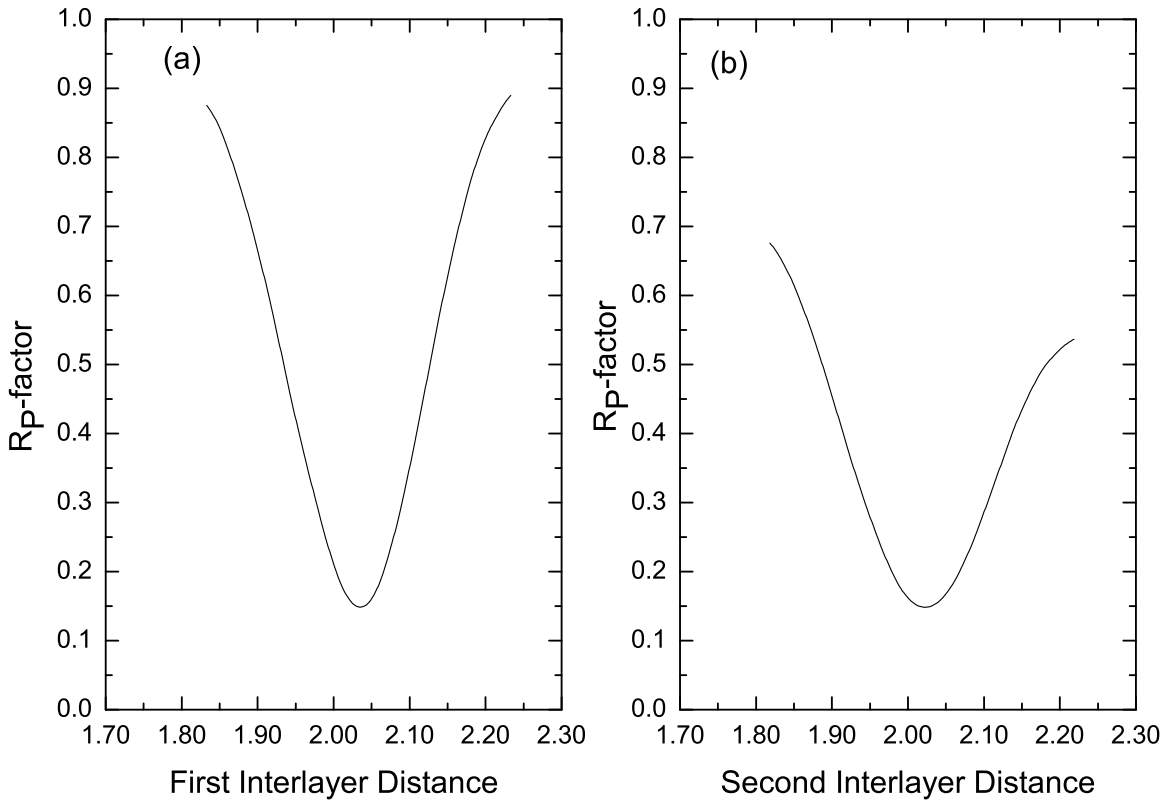


Fig. 6.2: (a) R_P as a function of the first interlayer distance d_{12} . (b) R_P as a function of the second interlayer distance d_{23} .

minimum R -factor and the overall energy range of the experimental data [89,98].

6.1.3 Results and Discussions

As summarized above, the first step of the LEED structure determination for the clean Ag(100) surface was to calculate the $I - V$ curves for the ideally terminated surface. At present, this is the only reasonable reference structure model. In the calculation a lattice constant of 4.085 \AA was used so that the layer distances for both surface and bulk layers were set to 2.043 \AA . In the second step of the structure determination, both the first (d_{12}) and second (d_{23}) interlayer distances were varied but the third interlayer distance (d_{34}) was kept constant and equal to the bulk value. This seems to be a reasonable constraint in view of the very small relaxations found in previous studies of fcc(100) surfaces, even for the outermost layer. The muffin tin zero was the only nonstructural parameter refined.

The final best-fit structure has a $R_P = 0.15$ with $\Delta d_{12} = -0.025 \pm 0.02 \text{ \AA}$ and $\Delta d_{23} = -0.006 \pm 0.03 \text{ \AA}$, which correspond to $-1.2 \pm 1.0\%$ and $-0.2 \pm 1.5\%$ of the bulk layer distance (2.043 \AA) for d_{12} and d_{23} respectively as shown in Fig. 6.1. A more quantitative view of the minimum seen is provided in Fig. 6.2, which shows two

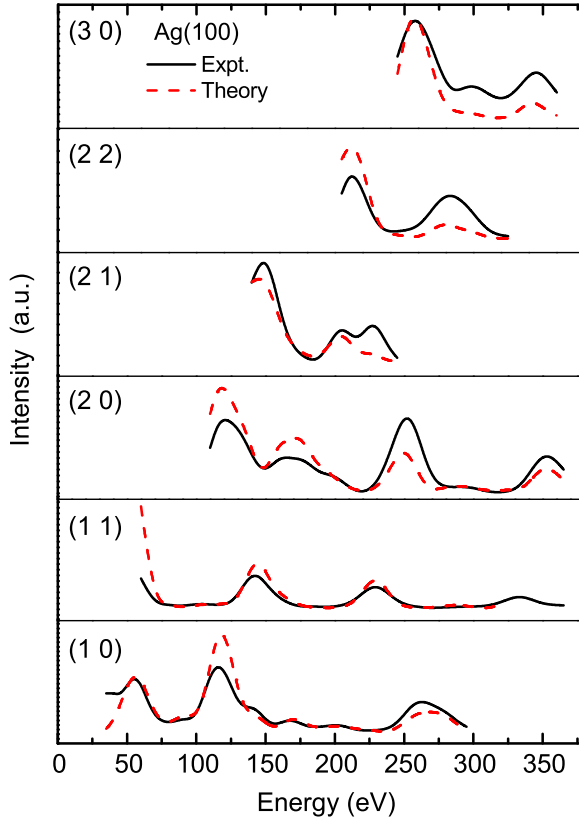


Fig. 6.3: Comparison of the experimental (solid) LEED $I - V$ curves with those calculated (dashed) for the best fit model of the clean Ag(100) surface.

orthogonal projections of the parameter space, chosen to pass through the minimum. Fig. 6.2a shows the variations of R_P respect to d_{12} , keeping d_{23} fixed at its optimum value, and Fig. 6.2b shows R_P as a function of d_{23} while keeping d_{12} fixed at its optimum value. Fig. 6.2 also provided the basis for estimating the precision of our structure determination. The standard error in the minimum value of R_P was calculated to be 0.02, leading to corresponding uncertainties in the interlayer spacing of 0.02 Å for d_{12} and 0.03 Å for d_{23} respectively.

Fig. 6.3 shows a comparison of six of the experimental $I - V$ curves used in this work with the theoretical curves obtained from the SATLEED code for the best structural model. Clearly, there is very good agreement between the experimental and theoretical data. These experimental results are in good agreement, within the quoted accuracy, with a first principles calculation of the lattice relaxation on Ag(100) done by Bohnen, Rodach, and Ho [133]. This calculation finds $\Delta d_{12} = -0.027 \text{ \AA}$ (-1.3%), $\Delta d_{23} = 0.02 \text{ \AA}$ (1.0%). Calculations based on the embedded atom method find larger relaxations of the first interlayer spacing, namely $\Delta d_{12} = -0.06 \text{ \AA}$ (-3.0%) [134] and $\Delta d_{12} = -0.04 \text{ \AA}$ (-1.9%) [135]. Other measurements of relaxations of fcc(100) metal surfaces show mainly small relaxations with $\Delta d_{12}/d_{bulk} \leq 1\%$, for Cu(100), $\Delta d_{12}/d_{bulk} = -1.1 \pm 0.4\%$ [136], for Ni(100), $\Delta d_{12}/d_{bulk} = -1.0 \pm 1.0\%$ [137].

In general, theoretical treatments of multilayer relaxations at metal surfaces predict small relaxations of the first fcc(100) layer [88]. A simple, moderately successful,

electrostatic model of relaxation predicts universal curves for relaxations at surfaces of bcc and fcc lattices against openness [138, 139]. These curves show a 1% compression of the first layer spacing of fcc(100) with respect to the bulk, and a 4% compression of the more open bcc(100) first layer spacing. Hence, the relaxation found here for Ag(100) is consistent with this model.

6.2 CoO/Ag(100) Surface

6.2.1 Introduction

Ordered thin films of transition metal oxides (NiO, CoO, MnO etc.) are general important but not much is known of their formation or structure and morphology. In the case of NiO, ordered thin oxide films can be grown by the oxidation of metal single crystal surfaces. The LEED pattern of oxidized Ni(100) surfaces, however, mostly indicates the presence of a rather imperfect NiO(100) film on top of Ni(100), which might result from the large lattice mismatch (of nearly 20%) between Ni and NiO [30]. Although the use of highly oriented Ni(100) as substrate leads to considerable improvement of the LEED pattern from the oxidised surface, the large lattice mismatch always remains a problem, with the possible consequence of defect structures in the oxide film [25].

A different approach to prepare a well ordered NiO(100) film is to evaporate Ni onto an Ag(100) surface in an O₂ atmosphere. LEED and UV photoelectron spectroscopy have shown that a well ordered and smooth NiO(100) surface can indeed be obtained in this way [31]. The reason for this more perfect growth of NiO(100) layers by using an Ag(100) substrate is the smaller lattice mismatch (only 2%) between NiO and Ag. These results were confirmed by scanning tunnelling microscopy. It has been demonstrated that deposition of Ni onto Ag(100) in an O₂ atmosphere leads to much better NiO(100) films than oxidation of Ni(100), at least for surface orientations which were accessible by standard Laue techniques [32].

CoO films grown on the Ag(100) substrate have been prepared in the same way. The growth mechanism and structure of CoO films have been investigated by different surface science methods in our previous studies [38, 124]. Despite Ag(100) appears to be an ideal substrate for the epitaxial growth of CoO, those studies show that the CoO/Ag(100) system is rather complex probably due to the larger lattice mismatch (4.3%) between CoO and Ag(100). Deposition on a slightly heated substrate at a temperature of 470 K resulted in more perfect CoO films in (100) geometry and in registry with the substrate. Owing to the large lattice mismatch between CoO and Ag(100), a layer-by-layer-like growth mode could not be expected. Indeed, we observe the tendency towards a more three-dimensional growth mode for thicker films (for example, a 10 ML of CoO film with (100) orientation). However, at the initial stage, the films show a layer-by-layer growth mode [124]. Since no moiré pattern is

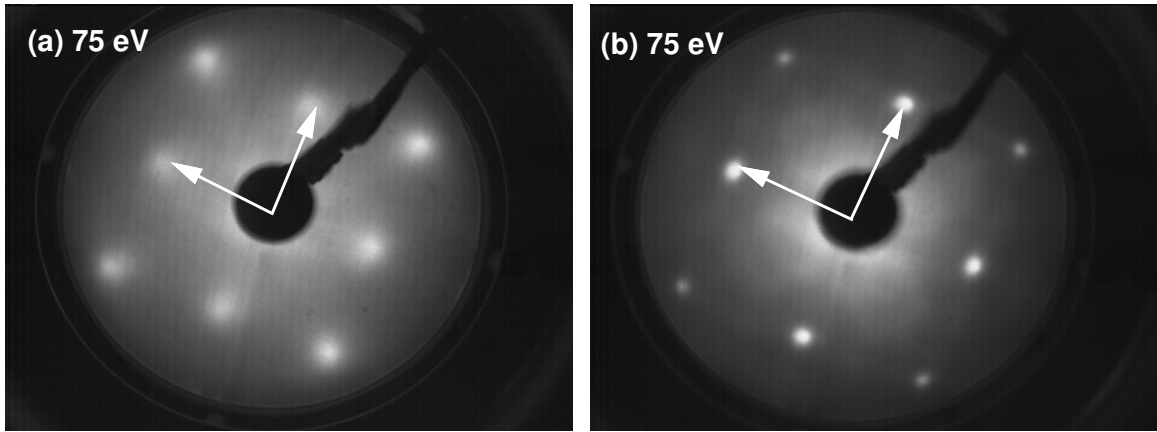


Fig. 6.4: LEED patterns for (a) CoO(100)-(1 × 1) on Ag(100) and (b) a clean Ag(100)-(1 × 1) surface, showing that the CoO film grows along the $\langle 110 \rangle$ direction of the Ag(100) unit cell. Both images were recorded at the same sample position and an incident energy of 75 eV.

detected at small coverage, we assume that the CoO(100) film first grows in a slightly compressed form. We also have concluded that the initial CoO(100) film atop the substrate grows in the form of a double layer and continues in the form of single layers at low coverage. A 2 ML thickness film then should correspond to the height of the CoO rocksalt unit cell of 4.26 Å.

It is the purpose of the present work to provide some additional structure information of CoO films grown on Ag(100) at low coverage by the LEED $I - V$ analysis, which have not been described previously. Although the single crystal CoO(100) surface has been studied by LEED $I - V$ analysis, an early full dynamic LEED structure determination revealed this surface is a simple termination of the bulk lattice without any relaxation [50]. However, this result cannot be considered as reliable, because the dataset is quite limited in this study. The CoO(100) surface becomes charged below 170 eV at room temperature and the LEED $I - V$ curves were recorded from just above this energy for three beams only. Another deficiency in this study is that the possibility of surface rumpling has not been considered. Furthermore, the surface structure of the film with low coverage might be different compared to a single crystal surface, since the substrate will influence the structure details of film.

A 4 ML CoO film was prepared in the present LEED $I - V$ analysis. It was grown by deposition of cobalt on Ag(100) in an O₂ atmosphere with 1×10^{-6} mbar partial pressure. During the deposition, the Ag(100) substrate temperature was kept at 470 K, this growth condition proved to be the optimized growth condition in our previous investigation. For LEED $I - V$ measurement, five inequivalent beams with an energy range from 30 to 400 eV were measured.

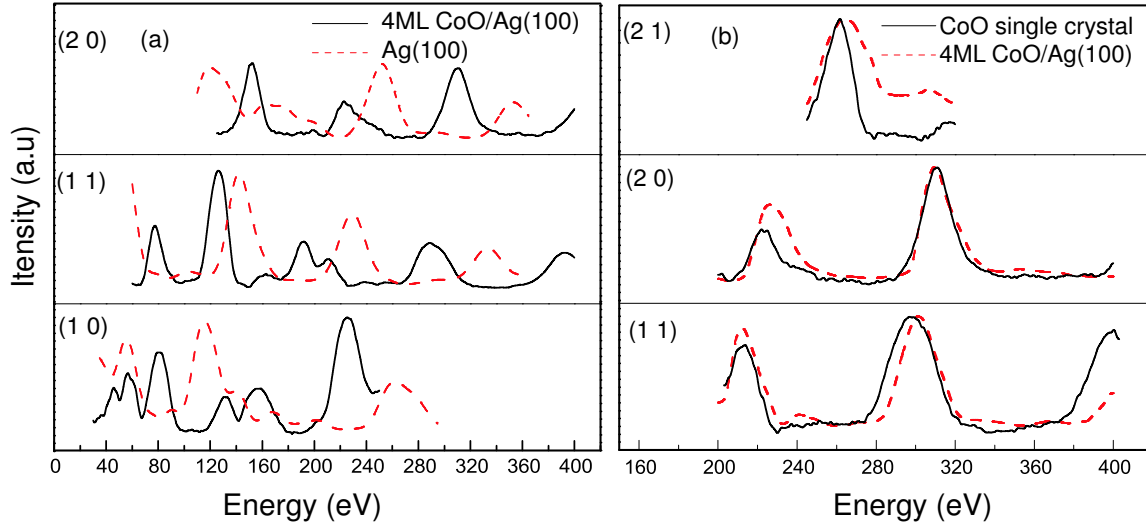


Fig. 6.5: LEED $I - V$ curves comparison. (a) Clean Ag(100) and 4 ML CoO on Ag(100). (b) 4 ML CoO on Ag(100) and single crystal CoO(100) surface. (The $I - V$ curves measured for the single crystal CoO(100) surface are taken from ref. [50])

6.2.2 TLEED Calculations

The analysis of LEED $I - V$ curves was again performed by the Barbieri-Van Hove Symmetrized Automated Tensor LEED package (SATLEED) [132]. Following Roberts *et al.* [140] and Barbieri *et al.* [141], phase shifts of neutral atoms instead of ions were derived from the Barbieri-Van Hove phase shift package [132] in order to treat elastic scattering at the ion cores. Ten phase shifts $l_{max} = 9$ were used in the LEED calculations. The phase shifts for Ag and CoO were calculated from the muffin-tin potentials of Ag and CoO single crystal respectively. An additional set of phase shifts of Co and O was calculated from the muffin-tin potential of a 4 ML film of CoO(100) on a Ag(100) surface (to avoid problems with different values of the inner potential of Ag and CoO). Test LEED calculations performed with the two sets of phase shifts lead to results that do not differ significantly. The LEED calculations were performed between 30 and 400 eV. The imaginary part of inner potential was set to 5 eV, whereas the real part was set to 10 eV and optimized in the search procedure. The Debye temperatures were initially set to 385, 500 and 225 K for Co, O and Ag respectively. In the automated structure search, 5 non-equivalent experimental $I - V$ curves with a total energy range of about 1025 eV were measured for analysis.

6.2.3 Results and Discussions

After deposition a 4 ML thick CoO film at a temperature of 470 K and annealing at 500 K, a sharp LEED pattern was produced, which is represented along with the clean Ag(100) substrate LEED pattern in Fig. 6.4a and 6.4b respectively. The square

diffraction pattern of the CoO film confirms the identity of CoO with its (100) orientation. Additional proof can be seen in the direct comparison of the LEED $I - V$ curves. In Fig. 6.5a the LEED $I - V$ curves of (1, 0), (1, 1), (2, 0) beams measured for a clean Ag(100) surface and a CoO film on Ag(100) are compared. The curves are substantially modified by the presence of the 4 ML thickness CoO film. On the other hand, the curves of the (1, 1), (2, 0), (2, 1) beams are very similar to those measured for a single crystal CoO(100) surface as shown in Fig. 6.5b. These $I - V$ curves possess the same maxima and minima, within a variation of 1 eV. Fig. 6.5 corroborates the proposition that the CoO film on the Ag(100) substrate has the same structure as the single crystal CoO(100) surface.

Table 6.1 Minimum values of the Pendry R -factor R_P obtained from calculations performed for pseudomorphic CoO(100) films of various thickness. For each thickness, the calculations were performed for three registries of the CoO film with respect to the Ag(100) substrate. A: Co atoms directly above Ag atoms and O atoms in hollow sites. B: O atoms directly above Ag atoms and Co atoms in hollow sites. C: Co and O atoms in bridge positions.

Registry	2ML	3ML	4ML	5ML
A	0.47	0.35	0.31	0.30
B	0.45	0.31	0.27	0.30
C	0.65	0.64	0.63	0.63

The (100) surface of CoO consists coplanar crystal layers with alternating cation-anion pairs. Similar to the Ag(100) surface, lateral displacements could be excluded due to the high symmetry of the rocksalt structure and the (1×1) surface structure observed in the LEED patterns.

As a reference structure model we considered a pseudomorphic CoO(100) film as revealed by the SPA-LEED analysis. In this structure model the in-plane lattice parameter is compressed by about 4% with respect to the bulk CoO value (3.012 Å), i.e., the same lattice parameter as bulk Ag single crystal (2.888 Å). The interlayer distance between the CoO layers was set equal to that of bulk CoO (2.13 Å). For the CoO-Ag(100) interface structure, three possible registries of the CoO film with respect to the Ag(100) substrate were considered: Co atoms on-top Ag atoms and O atoms in hollow sites (model A), O atoms on-top of Ag atoms and Co atoms in hollow sites (model B), and both O and Co atoms in bridge sites (model C). For all models, CoO layers were treated as composite layers, for which a single scattering T-matrix was calculated. For vertical relaxation of the ions, the two upper CoO layers were allowed. The deeper CoO layers as well as the Ag substrate layers was fixed. The atoms in the Ag substrate were fixed to their bulk positions. Since we have no O-Ag and Co-Ag bond length information of the CoO/Ag(100) system, for all models, the interlayer distance at the CoO/Ag interface was varied from 1.93 to 2.93 Å in steps

of 0.10 Å, each value corresponding to a new reference structure. For each registry, the calculations were performed for two, three, four and five layers of CoO.

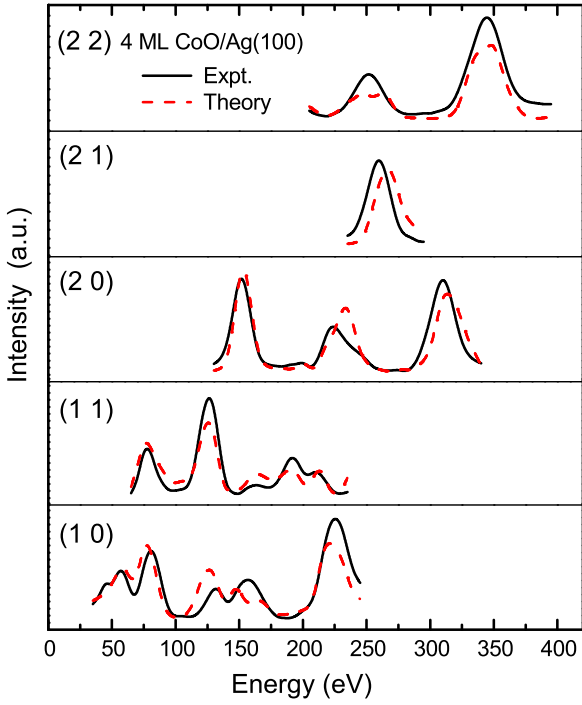


Fig. 6.6: Comparison of the experimental LEED $I - V$ curves with those calculated for the best fit model of the 4 ML CoO/Ag(100) structure. Experimental (solid) and theoretical (dashed).

The minimum values of the R_P obtained for the models described above are reported in Table 6.1. The best fit is obtained for a CoO film having a thickness of four layers with O atoms on top of Ag atoms at the interface (model B).

Table 6.2 Description of the refined 4 ML CoO(100)/Ag(100) structure. The subscripts on the atom labels correspond to the subscripts used in the text and Fig. 6.7. The surface region refers to the atoms at the vacuum-solid interface that were allowed to be refined in the calculation. Absolute lateral positions of the atoms are given in two dimensional Cartesian coordinates. The perpendicular lattice positions are defined relative to the previous atom's position as Δd_z .

Region	Atomic species	Atom number	X(Å)	Y(Å)	Δd_z (Å)
Surface	O ₁	1	1.444	1.444	0.000
Surface	Co ₁	2	0.000	0.000	0.060±0.04
Surface	O ₂	3	1.444	1.444	2.251±0.04
Surface	Co ₂	4	0.000	0.000	0.013±0.04
Bulk	O ₃	5	1.444	1.444	2.179±0.04
Bulk	Co ₃	6	0.000	0.000	0.000
Bulk	O ₄	7	1.444	1.444	2.130
Bulk	Co ₄	8	0.000	0.000	0.000
Bulk	Ag ₁	9	1.444	1.444	2.400
Bulk	Ag ₂	10	0.000	0.000	2.043

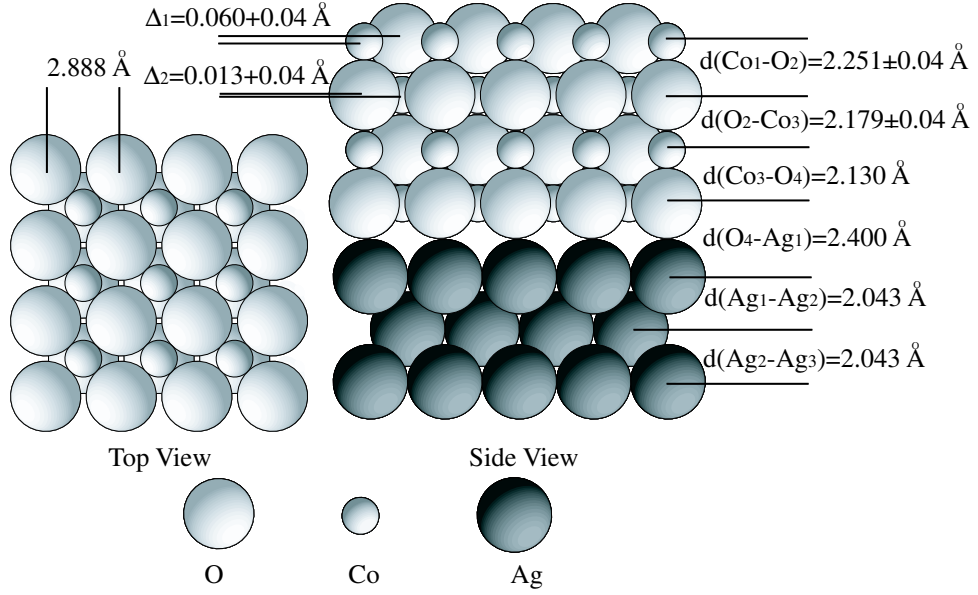


Fig. 6.7: Top view (at left) and side view (at right) of the optimized CoO(100) surface grown on Ag(100) (the surface termination is on top). The values of the interlayer and intralayer spacings are shown.

The difference of the R_P factors between model A and B is small but significant. As expected, the differences amongst the registries decrease upon increasing the thickness of the film. The results of the analysis are consistent with the nominal thickness of the film, since the best fit is obtained for a film 4 ML thick. Starting from the optimized coordinates, a new reference structure calculation was performed. In addition to the structural parameters, also the imaginary part of the inner potential and the Debye temperatures of the atoms were optimized in the analysis. After refining, a minimum R_P of 0.20 was obtained. It was found that $\Theta_{Co} = 440$ K, $\Theta_O = 480$ K and $\Theta_{Ag} = 245$ K improved R_P by 0.003 with no effect on the structural parameters. The optimized CoO/Ag(100) interface distance (O-Ag bond) was found to be 2.40 Å. The optimized inner potential is $V_0 = -(9 + 4i)$ eV. Fig. 6.6 compares the theoretical $I - V$ curves, which resulted from this last stage of refinement, to the experimental curves. The final structure for model B with an $R_P = 0.20$ is described in Table 6.2 and illustrated in Fig. 6.7. This represents the structure as determined for the 4 ML CoO(100) film on Ag(100).

The largest deviations from the CoO film structure occurred in the surface layer, where the O anions, which in the bulk would be coplanar with the Co cations, relaxed outwards and introduced a surface layer corrugation of $\Delta_1 = 0.060 \pm 0.04$ Å. The $d(\text{Co}_1\text{-O}_2)$ distance, where the indices number the layers, was expanded to 2.251 ± 0.04 Å from the bulk value of 2.13 Å. No buckling of anions or cations was found in the second layer, where the intralayer spacing was $\Delta_2 = 0.013 \pm 0.04$ Å. As with $d(\text{Co}_1\text{-}$

O₂), the second interlayer spacing $d(\text{O}_2\text{-Co}_3)$ was expanded from the bulk value 2.13 Å to 2.18 ± 0.04 Å. Since the inplane lattice parameter of the CoO film is compressed, an expansion of the interlayer spacing would be expected. Indeed, an expansion of the interlayer distances ($1.9 \pm 0.4\%$) for a pseudomorphic NiO film 3 ML thick grown of Ag(100) was found by means of Primary-beam Diffraction Modulated Electron Emission (PDMEE) [142]. This technique, which is similar to X-ray Photoelectron Diffraction (XPD) [143], was applied successfully to study the MgO/Ag(100) interface [144]. The expansion of the interlayer distance determined by PDMEE is compatible with LEED results [145]. It was decided that another possible reference structure can be made by expanding the unit cell from a pseudomorphic Ag lattice constant of 4.09 Å to 4.26 Å, i.e. expanding the lattice parameter to the exact CoO bulk value. The same structural and nonstructural parameters were refined in this model as in the previous one. For this model, however, the obtained R_P factor of 0.43 was higher than for the pseudomorphic (compressed) model. Therefore, this model can be excluded. Taking into account the SPA-LEED results, the critical thickness for the strain relief transition might happen between 4-6 ML.

In summary, CoO has been successfully prepared in its (100) orientation on Ag(100). For the 4 ML thickness film, the film's in-plane unit cell vectors were compressed by 4.3% of the bulk value. Deviations from the bulk CoO(100) atomic positions were 5.6% and 2.4% expansion of the first and second interlayer spacings, respectively. The difference in outward movement of the surface O anions and Co cations cause a buckling of 0.06 Å.

6.3 BaTiO₃(111) ($\sqrt{3} \times \sqrt{3}$) $R30^\circ$ Surface

6.3.1 Introduction

There is increasing interest in the surface properties of metal oxides because of their important technological applications as catalysts, corrosion resistant coatings as well as in electronic devices. Barium titanate (BaTiO₃), for example, is a ferroelectric wide band-gap semiconductor and is used in many applications such as non-volatile ferroelectric memory and varistors in protection circuits in order to prevent thermal overload. The knowledge of the structure and energetics of oxide surfaces is essential for an understanding of their physical and chemical properties. In the case of polar metal oxide surfaces, the atomic structures of these surface orientations can deviate strongly from their corresponding bulk truncations. This is predicted by many theoretical studies, but only a few experimental surface structure determinations exist so far. The (111) surfaces of oxides with the perovskite structure such as BaTiO₃ become stabilized by severe reconstructions by different preparation conditions. Other surfaces do not reconstruct but become stabilized by strong interlayer relaxions in their surface regions. The topmost interlayer spacings of Cr₂O₃(0001) [146], α -Al₂O₃(0001) [147, 148]

and $\alpha\text{-Fe}_2\text{O}_3(0001)$ [149] surfaces are reduced by up to 86% of the corresponding bulk spacings. These distortions are much larger than those found for metal and semiconductor surfaces, including weakly polar compound semiconductors, and they strongly influence the surface chemical properties of these materials. The reasons for the large relaxations still are subject of current research. A dominating driving force for them is electrostatic potentials that can build up at such surfaces, because the atomic planes along polar crystal directions consist only of either positively charged cations or negatively charged anions. These electrostatic potentials can be compensated or reduced by surface reconstructions or interlayer relaxations.

The large relaxations make a reliable structure determination with LEED crystallography very time consuming. They usually exceed the convergence radius of LEED calculation algorithms, and therefore a large number of structural searches with different reference structures as starting points have to be performed. For oxides with complex crystal structures a large number of different surface terminations are possible and have to be taken into account. Structure models with missing atoms or adatoms in the topmost layers further increase this number. On the experimental side the preparation of oxide surfaces with defined structures and chemical compositions turned out to be very difficult and to depend critically on the preparation procedure [1]. For a number of oxides the formation of different surface structures that coexist on the sample surface has been observed under certain preparation conditions [149–151]. Therefore, the possible coexistence of different surface structures as well as the surface defect concentrations should be clarified by suitable techniques such as STM before a LEED analysis is performed.

In our previous STM and LEED studies on the $BaTiO_3(111)$ surface, it turned out that unlike the unreconstructed $SrTiO_3(111)$ surface, various superstructures were found depending on the preparation procedure. In summary, vacuum annealing at 1470 K resulted in a ($\sqrt{3} \times \sqrt{3}$) $R30^\circ$ superstructure and annealing in oxygen lead to a mixture of (1×1) and (2×2) . Subsequent vacuum annealing produced a mixture of ($\sqrt{3} \times \sqrt{3}$) $R30^\circ$ and (2×2) [87,152]. However, no experimental quantitative structure determination has been reported so far for these surfaces. The ($\sqrt{3} \times \sqrt{3}$) $R30^\circ$ reconstruction is more interesting because it is always observed after annealing the sample up to 1470 K and is usually obtained on new samples. The previous STM and LEED studies motivated the present LEED $I - V$ analysis aimed to determine the surface structure of the ($\sqrt{3} \times \sqrt{3}$) $R30^\circ$ reconstructed $BaTiO_3(111)$ surface.

6.3.2 Surface Structure of $BaTiO_3(111)$

Fig. 6.8a shows the top view of a bulk terminated $BaTiO_3(111)$ surface with BaO termination. Fig. 6.8b shows the side view of the layer structure when cut through the dashed line as indicated in Fig. 6.8a. The BaO-Ti double layers form a ...AB-CABC... stacking sequence along the $[111]$ direction, which is indicated by the capital

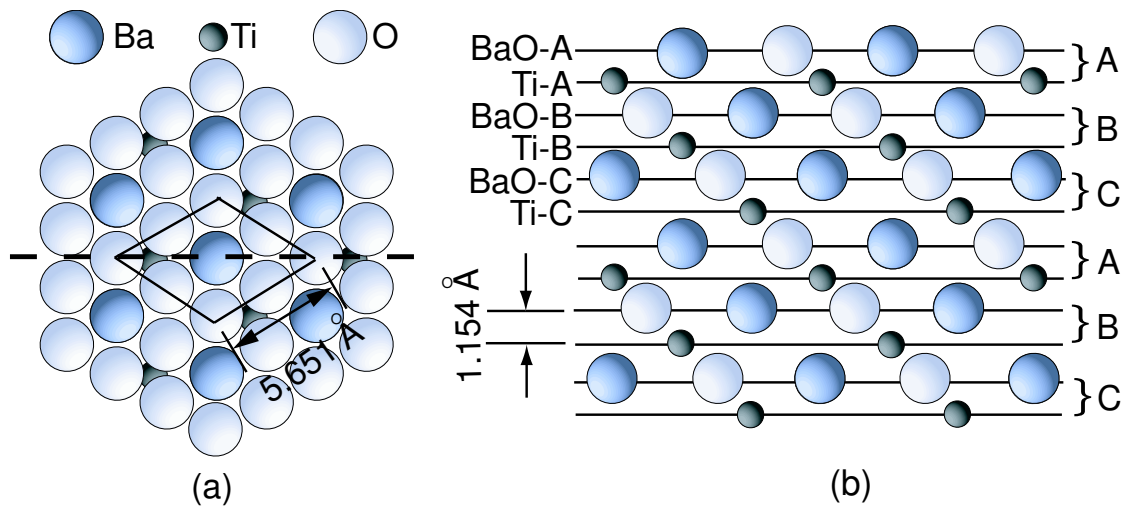


Fig. 6.8: Top view (a) and side view (b) of the BaTiO₃ structure exposing a (111) surface plane without interlayer relaxations. Two types of notation for the layer stacking along the [111] direction are given on the left and right side of (b), for explanation see text. In the top view in (a) the BaTiO₃-(1 × 1) surface unit cell with a lattice constant of 5.651 Å is indicated. The layer spacing between the single BaO and Ti layer is 1.154 Å.

letters A, B, and C on the right of Fig. 6.8b. Here, each letter denotes the lateral registry of the surface unit cell. Considering the lateral registry A, B, or C of the surface unit cell, six inequivalent bulk terminations can be obtained by cutting the BaTiO₃(111) stacking sequence. Each termination can be described by the stacking sequence notation indicated in the left of Fig. 6.8b. The layer spacing between the single BaO and Ti layers is 1.154 Å. The two dimensional (1 × 1) unit cell (double layer unit cell) contains five atoms (Three O atoms, one Ba atom and one Ti atom, see Fig. 6.8a). For the BaO terminated surface, three O atoms in the top layer are symmetrically equivalent and coordinated to one top layer Ba atom and one Ti atom in the second layer. Each Ba atom is coordinated by six O atoms, which in turn form bridges between neighboring Ba atoms. This structure leads to an O-rich BaO₃ composition in the top surface layer and a negatively charged surface. The Ti-terminated surface consists of Ti only in the topmost layer. This termination is O-deficient and positively charged. The Ti atoms in the top layer do not bond to each other, because the distance (5.651 Å) between them is too large. Therefore, they are coordinated only by three O atoms of the BaO₃ layer below.

Another striking difference between the BaO termination and Ti termination is that the Ti-terminated top layer is more open than the BaO-terminated one. It is to be expected that the excess charge on either bulk-like terminated surface and the mismatch in stoichiometry of oxygen and the respective metal lead to high surface energies for both such surface terminations, which makes the $(\sqrt{3} \times \sqrt{3})R30^\circ$ surface reconstruction.

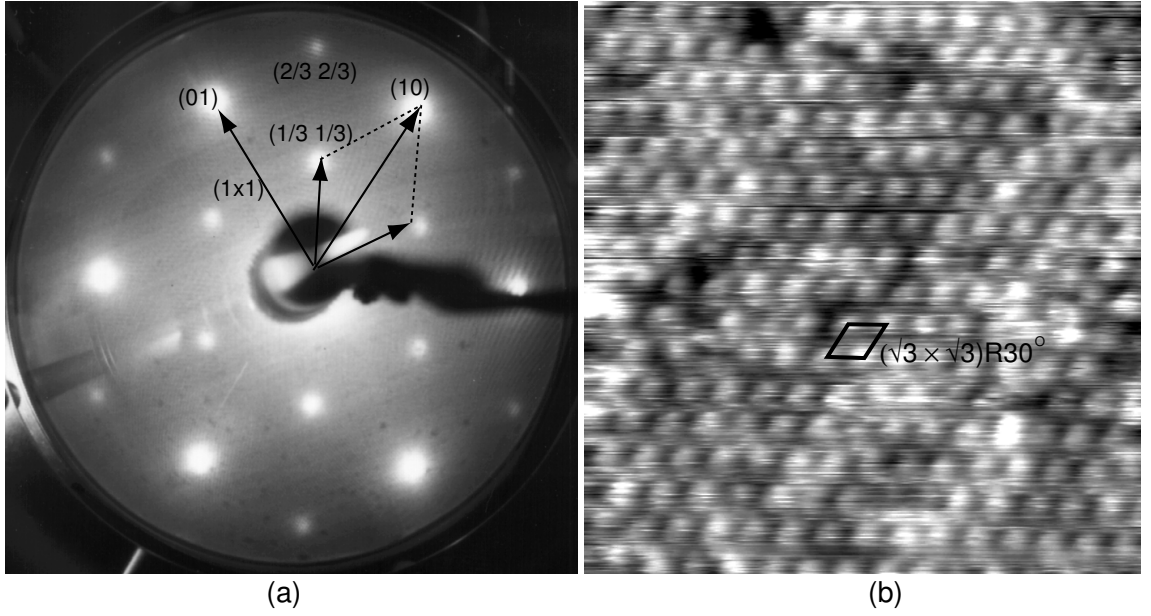


Fig. 6.9: (a) LEED pattern of the $(\sqrt{3} \times \sqrt{3})R30^\circ$ superstructure of $\text{BaTiO}_3(111)$ measured at room temperature after vacuum annealing the single crystal up to 1470K, the size of $(\sqrt{3} \times \sqrt{3})R30^\circ$ unit cell is outlined, (normal incidence, $E = 16$ eV). (b) STM image ($160 \times 160 \text{ \AA}^2$) of the $\text{BaTiO}_3(111)$ $(\sqrt{3} \times \sqrt{3})R30^\circ$ superstructure. The image corresponds to the tip height at $U_{gap} = -1$ V and $I_{tunnel} = 0.016$ nA. The mark shown in the image represents the $(\sqrt{3} \times \sqrt{3})R30^\circ$ superstructure unit cell but not the individual atoms. This image is obtained at similar preparation conditions as the LEED experiment

6.3.3 TLEED Calculations

Another tensor LEED package, which was derived from the Erlangen Tensor LEED package (TensErLEED) [153] and written by Dr. Ch. Ammer, was used to analyze the $I - V$ data in this investigation. In this package, the layer doubling approximation was implemented to calculate the interlayer multiple scattering, which was not available in SATLEED package. This feature is critical in computations of systems with short interlayer distances such as the $\text{BaTiO}_3(111)$ surface, because the layers in the $\text{BaTiO}_3(111)$ surface (only 1.154 \AA) might be too close to ensure convergence of the multiple scattering within the renormalized forward scattering (RFS) approximation as implemented in SATLEED package. In fact, we have tried to perform such calculations with the SATLEED package, but the convergence problem showed up.

Non-relativistic scattering phase shifts were calculated for Ba, Ti and O in the cubic perovskite BaTiO_3 structure. Due to the short layer spacing, we defined composite layers, consisting of two layers for all models considered. For example, the BaO termination was separated into BaO-Ti slabs as the surface composite layer. Two composite layers were defined as surface region, where the coordinates of the atoms within these composite layers can be displaced in the structure search. Con-

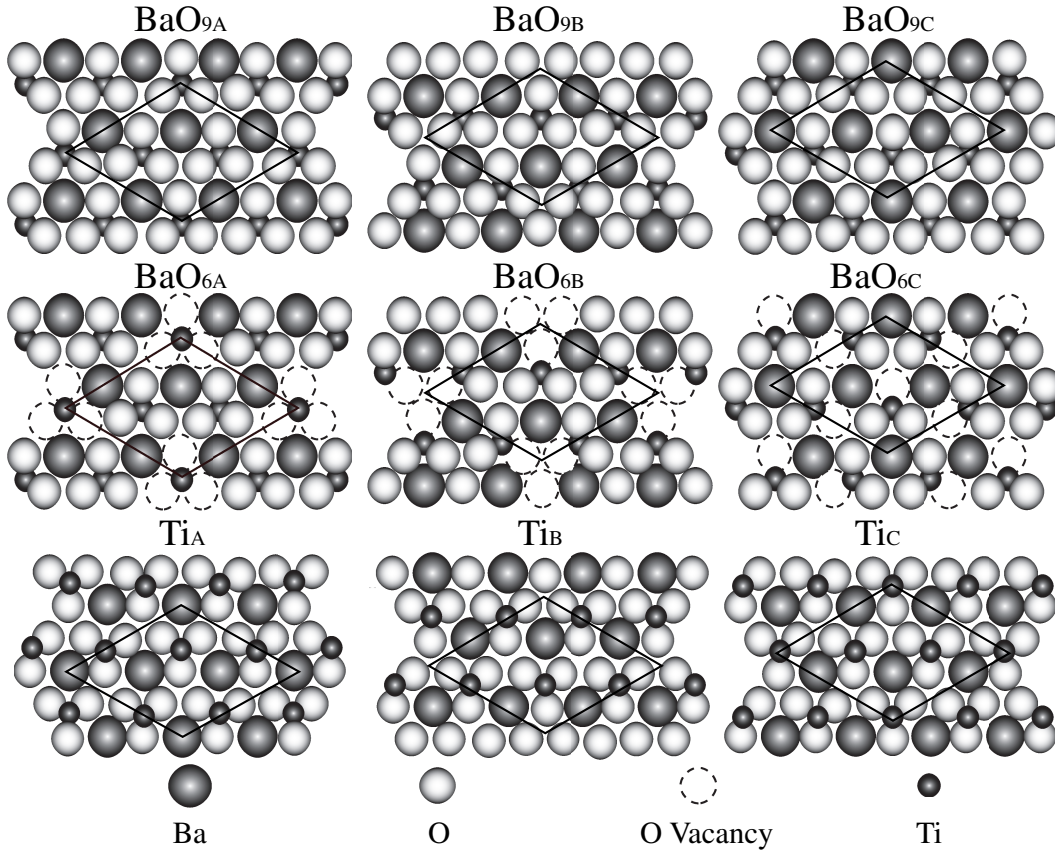


Fig. 6.10: Structure models of $\text{BaTiO}_3(111)$ $(\sqrt{3} \times \sqrt{3})R30^\circ$ surface proposed in the present analysis. Both Ba terminated and Ti terminated surface structures were considered. BaO_{9A-C} represent stoichiometric BaO terminated surfaces with a BaO_9 composition of the $(\sqrt{3} \times \sqrt{3})R30^\circ$ surface unit cell in the topmost layer. BaO_{6A-C} represent nonstoichiometric BaO terminated surfaces with 3 symmetry equivalent O atoms removed in each surface unit cell in the topmost layer. Ti_{A-C} are ideal Ti terminated surface structure models without removal of O atoms in the BaO layer below the topmost Ti layer. Capital letters A, B, and C denote the lateral registry.

sequently, we had to consider 30 atoms. Other slabs represent the bulk repeat unit (see Fig. 6.8b). Multiple scattering within each composite layer was treated exactly by the Beeby inversion scheme, the interlayer scattering was described by the layer doubling approximation. The search for the best-fit structure model was performed by a modified random sampling algorithm, which compromises between global and local search features [154]. Eight phase shifts ($l_{max} = 7$) were used in the LEED calculations. A temperature of 300 K and Debye temperatures of 308 K, 521 K, and 900 K were assumed for Ba, Ti, and O, respectively. The imaginary part of the inner potential V_{0i} was fixed to a value of 5 eV. The real part V_0 was fitted within each calculation starting from a value of 10 eV.

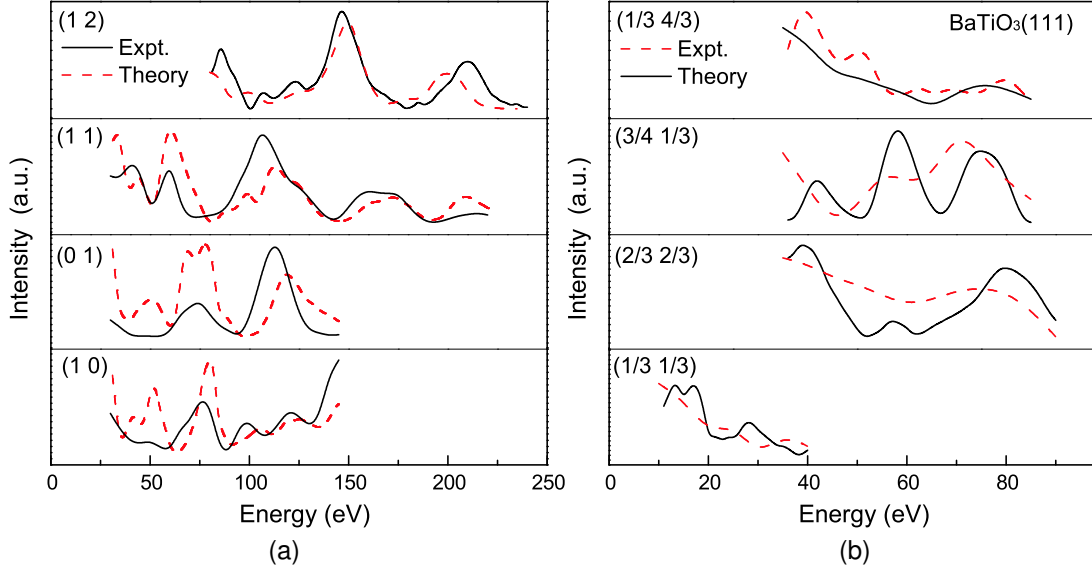


Fig. 6.11: Comparison of the experimental and theoretical $I - V$ curves for the best fit structure obtained for the $\text{BaTiO}_3(111) (\sqrt{3} \times \sqrt{3})R30^\circ$ surface. The data set covers a total energy range of 800 eV and reveals a Pendry R -factor of 0.40.

6.3.4 Results and Discussions

Fig. 6.9a shows the $(\sqrt{3} \times \sqrt{3})R30^\circ$ LEED pattern of the $\text{BaTiO}_3(111)$ surface at an electron energy of 16 eV. The image shows the $(1, 0)$ and $(0, 1)$ spots of the bulk unit cell as well as the $(1/3, 1/3)$ and $(2/3, 2/3)$ fractional order spots of the superstructure. A qualitative visual analysis of the energy dependence of the hexagonal pattern reveals the actual threefold symmetry of the pattern. However, only the integer order spots of the pattern show two distinct groups of symmetry equivalent spots. This indicates three additional mirror axes, leading to a $p3m1$ symmetry. Fig. 6.9b shows a typical STM image ($160 \times 160 \text{ \AA}^2$) of the $\text{BaTiO}_3(111) (\sqrt{3} \times \sqrt{3})R30^\circ$ superstructure measured from the same sample. The $(\sqrt{3} \times \sqrt{3})R30^\circ$ superstructure with a unit length of 9.788 \AA can clearly be identified, with each bright feature on the image corresponding to one unit cell of the superstructure. With the $(\sqrt{3} \times \sqrt{3})R30^\circ$ reconstruction, the $\text{BaTiO}_3(111)$ surface unit cell becomes three times larger than the unreconstructed (1×1) unit cell. Each double layer unit cell now has nine O atoms, three Ba atoms and three Ti atoms in the case of a bulk termination.

For a detailed LEED $I - V$ analysis, structure models have to be assumed at first. Due to the large unit cell of the reconstruction, the possible structure models are large and are very time consuming to perform the calculation if we just consider the unit cell symmetry. However, some structure models could be excluded convincingly, based on our previous experimental analysis. For example, we have assumed that the $(\sqrt{3} \times \sqrt{3})R30^\circ$ superstructure is related to a Ba-O termination and suggested

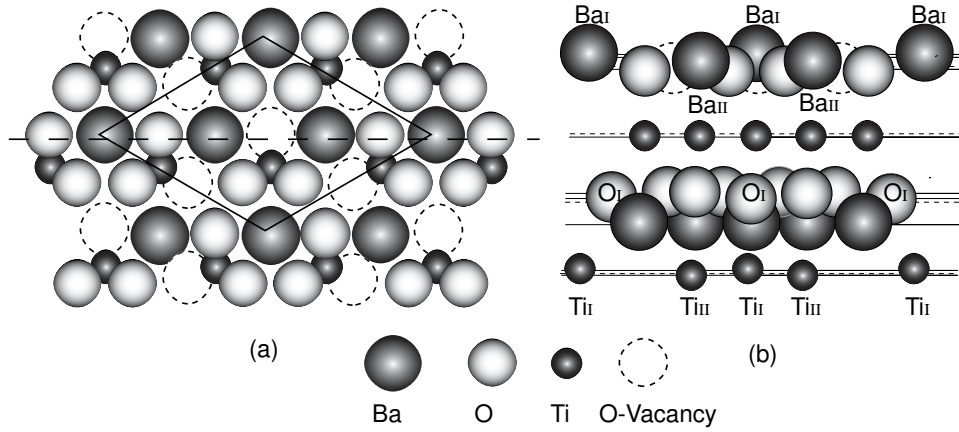


Fig. 6.12: (a) Top and (b) side view of the $\text{BaTiO}_3(111)$ $(\sqrt{3} \times \sqrt{3})R30^\circ$ surface structure with the interlayer relaxations, the details of the structure parameter are list in table 6.4, dashed line indicate the bulk position, the unit cell of $(\sqrt{3} \times \sqrt{3})R30^\circ$ superstructure are indicated in the top view.

a structural model of this surface, where one-third of the Ba atoms of the top layer was removed along with their six neighboring O atoms [87]. However, the STM image shows no indication that the reconstruction involves the removal of large groups of atoms. Obviously, the surface seems to be stabilized in a much more subtle way. The superstructure might be due to small lateral and/or vertical shifts of atoms/groups from their positions in the (1×1) mesh. On the other hand, a theoretical investigation for the related $\text{SrTiO}_3(111)$ surface shows that charge compensation and the corresponding energetic stabilization of the surface could be achieved without the removal of O atoms simply by symmetry breaking through moving one O atom out of three further away from the Ti atom below [152]. Based on this consideration we restricted our search to models for the $\text{BaTiO}_3(111)$ surface with bulk termination (Both BaO or Ti terminated) and BaO terminations with one-third of the O atoms removed in the top layer $(\sqrt{3} \times \sqrt{3})R30^\circ$ unit cell. All models considered in the first step of full dynamic reference structure calculations are shown in Fig. 6.10. Models with two-thirds of the O atoms removed in the first layer were not considered, because of their charge compensation problem.

Table 6.3 Pendry R -factor R_P obtained from calculations performed for all models considered in this investigation as shown in Fig. 6.10.

Models	R_P	Models	R_P	Models	R_P
BaO_{9A}	0.42	BaO_{9B}	0.41	BaO_{9C}	0.42
BaO_{6A}	0.41	BaO_{6B}	0.46	BaO_{6C}	0.40
Ti_A	0.54	Ti_B	0.52	Ti_C	0.50

In the second step of the structure search, 8 beams with a total energy range of

800 eV was used. The vertical coordinates of the topmost 27 to 30 atoms (within the two topmost composite layers) were varied under the restriction to keep the $p3m1$ symmetry. Although lateral displacements were possible regarding the structure symmetry, for simplicity and computation time consideration, only vertical displacement were allowed, since LEED is not very sensitive on lateral displacements in normal incidence geometry. Due to this restrictions, the search is reduced to 9-11 variables for the different models.

Table 6.4 Details of the best-fit structure (model BaO_{6C}) of the $BaTiO_3(111)$ ($\sqrt{3} \times \sqrt{3}$) $R30^\circ$ surface. X, Y, Z are the coordinates of bulk positions used in the calculation. The displacement Δd_z in the Z direction is defined relative to the original bulk position, negative displacements mean outward relaxation.

Layer	Atomic species	X(Å)	Y(Å)	Z(Å)	Δd_z (Å)
1	Ba _I	0.000	0.000	0.000	-0.24
1	Ba _{II}	-2.826	4.894	0.000	-0.20
1	Ba _{II}	2.826	4.894	0.000	-0.20
1	O	-1.413	2.477	0.000	0.02
1	O	1.413	2.477	0.000	0.02
1	O	-5.651	4.894	0.000	0.02
1	O	5.651	4.894	0.000	0.02
1	O	-1.413	7.341	0.000	0.02
1	O	1.413	7.341	0.000	0.02
2	Ti	-5.651	3.262	1.153	0.04
2	Ti	0.000	3.262	1.153	0.04
2	Ti	5.651	3.262	1.153	0.04
3	Ba	-2.826	1.631	2.307	0.38
3	Ba	2.826	1.631	2.307	0.38
3	Ba	0.000	6.525	2.307	0.38
3	O _I	0.000	1.631	2.307	-0.08
3	O _I	-7.064	4.078	2.307	-0.08
3	O _I	7.060	4.078	2.307	-0.08
3	O _{II}	-4.238	4.078	2.307	-0.20
3	O _{II}	-1.413	4.078	2.307	-0.20
3	O _{II}	1.413	4.078	2.307	-0.20
3	O _{II}	4.238	4.078	2.307	-0.20
3	O _{II}	-2.825	6.525	2.307	-0.20
3	O _{II}	2.825	6.525	2.307	-0.20
4	Ti _I	0.000	0.000	3.460	-0.06
4	Ti _{II}	-2.825	4.894	3.460	0.02
4	Ti _{II}	2.825	4.894	3.460	0.02

Table 6.3 lists the R_P factors for each model considered as shown in Fig. 6.10. For Ti terminated models, all R_P factors are above 0.50, for BaO terminated models, the R_P factors are smaller than for Ti terminated models but the minimum R_P factor is still above 0.40. The best-fit model is the BaO_{6C} model, for which an R -factor of $R_P = 0.40$ is obtained.

The best-fit structure is shown in Fig. 6.12. For this structure, one-third of the oxygen in the topmost BaO terminated surface was removed. This result is reasonable if we consider the charge compensation problem of the polar surface. Details of the best-fit structure are given in table 6.4. It includes the coordinates of atoms in the upper four layers of the reference structure plus the vertical displacement obtained for the best-fit structure. The $I - V$ curves comparison between theory and experiment for the best-fit structure is shown in Fig. 6.11a and Fig. 6.11b for the integral and fractional order beams, respectively. The integral order beams have an averaged R_P factor of 0.37. They fit better than the fractional order beams, which have an averaged R_P factor of 0.52. The higher R_P factor for the fractional order beams is partly due to their weak intensity. This limits the measurable energy range of the fractional order beams and increases their noise level. Even though the fractional beams were visible on the video screen, the software was not always capable to measure the intensity due to problems with subtracting the background intensity.

The best-fit structure shows strong relaxations of the first (-0.24 Å and -0.20 Å) and the third (0.38 Å) Ba layers, which correspond to -19% (averaged two planes in the first layer) and 33% of the bulk layer distance. The relaxations are relatively weak for the second and fourth Ti layers, which are within $\pm 5\%$ of the bulk layer distance. Unfortunately, the scattering strength of Ti and Ba is much larger than that of oxygen. This entails that the $I - V$ curves are dominated by the strong scatterer positions, while the positions of oxygen atoms cause only minor modifications.

The minimum R_P factor of 0.40 is acceptable in view of the complexity of the structure and the atomic approximation used for the scattering potential. Nevertheless, the level of the minimum R factor indicates that the structure found can be refined by additional structural variations, which we could not consider because of limited computer time. For example, the reconstruction may extend also to deeper layers or include the lateral displacement within the $p3m1$ symmetry. The level of the minimum R factor is rather high compared to single component systems. It is well known, however, that in general the agreement becomes worse with increasing complexity of the surface. In the present case the complexity comes from several features, the presence of three different atoms, the existence of six terminations, the large superstructure unit cell (15 atoms for each composite layer), and the appearance of surface rumpling. It is hard to find an equivalent system in the literature for comparison. Perhaps the most similar system in this respect is the relatively simple SrTiO₃(100) surface, for which an R factor of 0.53 was reported [23].

Since all six BaO terminated models have the same level of minimum R_P factor, we

further check the results of all these models. We found for all these models, that the optimized structures shown some common features: The Ba planes in the first layer are expanded by about 0.20 ± 0.10 Å, the Ba planes in the third layer is contracted by about 0.40 ± 0.06 Å. The Ti planes in both second and fourth layers are nearly unchanged, within a range of 0.00 ± 0.10 Å. However, the oxygen planes among the different models show no common features, some are expanded, others are contracted, the magnitude of the relaxations is also different and depend on the specific model. This confirms again that the investigation with the present $I-V$ curves is not sensitive enough to determinate the positions of the oxygen atoms. However, the relaxation of the Ba atoms in the first and third layers as well as the bulk positions of Ti atoms in the second and fourth layers appear to be reliable.

Chapter 7

Conclusions

In this thesis, two types of transition metal oxide systems were investigated by means of low energy electron diffraction. The aim of these investigations is to obtain more detailed structure information of these systems. One type is CoO films grown on a Ag(100) substrate. They were characterized by both kinematic (SPA-LEED) and dynamic (Tensor LEED) methods. In addition, the SPA-LEED results were complemented by STM results obtained in previous investigation. The other type of system is the $(\sqrt{3} \times \sqrt{3})R30^\circ$ reconstructed BaTiO₃(111) surface. The structure of this surface was studied by tensor LEED.

Regarding the CoO/Ag(100) system, it has been shown that surface defects on the Ag(100) substrate have a strong influence on the growth of CoO films. Therefore, considerable effort was put into the analysis of the defects of clean Ag(100) surfaces. The various surface defects have been characterized using high resolution LEED (SPA-LEED). The splitting of LEED spots reveals the presence of regular step arrays on the surface, whereby the splitting direction indicates the step edges along the $\langle 110 \rangle$ direction. On an annealed Ag(100) surface, surface facets with (111) orientation were identified using an Ewald construction. For an ion sputtered Ag(100) surface, two dimensional LEED spots exhibit an anisotropic square shape at the "out-of-phase" conditions, in compliance with square pit-like structures in the corresponding STM images. The large FWHM of the one dimensional spot profile measured at the "out-of-phase" conditions indicates a high step density on this ion sputtered Ag(100) surface, with a average terrace width of 3 ± 1 atom distances. The anisotropic square shape disappears after annealing.

A tensor LEED analysis has been performed in order to determine the atomic structure and relaxation of the clean Ag(100) surface. By this analysis, a small inward relaxation in the top layer of Ag(100) surface was observed, the relaxation of the second layer is negligible. This result compliance with the general behavior of surface relaxations on low index fcc or bcc metal surfaces as well as theoretical investigations. The progress of this analysis compared to the former one is that the agreement between experiment and theory improved considerably. The R_P factor went down from 0.39 to 0.15 with the same total energy range.

Before growing CoO films on the Ag(100) substrate, pure Co films have been grown

and analyzed by SPA-LEED. The substrate peak intensities were found to decrease with the thickness of the Co film. Moreover, no LEED pattern was observed for high thickness films (5 ML). Due to the large lattice constant mismatch between Co and the Ag(100) substrate, Co films obviously grow in a three dimensional cluster mode on the Ag(100) surface without any long rang order.

CoO films were grown by depositing Co in an O₂ ($p(\text{O}_2) = 1 \times 10^{-6}$ mbar) atmosphere at different substrate temperatures (300-500 K) and annealing temperatures (300-700 K). The SPA-LEED analysis demonstrates that either by subsequent annealing (450-500 K) or by deposition of the films on a hot (450-500 K) substrate, ordered CoO films form on Ag(100). The overall morphology and the structure of the deposited films, however, drastically depend on the deposition and annealing temperature as well as on the film thickness. With room temperature deposition of a low thickness (2 ML) film, a (2×1) superstructure was observed. Middle thickness (5 ML) films give a (1×1) structure. The strain of the film was released at this film thickness as shown by a one dimensional spot profile analysis. At a thickness of 10 ML, a $(111)(\sqrt{3} \times \sqrt{3})R30^\circ$ superstructure together with a $(100) (2 \times 1)$ superstructure has been obtained. An atomic structure model for the $(111)(\sqrt{3} \times \sqrt{3})R30^\circ$ superstructure has been proposed.

When 1.2 ML CoO films were deposited at 390 K, an O/metal precursor state was identified, again in compliance with the STM image. This precursor state is supposed to be due to a moiré pattern of the substrate and precursor lattices. By deposition of the CoO film at 470 K with a 5 ML thickness the film shows a (1×1) structure. Annealing this film up to 660 K further improves the order of the film as deduced from the sharpening of the LEED spots. The substrate temperature between 450-500 K proved to be the optimal temperature for the growth of a smooth and ordered CoO film on Ag(100).

A 4 ML thick CoO film grown by depositing of Co in an O₂ atmosphere (1×10^{-6} mbar) at elevated temperature (470 K) was analyzed by tensor LEED. The result shows that at the CoO/Ag(100) interface, the O atoms are located on top of Ag atoms, while the Co atoms occupy hollow sites. In the lateral direction, this CoO film on Ag(100) is pseudomorphic, which implies an in-plane lattice compression by 4.3% of the bulk value. In the vertical direction, the first and second layers distance are expanded by 5.6 % and 2.4 % of the bulk layer distance, respectively. Different relaxations of the Co cations and the O anions in the top layer cause a surface rumpling by 2.8 % of the bulk layer distance, the surface rumpling in the second layer is negligible.

The BaTiO₃ $(111)(\sqrt{3} \times \sqrt{3})R30^\circ$ surface has been analyzed by the tensor LEED method. Nine different models for both BaO and Ti terminations were considered as initial structures for a structure determination. The result shows that the BaO termination with one-third of the O atoms of the top layer removed was the best-fit structure. For this optimized structure, a strong relaxation was observed in the first

and third BaO layers while the second and fourth Ti layers remain at bulk positions. However, other models could not be excluded, because of comparable Pendry R_P factors. Although it has not been possible to uniquely identify the structure of the $\text{BaTiO}_3(111)(\sqrt{3} \times \sqrt{3})R30^\circ$ surface, this investigation has enabled us to exclude the Ti terminated models. Furthermore, strong relaxations of similar size were found for the Ba atoms in the first and third layers in all models. Therefore, they are regarded as significant contrary to the relaxations of the O atoms.

Bibliography

- [1] V.E. HENRICH AND P.A. COX. “The Surface Science of Metal Oxides”. Cambridge University Press, Cambridge (1994).
- [2] P.A. COX. “Transition Metal Oxides. An Introduction to their Electronic Structure and Properties”. Clarendon Press, Oxford (1995).
- [3] CH. WEIßMANTEL AND C. HAMANN. “Grundlagen der Festkörperphysik”. VEB Deutscher Verlag der Wissenschaften, Berlin (1989).
- [4] H.-J. FREUND, B. DILLMANN, O. SEIFERTH, G. KLIVENYI, M. BENDER, D. EHRLICH, AND D. CAPPUS. *Catalysis Today* **32**, 1–10 (1996).
- [5] H.-J. FREUND, B. DILLMANN, D. EHRLICH, M. HÄBEL, R.M. JAEGER, H. KUHLENBECK, C.A. VENTRICE JR., F. WINKELMANN, S. WOHLRAB, C. XU, T. BERTRAMS, A. BRODDE, AND H. NEDDERMEYER. *J. Mol. Catal.* **82**, 143–169 (1993).
- [6] H. ESAKI. *Integr. Ferroelectr.* **14**, 11–21 (1997).
- [7] M. MATSUOKA AND S. TOHNO. *J. Vac. Sci. Technol. A* **13**, 2427–2434 (1995).
- [8] X.M. LU, J.S. ZHU, W.Y. ZHANG, G.Q. MA, AND Y.N. WANG. *Thin Solid Films* **274**, 165–168 (1996).
- [9] G.M. DAVIES AND M.C. GOWER. *Appl. Phys. Lett.* **55**, 112–114 (1989).
- [10] J. ZHANG, M. SZABADI, AND P. HESS. *J. Vac. Sci. Technol. B* **14**, 1600–1606 (1996).
- [11] K. IJIMA, T. TERASHIMA, K. YAMAMOTO, K. HIRATA, AND Y. BANDO. *Appl. Phys. Lett.* **56**, 527–529 (1990).
- [12] Y. YANO, K. IJIMA, Y. DAITOH, T. TERASHIMA, AND Y. BANDO. *J. Appl. Phys.* **76**, 7833–7837 (1994).
- [13] B.S. KWAK, K. ZHANG, E.P. BOYD, A. ERBIL, AND B.J. WILKENS. *J. Appl. Phys.* **69**, 767–772 (1991).

- [14] L.A. WILLS, B.W. WESSELS, D.S. RICHESON, AND T.J. MARKS. *Appl. Phys. Lett.* **60**, 41–43 (1992).
- [15] “Group III: Crystal and Solid State Physics, Landolt-Börnstein: Numerical Data and Functional Relationships in Science and Technology”. New Series vol. 17h, p. 188. Springer, Berlin (1985).
- [16] W. HEYWANG. *Sol. Stat. Electron.* **3**, 51–58 (1961).
- [17] G.H. JONKER. *Sol. Stat. Electron.* **7**, 895–903 (1964).
- [18] J. NOWOTNY AND M. REKAS. *Ceram. Int.* **17**, 227–241 (1991).
- [19] H. OGAWA, M. DEMURA, T. YAMAMOTO, AND T. SAKUMA. *J. Mater. Sci. Lett.* **15**, 537–538 (1996).
- [20] S.N. ZHU AND W.W. CAO. *Phys. Rev. Lett.* **79**, 2558–2561 (1997).
- [21] M. TAKASHIGE, S. HAMAZAKI, F. SHIMIZU, AND S. KOJIMA. *Ferroelectrics* **196**, 531–534 (1997).
- [22] B.M. PARK AND S.J. CHUNG. *Ferroelectrics* **197**, 717 (1997).
- [23] N. BICKEL, G. SCHMIDT, K. HEINZ, AND K. MÜLLER. *Phys. Rev. Lett.* **62**, 2009–2011 (1989).
- [24] H.-J. FREUND, H. KUHNENBECK, AND V. STAEMMLER. *Rep. Prog. Phys.* **59**, 283–347 (1996).
- [25] D. CAPPUS, C. XU, D. EHRLICH, B. DILLMANN, C.A. VENTRICE, K. AL-SHAMERY, H. KUHNENBECK, AND H.-J. FREUND. *Chem. Phys.* **177**, 533–546 (1993).
- [26] F. ROHR, K. WIRTH, J. LIBUDA, D. CAPPUS, M. BAÜMER, AND H.-J. FREUND. *Surf. Sci.* **315**, L977–L982 (1994).
- [27] R. LACMANN. *Colloq. Int. CNRS.* **152**, 195 (1965).
- [28] D. WOLF. *Phys. Rev. Lett.* **68**, 3315–3318 (1992).
- [29] K. WANDELT. *Surf. Sci. Rep.* **2**, 1–121 (1982).
- [30] M. BAÜMER, D. CAPPUS, H. KUHNENBECK, H.-J. FREUND, G. WILHELMI, A. BRODDE, AND H. NEDDERMEYER. *Surf. Sci.* **253**, 116–128 (1991).
- [31] K. MARRE AND H. NEDDERMEYER. *Surf. Sci.* **287**, 995–999 (1993).

- [32] T. BERTRAMS. “Rastertunnelmikroskopische Untersuchungen katalytischer Modellsysteme”. Dissertation, Ruhr-Universität Bochum (1996).
- [33] R.M. JAEGER, H. KUHLENBECK, H.-J. FREUND, M. WUTTIG, W. HOFFMAN, R. FRANCHY, AND H. IBACH. *Surf. Sci.* **259**, 235–252 (1991).
- [34] A. ROSENHAHN, J. SCHNEIDER, C. BECKER, AND K. WANDEL. *Appl. Surf. Sci.* **142**, 169–173 (1999).
- [35] A. ROSENHAHN, J. SCHNEIDER, J. KANDLER, C. BECKER, AND K. WANDEL. *Surf. Sci.* **433-435**, 705–710 (1999).
- [36] M.R. CASTELL, P.L. WINCOTT, C. MUGGELBERG, G. THORNTON, S.L. DUDAREV, A.P. SUTTON, AND G.A.D. BRIGGS. *Phys. Rev. B* **55**, 7859–7863 (1997).
- [37] T. BERTRAMS, A. BRODDE, H. HANNEMANN, C.A. VENTRICE, G. WILHELM, AND H. NEDDERMEYER. *Appl. Surf. Sci.* **75**, 125–132 (1994).
- [38] M. HEILER. “Elektronische und Geometrische Struktur dünner CoO-Schichten auf Au(111) und Ag(100)”. Dissertation, Martin-Luther-Universität Halle-Wittenberg (1999).
- [39] H. LANDOLT AND R. BÖRNSTEIN (EDS.), editors. “Landolt-Börnstein Zahlenwerte und Funktionen aus Naturwissenschaften und Technik: Neue Serie”. Springer, Berlin (1961).
- [40] C. KITTEL. “Einführung in die Festkörperphysik”. Oldenbourg, München (1993).
- [41] W. KLEBER. “Kristallchemie”. B.G. Teubner, Leipzig (1963).
- [42] G. NATTA AND M. STRADA. *Gazz. Chim. Ital.* **58**, 419–433 (1928).
- [43] P.S. AGGARWAL AND A. GOSWAMI. *J. Phys. Chem.* **65**, 2105–2105 (1961).
- [44] C.R. BRUNDLE, T.J. CHUANG, AND D.W. RICE. *Surf. Sci.* **60**, 286–300 (1976).
- [45] P.W. TASKER. *J. Phys. C: Solid State Phys.* **12**, 4977–4984 (1979).
- [46] R.W. NOSKER, P. MARK, AND J.D. LEVINE. *Surf. Sci.* **19**, 291–317 (1970).
- [47] C. NOGUERA. *J. Phys: Condens. Matter* **12**, R367–R410 (2000).
- [48] C.B. DUKE. *Chem. Rev.* **96**, 1237–1259 (1996).

- [49] M.R. CASTELL, S.L. DUDAREV, G.A.D. BRIGGS, AND A.P. SUTTON. *Phys. Rev. B* **59**, 7342–7345 (1999).
- [50] R.C. FELTON, M. PRUTTON, S.P. TEAR, AND M.R. WELTON-COOK. *Surf. Sci.* **88**, 474–478 (1979).
- [51] G. WITTE, P. SENET, AND J.P. TOENNIES. *Phys. Rev. B* **58**, 13264–13274 (1998).
- [52] M. PRUTTON, J.A. WALKER, M.R. WELTON-COOK, R.C. FELTON, AND J.A. RAMSEY. *Surf. Sci.* **89**, 95–101 (1979).
- [53] J.L. MACKAY AND V.E. HENRICH. *Phys. Rev. B* **39**, 6156–6168 (1989).
- [54] Z.-X. SHEN, D.S. DESSAU B.O. WELLS A. BORG W. ELLIS J.S. KANG S.-J. OH I. LINDAU J.W. ALLEN, P.A.P. LINDBERG, AND W.E. SPICER. *Phys. Rev. B* **42**, 1817–1828 (1990).
- [55] M. HEILER, A. CHASSE, K.M. SCHINDLER, M. HOLLERING, AND H. NEDDERMEYER. *Surf. Sci.* **454**, 36–40 (2000).
- [56] A. BARBIER AND G. RENAUD. *Surf. Sci. Lett.* **392**, L15–L20 (1997).
- [57] A. BARBIER, G. RENAUD, AND A. STIERLE. *Surf. Sci.* **402-404**, 757–760 (1998).
- [58] O.L. WARREN AND P.A. THIEL. *J. Chem. Phys.* **100**, 659–663 (1994).
- [59] H. HANNEMANN, C.A. VENTRICE, T. BERTRAMS, A. BRODDE, AND H. NEDDERMEYER. *Phys. Stat. Sol. A* **146**, 289–297 (1994).
- [60] C.A. VENTRICE JR., T. BERTRAMS, H. HANNEMANN, A. BRODDE, AND H. NEDDERMEYER. *Phys. Rev. B* **49**, 5773–5776 (1994).
- [61] P.M. OLIVER, G.W. WATSON, AND S.C. PARKER. *Phys. Rev. B* **52**, 5323–5329 (1995).
- [62] A. BARBIER, C. MOCUTA, H. KUHLENBECK, K.F. PETERS, B. RICHTER, AND G. RENAUD. *Phys. Rev. Lett.* **84**, 2897–2900 (2000).
- [63] I. IGNATIEV, B.W LEE, AND M.A. VAN HOVE. Proc. 7th IVC & 3rd ICSS, Eds. R. Dobrozemsky, F. Rüdener and F.P. Viehböck, Vienna, 1733-1736, (1977).
- [64] M.E. BRIDGE AND R.M. LAMBERT. *Surf. Sci.* **82**, 413–424 (1979).

- [65] U. BARDI, B.C. BEARD, AND P.N. ROSS. *J. Vac. Sci. Technol. A* **6**, 665–670 (1988).
- [66] M. HASSEL AND H.-J. FREUND. *Surf. Sci.* **325**, 163–168 (1995).
- [67] M. SCHONNENBECK, D. CAPPUS, J. KLINKMANN, H.-J. FREUND, L.G.M. PETTERSON, AND P.S. BAGUS. *Surf. Sci.* **347**, 337–345 (1996).
- [68] I. SEBASTIAN, K. MEINEL M. HEILER, AND H. NEDDERMEYER. *Appl. Phys. A* **66**, 525–528 (1998).
- [69] I. SEBASTIAN, M. HEILER, K. MEINEL, AND H. NEDDERMEYER. *J. Appl. Phys. A* **66**, 525–528 (1998).
- [70] C. MOCUTA, A. BARBIER, AND G. RENAUD. *Appl. Surf. Sci.* **162**, 56–61 (2000).
- [71] M.A. LANGELL, M.D. ANDERSON, G.A. CARSON, L. PENG, AND S. SMITH. *Phys. Rev. B* **59**, 4791–4798 (1999).
- [72] J. GONIAKOWSKI AND C. NOGUERA. *Surf. Sci.* **365**, L657–L662 (1996).
- [73] R. COURTHS. *Phys. Stat. Sol. B* **100**, 135 (1980).
- [74] H. BANDO, T. SHIMIZU, Y. AIURA, Y. HARUYAMA, K. OKA, AND Y. NISHIHARA. *J. Vac. Sci. Technol. B* **14**, 1060–1063 (1995).
- [75] T. SHIMIZU, H. BANDO, Y. AIURA, Y. HARUYAMA, K. OKA, AND Y. NISHIHARA. *Jpn. J. Appl. Phys.* **34**, L1305–L1308 (1995).
- [76] D. ABERDAM, G. BOUCHET, AND P. DUCROS. *Surf. Sci.* **27**, 559–570 (1971).
- [77] B. CORD AND R. COURTHS. *Surf. Sci.* **152**, 1141–1146 (1985).
- [78] T. MATSUMOTO AND T. KAWAI S. KAWAI H. TANAKA, K. KOUGUCHI. *Surf. Sci.* **312**, 21–30 (1994).
- [79] E. HEIFETS, S. DORFMAN, D. FUKS, AND E. KOTOMIN. *Thin Solid Films* **296**, 76–78 (1997).
- [80] J. PADILLA AND D. VANDERBILT. *Phys. Rev. B* **56**, 1625–1631 (1997).
- [81] X.Y. XUE, C.L. WANG, AND W.L. ZHONG. *Surf. Sci.* **550**, 73–80 (2004).
- [82] A. POJANI, F. FINOCCHI, AND C. NOGUERA. *Appl. Surf. Sci.* **142**, 177–181 (1999).
- [83] H. TANAKA AND T. KAWAI. *Surf. Sci.* **365**, 437–442 (1996).

- [84] W.J. LO AND G.A. SOMORJAI. *Phys. Rev. B* **17**, 4942–4950 (1978).
- [85] S. SEKIGUCHI, M. FUJIMOTO, M.G. KANG, S. KOIZUMI, S.B. CHO, AND J. TANAKA. *Jpn. J. Appl. Phys.* **37**, 4140–4143 (1998).
- [86] A. POJANI, F. FINOCCHI, AND C. NOGUERA. *Surf. Sci.* **442**, 179–198 (1999).
- [87] C. HAGENDORF, K.M. SCHINDLER, T. DOEGE, AND H. NEDDERMEYER. *Surf. Sci.* **404**, 581–585 (1998).
- [88] M.A. VAN HOVE, W.H. WEINBERG, AND C.-M. CHAN. “Low-Energy Electron Diffraction”. Springer Verlag, Berlin (1986).
- [89] M.A. VAN HOVE, W. MORITZ, H. OVER, P.J. ROUS, A. WANDER, A. BARBIERI, N. MATERER, U. STARKE, AND G.A. SOMORJAI. *Surf. Sci. Rep.* **19**, 191–229 (1993).
- [90] M. HORN-VON HOEGEN. *Z. Kristallogr.* **214**, 684–721 (1999).
- [91] P.J. ROUS AND J.B. PENDRY. *Surf. Sci.* **173**, 1–19 (1986).
- [92] R.L. PARK AND J.E. HOUSTON. *Surf. Sci.* **18**, 213–227 (1969).
- [93] J.E. HOUSTON AND R.L. PARK. *Surf. Sci.* **21**, 209–223 (1970).
- [94] M. HENZLER. *Appl. Phys.* **9**, 11–17 (1976).
- [95] K. HEINZ. *Rep. Prog. Phys.* **58**, 637–704 (1995).
- [96] J.B. PENDRY. “Low Energy Electron Diffraction”. Academic, London (1974).
- [97] M.A. VAN HOVE AND S.Y. TONG. “Surface Crystallography by LEED”. Springer Verlag, Berlin (1979).
- [98] J.B. PENDRY. *J. Phys. C: Solid State Phys.* **13**, 937–944 (1980).
- [99] W. MORITZ AND D. WOLF. *Surf. Sci.* **163**, L655–L665 (1985).
- [100] S.Y. TONG, H. HUANG, C.M. WEI, W.E. PACKARD, F.K. MEN, G. GLANDER, AND M.B. WEBB. *J. Vac. Sci. Technol. A* **6**, 615–624 (1988).
- [101] J.B. PENDRY AND K. HEINZ. *Surf. Sci.* **230**, 137–149 (1990).
- [102] P.J. ROUS. *Prog. Surf. Sci.* **39**, 3–63 (1992).
- [103] P.J. ROUS AND J.B. PENDRY. *Surf. Sci.* **219**, 373–394 (1989).
- [104] P.J. ROUS, M.A. VAN HOVE, AND G.A. SOMORJAI. *Surf. Sci.* **226**, 15–25 (1990).

- [105] P.G. COWELL AND V.E. DECARVALHO. *Surf. Sci.* **187**, 175–193 (1987).
- [106] G. KLEINLE, W. MORITZ, D.L. ADAMS, AND G. ERTL. *Surf. Sci.* **219**, L637–L645 (1989).
- [107] D.W. MARQUARDT. *J. Soc. Ind. Appl. Math.* **11**, 431–441 (1963).
- [108] W.H. PRESS, B.P. FLAY, S.A. TEUKOLSKY, AND W.T. VETTERLING. “Numerical Recipes”. Cambridge University Press, Cambridge (1986).
- [109] J.F. BINDER. “Wachstum und Elektronische Struktur dünner Cu/Co-Schichten auf Cu(100) und Cu(111)”. Dissertation, Ruhr-Universität Bochum (1998).
- [110] U. SCHEITHAUER, G. MEYER, AND M. HENZLER. *Surf. Sci.* **178**, 441–451 (1986).
- [111] C. TEICHERT. “Atomare Prozesse auf der Silber(100)-Oberfläche beim Abtrag durch Ionenbeschuß und während des homoepitaktischen Wachstums”. Dissertation, Martin-Luther-Universität Halle-Wittenberg (1992).
- [112] C. TEICHERT, C. AMMER, AND M. KLAUA. *Phys. Stat. Sol. A* **146**, 223–242 (1994).
- [113] M. HENZLER AND W. GÖPEL. “Oberflächenphysik des Festkörpers”. Teubner, Stuttgart (1991).
- [114] G. COSTANTINI, S. RUSPONI, R. GIANOTTI, C. BORAGNO, AND U. VALBUSA. *Surf. Sci.* **416**, 245–254 (1998).
- [115] P. BEDROSSIAN, B. POELSEMA, G. ROSENFELD, L.C. JORRITSMAN, N.N. LIPKIN, AND G. COMSA. *Surf. Sci.* **334**, 1–9 (1995).
- [116] S. HILDEBRANDT, A. KRAUS, R. KULLA, AND H. NEDDERMEYER. *Appl. Surf. Sci.* **141**, 294–304 (1999).
- [117] CH. AMMER, K. MEINEL, H. WOLTER, A. BECKMANN, AND H. NEDDERMEYER. *Surf. Sci.* **375**, 302–314 (1997).
- [118] Y. LIANG AND D.A. BONNELL. *Surf. Sci.* **310**, 128–134 (1994).
- [119] H. TANAKA, T. MATSUMOTO, T. KAWAI, AND S. KAWAI. *Surf. Sci.* **318**, 29–38 (1994).
- [120] L.T. HUDSON, R.L. KURTZ, S.W. ROBEY, D. TEMPLE, AND R.L. STOCKBAÜER. *Phys. Rev. B* **47**, 1174–1180 (1993).

- [121] L.T. HUDSON, R.L. KURTZ, AND S.W. ROBEY. *Phys. Rev. B* **47**, 10832–10838 (1993).
- [122] R.L. PARK AND H.E. FARNSWORTH. *Surf. Sci.* **2**, 527–533 (1964).
- [123] W.P. ELLIS AND R.L. SCHWOEBE. *Surf. Sci.* **11**, 82–98 (1968).
- [124] I. SEBASTIAN. “Rastertunnelmikroskopie zur Keimbildung und zum Wachstum dünner CoO-Schichten auf Ag(100) und Au(111)”. Dissertation, Martin-Luther-Universität Halle-Wittenberg (2000).
- [125] G.A. CARSON, M.H. NASSIR, AND M.A. LANGELL. *J. Vac. Sci. Technol. A* **14**, 1637–1642 (1996).
- [126] W.-D. WANG, N.J. WU, AND P.A. THIEL. *J. Chem. Phys.* **92**, 2025–2035 (1990).
- [127] H. NIEHUS, R.P. BLUM, AND D. AHLBEHRENDT. *Phys. Stat. Sol. A* **187**, 151–159 (2001).
- [128] J.J. BURTON AND G. JURA. *J. Phys. Chem.* **71**, 1937–1940 (1967).
- [129] P.J. FEIBELMAN. *Surf. Sci.* **300**, 426–432 (1994).
- [130] H. LI, J. QUINN, Y.S. LI, D. TIAN, F. JONA, AND P.M. MARCUS. *Phys. Rev. B* **43**, 7305–7307 (1991).
- [131] E.A. SOARES, V.B. NASCIMENTO, V.E. DE CARVALHO, A.V. DE CARVALHO, R. TOOMES, AND D.P. WOODRUFF. *Surf. Sci.* **419**, 89–96 (1999).
- [132] A. BARBIERI AND M.A. VAN HOVE. Symmetrized Automated Tensor LEED Package, from M.A. Van Hove, Lawrence Berkeley Laboratory, 94720 Berkeley, CA, USA, Available from <http://www.lbl.gov/software>.
- [133] P.M. BOHNEN, TH. RODACH, AND K.M. HO. “The Structure of Surfaces III”. edited by S.Y. Tong and M.A. Van Hove, Springer Verlag, New York. (1991).
- [134] T. NING, Q.L. YU, AND Y.Y. YE. *Surf. Sci.* **206**, L857–L863 (1988).
- [135] S.M. FOILES, M.I. BASKES, AND M.S. DAW. *Phys. Rev. B* **33**, 7983–7991 (1986).
- [136] H.L. DAVIS AND J.R. NOONAN. *Surf. Sci.* **126**, 245–252 (1983).
- [137] W. OED, H. LINDNER, U. STARKE, K. HEINZ, K. MÜLLER, AND J.B. PENDRY. *Surf. Sci.* **224**, 179–194 (1989).

- [138] P. JIANG, P.M. MARCUS, AND F. JONA. *Sol. Stat. Commun.* **59**, 275–280 (1986).
- [139] F. JONA AND P.M. MARCUS. “The Structure of Surface II”. edited by J.F. van der Veen and M.A. Van Hove, Springer Verlag, New York. (1987), p90.
- [140] J.G. ROBERTS, S. HOFFER, M.A. VAN HOVE, AND G.A. SOMORJAI. *Surf. Sci.* **437**, 75–85 (1999).
- [141] A. BARBIERI, W. WEISS, M.A. VAN HOVE, AND G.A. SOMORJAI. *Surf. Sci.* **302**, 259–279 (1994).
- [142] C. GIOVANARDI, A. DI BONA, S. ALTIERI, P. LUCHES, M. LIBERATI, F. ROSSI, AND S. VALERI. *Thin Solid Films* **428**, 195–200 (2003).
- [143] S. VALERI AND A. DI BONA. *Surf. Rev. Lett.* **4**, 141–160 (1997).
- [144] C. GIOVANARDI, A. DI BONA, T.S. MOIA, S. VALERI, C. PISANI, M. SGROI, AND M. BUSSO. *Surf. Sci.* **505**, L209–L214 (2002).
- [145] M. CAFFIO, B. CORTIGIANI, G. ROVIDA, A. ATREI, C. GIOVANARDI, A. DI BONA, AND S. VALERI. *Surf. Sci.* **531**, 368–374 (2003).
- [146] F. ROHR, M. BAÜMER, H.-J. FREUND, J.A. MEJIAS, V. STAEMMLER, S. MÜLLER, L. HAMMER, AND K. HEINZ. *Surf. Sci.* **372**, L291–L297 (1997).
- [147] I. MANASSIDIS, A. DEVITA, AND M.J. GILLAN. *Surf. Sci.* **285**, L517–L521 (1993).
- [148] J. AHN AND J.W. RABALAIS. *Surf. Sci.* **388**, 121–131 (1997).
- [149] X.G. WANG, W. WEISS, S.K. SHAIKHUTDINOV, M. RITTER, M. PETERSEN, F. WAGNER, R. SCHLOGL, AND M. SCHEFFLER. *Phys. Rev. Lett.* **81**, 1038–1041 (1998).
- [150] N.G. CONDON, F.M. LEIBSLE, A.R. LENNIE, P.W. MURRAY, D.J. VAUGHAN, AND G. THORNTON. *Phys. Rev. Lett.* **75**, 1961–1964 (1995).
- [151] J. TOOFAN AND P. R. WATSON. *Surf. Sci.* **401**, 162–172 (1998).
- [152] C. HAGENDORF, K.M. SCHINDLER, T. DOEGE, AND H. NEDDERMEYER. *Surf. Sci.* **436**, 121–130 (1999).
- [153] V. BLUM AND K. HEINZ. *Compt. Phys. Commun.* **134**, 392–425 (2001).
- [154] M. KOTTCKE, B. DOTSCH, L. HAMMER, K. HEINZ, K. MÜLLER, AND D.M. ZEHNER. *Surf. Sci.* **376**, 319–329 (1997).

Abbreviations

AED	Auger Electron Diffraction
AES	Auger Electron Spectroscopy
AFM	Atomic Force Microscopy
ARUPS	Angle-Resolved UPS
FWHM	Full Width at Half Maximum
GIXD	Grazing Incidence X-ray Diffraction
HAS	Helium Atom Scattering
HREELS	High-Resolution Electron Energy Loss Spectroscopy
LEED	Low-Energy Electron Diffraction
NEXAFS	Near-Edge X-Ray Absorption Fine Structure
PDMEEM	Primary-beam Diffraction Modulated Electron Emission
RFS	Renormalized Forward Scattering
RHEED	Reflection High-Energy Electron Diffraction
SPA-LEED	Spot Profile Analysis LEED
SATLEED	Symmetrized Automated Tensor LEED
SEM	Scanning Electron Microscopy
SAM	Scanning Auger Microscopy
STM	Scanning Tunneling Microscopy
STS	Scanning Tunneling Spectroscopy
TEM	Transmission Electron Microscopy
UHV	Ultra-High Vacuum
UPS	Ultraviolet Photoelectron/Photoemission Spectroscopy
XPS	X-ray Photoelectron Spectroscopy
ML	Monolayer
XPD	X-ray Photoelectron Diffraction
K	Kelvin
a.u.	arbitrary unit
Bz	Brillouin zone

Erklärung

Ich erkläre hiermit, dass ich keine anderen als die von mir angegebenen Quellen und Hilfsmittel zur Erstellung meiner Dissertation verwendet habe. Den benutzten Werken wörtlich oder inhaltlich entnommene Stellen sind als solche gekennzeichnet.

Jian Wang

Halle (Saale), im Oktober 2004

Acknowledgements

First of all, I would like to thank my supervisor, Priv.-Doz. Dr. Karl-Michael Schindler for providing me with the opportunity to do this doctoral work in the surface and interface physics group, physics department at the Martin-Luther-University Halle-Wittenberg. His knowledge, ideas and suggestions were very helpful for me. I benefited a lot from them. I wish to thank for his trust, patience, support, guidance and encouragement.

My special thanks to thank Prof. Dr. H. Neddermeyer, the former group head of the group. He provided me the opportunity to work here.

I am very grateful to Prof. Dr. Wolf Widdra, our present group head. He provided me the opportunity to finish my PhD work.

I am also indebted to Dr. Christian Ammer. He taught me the experimental technique of LEED measurement. I thank him for his assistance performing the LEED calculations at the initial stage of my study.

I am grateful to Christel Jeckstiess for technical support.

I would like to express my gratitude to the other colleagues in the group, Dr. Christian Hagendorf, Dr. Klaus Meinel, Dr. Ina Sebastian, Dr. Roman Shantyr, Annette Kindlein, Torsten Doege, Klaus Duncker and all other members of the group for a very pleasant atmosphere, especially.

Special thanks I would like to express to my parents for their encouragement and their support.

Curriculum Vitae

First Name	Jian
Family Name	Wang
Date of Birth	May 09, 1973
Place of Birth	Lanxi, Zhejiang province, P. R. China
Nationality	Chinese
E-mail	<i>jian.wang@physik.uni-halle.de</i>

EDUCATION

<i>Jun. 2000 - present</i>	Martin-Luther-University Halle-Wittenberg (Halle, Germany) Ph.D. candidate (Supervisors: PD. Dr. Karl-Michael Schindler and Prof. Henning Neddermeyer)
<i>Sep. 1997 - Jun. 2000</i>	Zhejiang University (Hangzhou, P. R. China) Master's Degree in Physics
<i>Sep. 1991 - Jun. 1995</i>	Zhejiang University (Hangzhou, P. R. China) Bachelor's Degree in Physics
<i>Sep. 1985 - Jun. 1991</i>	First High School of Lanxi (Lanxi, P. R. China)

PROFESSIONAL EXPERIENCE

<i>Jun. 1995 - Sep. 1997</i>	Sir Run Run Shaw Hospital (Hangzhou, P. R. China) Physical Engineer in Radiotherapy Department
------------------------------	---
